UiO : University of Oslo

Raphael Schuler

Oxide thermoelectrics - materials, junctions and modules

Thermoelectric properties and direct junctions of p- and n-type iron tungstates

Dissertation submitted for the degree of Philosophiae Doctor

Department of Chemistry
Faculty of Natural Sciences and Mathematics

November, 2020

© Raphael Schuler, 2021

Series of dissertations submitted to the
Faculty of Natural Sciences and Mathematics, University of Oslo
No. 2364

ISSN 1501-7710

All rights reserved. No part of this publication may be
reproduced or transmitted, in any form or by any means, without permission.

Cover: Hanne Baadsgaard Utigard.
Print production: Reprosentralen, University of Oslo.

Abstract

Thermoelectric materials are able to directly convert heat into electricity, making them predestined candidates for the recuperation of waste heat and contributing to a more efficient energy economy. Since conventional thermoelectric materials are often toxic, scarce, expensive, and show limited stability at the relevant high temperatures, oxide thermoelectrics have been increasingly investigated in recent years. These represent cheaper, environmental-friendly and temperature-stable alternatives. Traditionally, thermoelectric materials have been discovered and investigated individually, and only later combined as p-n pairs in thermoelectric modules. This often leads to unforeseen complications such as thermal expansion mismatch, interdiffusion, and reactions, especially in the recently emerging direct junction thermoelectric modules. In the present thesis, the approach was pursued to select and investigate a p-n pair that has as many compatible physical properties as possible in order to exclude complications in advance. The approach presented here makes use of ternary semiconducting transition metal oxides, which can form both p and n-type charge carriers through multivalency. Such a model system is found in the materials pair of p-type $FeWO_4$ and n-type Fe_2WO_6. Their structural similarity provides the basis for compatible thermal expansion, whereas different charges in fully charge ordered crystal structures ensures low miscibility.

Since the high temperature properties of the materials are largely unexplored, **Publication I** investigates the conductivity mechanism and thermoelectric properties of Fe_2WO_6 in depth. We identify Fe_2WO_6 to conduct via a small polaron hopping mechanism with oxygen vacancies as the source for n-type charge carriers. We establish a defect chemical model for the formation of oxygen vacancies and report standard enthalpy and entropy of this reaction. By further decoupling carrier concentration from conductivity, we could parameterize the polaron mobility. We report the thermal conductivity of Fe_2WO_6, and calculate a thermoelectric figure of merit of $zT = 0.027$ at 900 °C. Properties of the p-n junction between $FeWO_4$ and Fe_2WO_6 are the subject of **Publication II**. We construct a band alignment diagram from a combination of XPS and UV-VIS spectroscopy. Experimentally acquired I-V characteristics and the constructed band alignment diagram indicate the formation of a near-broken gap junction. This alignment forms a charge accumulation layer in contrast to a charge depletion layer in common p-n junctions and thus exhibits fully ohmic behavior. Complementary DFT calculations show, that both corresponding band edges are of Fe-3d character, which could prove important for their energetic proximity and overlap. In **Publication III** we present a setup for characterizing thermoelectric modules, which was designed and manufactured in cooperation with NORECS AS as part of the THERMiO innovation initiative. The aim of the setup is to test pilot TEGs at high temperatures, under

high temperature gradients, in different atmospheres, and in combination with different contacts. The setup can host four 5 x 5 mm^2 TE-legs with no height restriction, tolerates up to 1000 °C, and generates temperature gradients up to 600 °C.

The setup is demonstrated by characterizing a 4-leg thermoelectric oxide module of p-type NiO and n-type ZnO. We find a large discrepancy between estimated properties from the individual materials and experimentally determined performance of the module. This underlines the importance of evaluating TE-materials in conjunction with their contacts and interconnects under realistic operational conditions.

Preface

This thesis is submitted in partial fulfillment of the requirements for the degree of *Philosophiae Doctor* at the Department of Chemistry, Faculty of Mathematics and Natural Sciences, University of Oslo. The position was financed by the University of Oslo as part of the Thermoelectrics for Industrial Applications (THERMiO) innovation and education cluster. The cluster is headed by Professor Truls Norby and hosted by the Centre for Materials Science and Nanotechnology (SMN). The cluster hosts one position from four different groups under the SMN umbrella organization. My position was with the group for Nanostructures and Functional materials (NAFUMA) under the supervision of Helmer Fjellvåg. Besides the scientific work on thermoelectric properties and interfaces, 25% of the position was dedicated to innovation-related activities relevant to thermoelectrics. The innovation-related work was carried out in cooperation with NORECS AS and involved the design manufacturing and testing of a ceramic setup for the characterization of thermoelectric pilot modules.

Acknowledgements

First of all, I would like to thank my supervisors Helmer Fjellvåg and Truls Norby for your valuable advice, great discussions, your patience, and the opportunity to work independently. Thank you for the great trust you showed during the course of my doctorate and your support in all of my decisions. I would also like to thank Matthias Schrade, whose advice and discussions helped me ”learn to walk” in the field of thermoelectrics and defects in my first months in Oslo and from whom I learned a lot. Moreover, I thank the two research groups, which I was part of during the last years, NAFUMA and the Electrochemistry group. In particular Erik Glesne, Kristin Nygård, Ingrid Marie Bakke Fjellvåg, Julia Wind, Bruno Gino, Henrik Riis, Christian Fleischer, and Monika Amundsen for the many laughs and discussions during coffee breaks, lunches, conferences, and Friday beers that we enjoyed together. In addition, my gratitude goes to my family and parents. I am deeply grateful for your unconditional love and your encouragement all these years.

Contents

1 Introduction

1.1 Heat and Energy

Our modern world as we know it relies on electricity as the universal and flexible energy carrier, and access to electric power has become a matter of course. Since the 18th century, electricity has mainly been generated through the burning of fossil fuels. The resulting heat is used to generate steam and to drive a turbine generator. The availability of fossil fuels is limited, however, as they are the billion year old product of the decomposition of organic matter and do not regenerate within human time scale. In addition, the burning of these fossil fuels releases vast amounts of the greenhouse gas CO_2 into the atmosphere, which has maneuvered the world into a climate crisis. The CO_2 release has lead to global warming, the consequences of which are already noticeable in the form of melting polar caps, increasing extreme weather conditions, and wildfires. A decrease in CO_2 emissions is not to be expected without drastic measures, since the world's population is steadily increasing and will reach almost 10 billion people in 2050.[1] The associated global energy consumption will thus have roughly doubled by then.[2] It is therefore urgent to make use of renewable energy sources and advance their technology, as currently only approximately 17% of the electricity is obtained from renewable energies such as wind power, photovoltaics, and hydropower.[3] However, since many renewable energy sources are subject to strong fluctuations, they are not suitable to cover the grid's base load and their energy densities are often too low to be used effectively for means of transport. It is therefore just as important to improve existing heat driven technologies and to make use of the planet's resources as efficiently as possible. Energy conversion via heat, however, is notoriously inefficient. Conventional internal combustion engines, for example, can convert about 30% of the fuel energy into electricity, a coal-fired power plant about 40%, and even the most modern gas turbine plants only achieve efficiency levels of about 60%.[4–6] The remaining energy is lost to the environment in form of waste heat, following the second

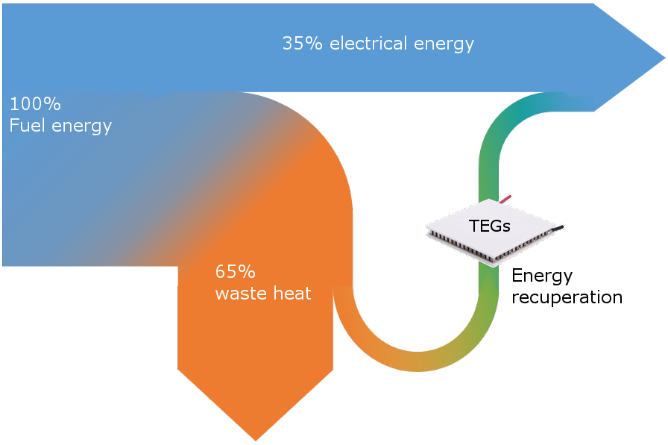

Figure 1.1: Energy efficiency Sankey diagram illustrating the thermal losses occurring in heat driven processes e.g. electricity generation in a coal power plant. Through the use of thermoelectric waste heat harvesting parts of the lost energy could be recovered.

law of thermodynamics and cannot be completely avoided. Such waste heat also occurs in large quantities in other industrial processes such as steel, glass or aluminum plants, and waste incinerators. This "secondary heat" can be seen as a renewable and sustainable energy source if it can be harvested. Conventional systems for heat conversion like Rankine engines are unsuitable for small heat loads below ca. 200 °C and rely on moving parts and liquid coolants, which often makes them too bulky for retrofitting and unsuitable for difficult-to-access, or remote locations, as they require maintenance. Small solid state thermal to electrical converters have no moving parts and are potential alternatives for the direct conversion of waste heat into electricity. Their strength lies in the fact that they do not require any maintenance and therefore produce electricity reliably for years. Among the most promising are thermoelectric generators (TEGs), which provide a direct current supply proportional to the temperature difference in a spatial temperature gradient. However, the currently available TEGs efficiencies are still quite low ($\sim 5\%$) and their technology is not yet mature. The costly manufacturing through piece-by-piece assembly, expensive materials, and low efficiency lead to long investment amortization times, which currently renders their use uneconomic. The use of cheaper materials and a simplified production could, however, qualify them as efficient waste heat harvesters. Attractive are the TEGs already for off-grid applications, such as on ships, aerospace or in remote locations where they do not have to compete with commercial electricity prices.[7–10] The potential of TEGs is enormous, as they can be used in complementary to existing heat engine technologies, retro-fitted, and easily up-scaled, as they are built up modular. Since the majority of the EU's energy consumption occurs in thermal processes such as transport and industry ($\approx 60\%$),[3] the implementation of waste heat recovery in these sectors could significantly increase their energy efficiency. With the emergence of stricter environmental regulations or the introduction of a CO_2 tax, the price of electricity generated from fossil fuels can be expected to rise in the near future, which will make thermoelectricity economical for on-grid applications. Advancing the field of thermoelectric energy generation could unfold its enormous potential and enable it to contribute to a cleaner and more efficient global energy balance.

1.2 Thermoelectric effects

The term "thermoelectric" is a generic term for three related effects that were discovered independently of one another. When in 1822 Thomas Johann Seebeck discovered a current flow in a pair of dissimilar metals when exposed to a temperature gradient, he laid the cornerstone for the field of thermoelectricity.[11] Named after his discovery, the Seebeck effect is the basis for thermoelectric power generation, describing the voltage built-up (V) in a given material upon exposure to a temperature gradient (ΔT).[12]

$$V = -\alpha \Delta T \tag{1.1}$$

The related but reverse effect is called the Peltier effect, discovered by Jean Charles Athanase Peltier in 1834, describing the heat absorption or release rate ($\dot{Q}$), dependent on the sign of the current, at a material junction upon applying a current (I).[13]

$$\dot{Q} = (\Pi_A - \Pi_B)I \tag{1.2}$$

The third and last of the three thermoelectric effects is the Thomson effect. Predicted and observed by Lord Kelvin, it describes the change in heat flux density ($\dot{q}$) of a material in a temperature gradient (ΔT) through which a current density (j) flows.[14]

$$\dot{q} = -\mu_T j \Delta T \tag{1.3}$$

The Seebeck coefficient (α), Peltier coefficient (Π), and Thomson coefficient (μ_T) are related to each other via the Kelvin relations.[15]

$$\mu_T = T\frac{d\alpha}{dT} \quad \text{and} \quad \Pi = T\alpha \tag{1.4}$$

The thermoelectric effects represent bulk material properties and can be used in compact full solid state devices without moving parts, which operate maintenance-free. Based on the Peltier-effect, thermoelectric coolers have found their way into numerous applications, especially in electronics, where small, fast-responding cooling is crucial. CPU-cooling, high precision LASER temperature controllers, and CCD-camera cooling, just to name some examples. One of the most simple devices, based on the Seebeck effect, is a thermocouple. Resembling Seebeck's original setup, a junction of two dissimilar metals allows for inexpensive, self-powered temperature sensing. Thermoelectric power generators have been successfully implemented in e.g. exhaust heat recovery from automobiles, power supply in remote places and so-called wearables as body-heat powered gadgets in every-day life.[16, 17] The by far most celebrated application of thermoelectric power generators are the radio isotope generators used by NASA to power planetary exploration rovers or deep-space probes far from the sun. Utilizing the radioactive isotope Pu-238, with a half-life of 87.7 years, as a heat source and the cold environment of space, they can supply the vehicle for decades with electricity, without the need for sunlight or maintenance.[18] The Kelvin effect is even difficult to prove experimentally and has no practical applications. Since this work focuses on the generation of electricity from heat (thermoelectricity), the term thermoelectrics in the following refers to the context based on the Seebeck effect.

1.3 Thermoelectric materials

The prerequisites of a good thermoelectric material for power generation are easy to state, and summarized in zT, a dimensionless figure of merit. A large Seebeck coefficient α and high electrical conductivity σ, paired with a low thermal conductivity κ maximize the thermoelectric performance.

$$zT = \frac{\alpha^2 \sigma}{\kappa_e + \kappa_{lat}} T \tag{1.5}$$

The thermal conductivity consists of two contributions, the thermal energy transfered by the lattice vibrations κ_{lat} and the thermal energy carried by electrons κ_e. The electronic contribution κ_e is directly related

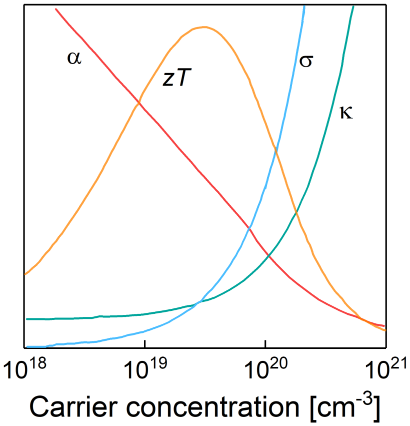

Figure 1.2: Illustration on the charge carrier dependence of conductivity, Seebeck-coefficient, and thermal conductivity. zT peaks at a compromise between all three contributions.

to conductivity (σ), via the Wiedemann-Franz relation.[19]

$$\kappa_e = L\sigma T \tag{1.6}$$

With L being a constant of $2.4\,^{\times}10^{-8}$ WΩK^{-2} called the Lorenz-number. While electronic thermal conductivity cannot be avoided, the minimization of lattice thermal conductivity through various methods such as nanostructuring or the introduction of rattling centers is subject of active research. All of the physical quantities stated above are functions of the charge carrier concentration in a material. While thermal and electrical conductivity increase with increasing carrier concentration, the Seebeck coefficient decreases. This results in a compromise between the individual contributions in order to maximize zT. It has been found that the optimal carrier concentration for any material lies between 10^{18} to

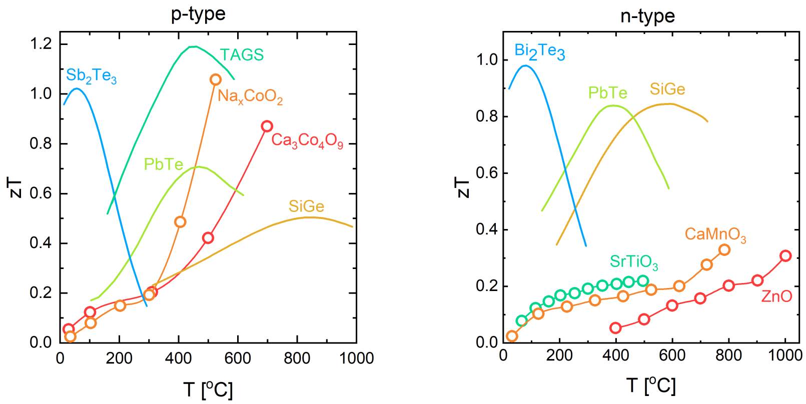

Figure 1.3: Overview of selected p- and n-type thermoelectric materials figures of merit zT as a function of temperature.[23, 25–30]

10^{21} cm^{-3}.

Materials that meet the stated prerequisites best were found to be heavily doped semiconductors. Since the properties of conductivity, Seebeck coefficient and thermal conductivity are all temperature dependent, different materials typically peak in their performance in their respective optimal temperature window. By far the most successful material in heat conversion is Bi_2Te_3. Within a window from room temperature to ca. 200 °C it reaches a zT of 0.8-1.1.[20] For mid-temperature ranges from 200-600 °C the different Te alloys (Pb/Ge/Sn)Te are the materials of choice, with $(GeTe)_{0.85}(AgSbTe_2)_{0.15}$ (”TAGS”) reaching a zT of 1.2.[21] High temperature (>600 °C) thermoelectrics are realized with SiGe-alloys in vacuum, reaching zT values of 0.5-0.9.[22–24] It becomes evident that the current state-of the-art materials are dominantly composed of p-block elements. With the exception of Si, all of these elements are scarce and/or toxic, raising questions about scalability, price, hazard, and life cycle impact of thermoelectric generators.

It was only rather recently, when Terasaki *et al.* discovered a large Seebeck coefficient and high conductivity in the oxide $Na_{0.5}CoO_2$, that a new material class became a considerable alternative to the main-group element alloys.[31] Composed of cheap, abundant, and non-toxic elements, thermoelectric oxides offer new possibilities due to their high temperature stability and increased resistance to harsh environments. In contrast to traditional semiconductors which can be tuned to exhibit both n-type or p-type conductivity, oxides tend to be dominated by intrinsic defects, which usually leaves them uni-polar. Although the possibility to obtain bi-polar oxides has been shown, this usually requires extensive synthetic effort and is rarely maintained over larger windows of temperature or oxygen partial pressures.[32] Thus the oxide thermoelectrics are split in the subgroups of n-type and p-type materials. The layered cobaltites $Ca_3Co_4O_9$ ($zT_{max} = 0.87$ @ 700 °C) together with the afore mentioned $Na_{0.5}CoO_2$ ($zT_{max} = 1.2$ @ ~ 530 °C) present the leading p-type materials.[26, 33] Although the Na-cobaltite shows better performance, the Ca-cobaltite variant is the preferred choice due to higher stability. Among the n-type thermoelectric oxides $SrTiO_3$ ($zT_{max} = 0.37$ @ 700 °C), ZnO ($zT_{max} \approx 0.3$ @ 1000 °C), and $CaMnO_3$ ($zT_{max} \approx 0.3$ @ 700 °C) are the most promising candidates.[34–36] It becomes clear that the n-types lag behind in terms of performance, compared to their p-type counterparts and the search for new promising n-type thermoelectric oxides is an ongoing field of active research.

In summary, the most successful thermoelectric materials are low bandgap p-block semiconductors, which however show limited stability towards high temperatures and tend to oxidize or deteriorate over time. Large band-gap oxides on the other hand exhibit high stability and reliability at the cost of performance.

1.4 Thermoelectric modules

A thermoelectric module can be considered an assembly of two or more individual thermoelectric legs forming a device capable of transforming thermal energy into electricity. As the Seebeck effect is usually in the order of several hundred micro-volts, multiple TE-legs are connected in series in a module. The classic thermoelectric module design consists of alternating n-and p-type TE-legs, connected electrically in series and thermally in parallel. In this way the Seebeck-voltages of the legs add up and a current can be driven through an external load resistance (R_L). The individual TE-legs are connected by flat metal interconnects soldered to the TE-materials. The power output a module with N number

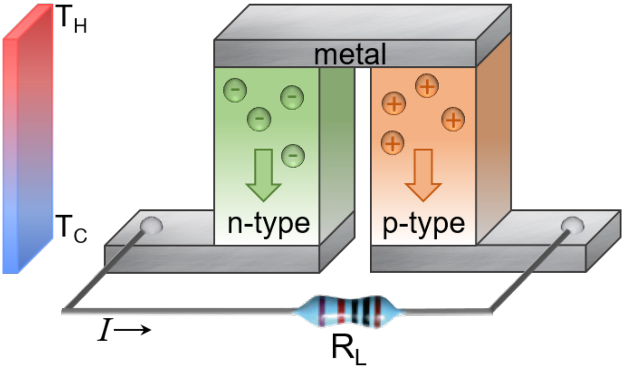

Figure 1.4: Illustration of a 2-leg thermoelectric generator composed of one n-type and one p-type leg connected electrically in series and thermally in parallel.

of p-n pairs produces can be deducted from Ohm's law.

$$P = I^2 R_L = \frac{N(\alpha_p - \alpha_n)^2 \Delta T^2 R_L}{(R_{TEG} + R_L)^2} \tag{1.7}$$

The resistance of the module (R_{TEG}) now, not only consists of the TE-materials resistance, but additionally contains the interconnect, and the contact resistances between them. By differentiating P with respect to R_L it can be shown that the maximum power output occurs where the module resistance is equal to the load resistance ($R_{TEG} = R_L$).

$$P_{max} = \frac{N(\alpha_p - \alpha_n)^2 \Delta T^2}{4 R_{TEG}} \tag{1.8}$$

Conversion efficiency is generally defined as the ratio of electrical power produced (P_{elec}) to the thermal energy supplied at the hot side (Q_H). When operated under optimal external load, a module's conversion efficiency (η) can be written as

$$\eta = \frac{P_{elec}}{Q_H} = \frac{\Delta T}{T_H} \cdot \frac{\sqrt{1 + ZT} - 1}{\sqrt{1 + ZT} + \frac{T_C}{T_H}} \tag{1.9}$$

with the hot and cold side temperatures T_H and T_C, and the total temperature gradient across the module ΔT=T_H-T_C. Here Z has the same meaning as stated above, just for the whole module.[37]

It is generally accepted that a $ZT \geq 1$ is required to achieve a sufficiently efficient energy conversion ($\approx$ 10%). In order to compete with state-of-the-art heat pumps, a ZT of ~ 3 would be necessary. Although record zT values of 2.5 have been reported in some materials on a lab-scale, we will probably not see such high efficiency modules in the near

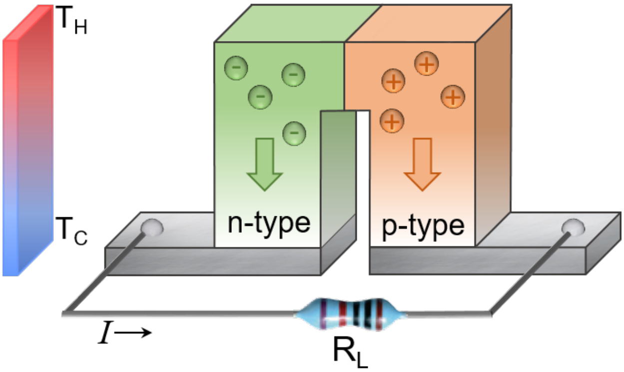

Figure 1.5: Illustration of a direction p-n junction thermoelectric generator.

future.[38] As a rule of thumb, the zT is halved when moving from the material scale to the module, as additional parasitic losses occur. They mainly arise from the additional thermal and electrical resistances of the contact layers between metal-interconnect and TE-legs. Besides the electric and thermal shortcomings of the interconnects in general, the hot side interconnect poses some additional weaknesses to the modules performance potential. The high temperatures, which the hot side is exposed to, require the use of noble metal interconnects, high melting solders, and usually additional buffer layers to avoid oxidation, degradation and reactions between the TE-leg, solder and interconnect. This has led to the proposition of omitting the hot-side interconnect all together, establishing a direct-junction thermoelectric generator.[39] The direct junction TEGs require less noble materials and are thus potentially cheaper and easier to fabricate. Especially the so-called "large-area p-n junction" design, where p- and n-materials are in contact over the whole temperature gradient, has the potential to greatly facilitate large scale production.[40, 41]

1.5 Starting point and motivation

The direct junction approach, however, does not only have advantages, but poses some challenges as well. With the two semiconductors being in direct contact with each other at high temperatures, phenomena like interdiffusion, dopant de-mixing, and reactions forming intermediate phases are to be expected and can severely impair the semiconductor and thermoelectric properties. To a certain extend, this can be circumvented through the targeted use of coexistent p-n pairs such as ZnO and NiO, which show finite mutual solid solubilities and do not form any intermediate phases.[42] However, this approach does not address the other major problem, that of rectifying diodes. When in direct contact, p- and n-type semiconductors typically form a charge depletion layer resulting in a diode like behavior. This leads to a high parasitic resistance between the two semiconductors, since Seebeck voltages generated by the materials are too low to overcome the p-n junction barrier layer. To still make the direct p-n junction TEGs work, one would have to operate them at high enough temperatures to overcome the barrier by thermionic emission, or to find a way to build p-n junctions without rectifying characteristics. The motivation for this PhD project was the discovery of a new pair of p- and n-type thermoelectric oxides, which would be coexistent, composed of cheap and abundant elements, high temperature stable, and ideally additionally dope each other p and n to avoid the problem of dopant interdiffusion. In the course of the project, a new approach to circumvent the rectifying issues of the p-n junctions was uncovered. We were able to identify a broken-gap junction that shows non-rectifying characteristics, which is a known approach in the field of tandem photovoltaic cells. The targeted design of broken-gap junctions could give the direct junction thermoelectrics a significant advantage over their diode-like relatives and thus potentially enable the field of thermoelectrics to take a significant step forward.

2 Theory

In this chapter an overview on selected theoretical backgrounds relevant to the materials and phenomena treated in this thesis are given. Thermoelectric properties for band conducting metals and semiconductors will be derived in an introduction to the Boltzmann transport theory. This is followed by a section treating localized states, like polarons, where the relevance of the band formalism fades. Finally, properties of electronic interfaces are presented. The treatment of defect chemistry can be found in the materials review section, where the relevant concepts are derived and explained using specific example materials.

2.1 The Boltzmann theory of transport

This section gives an overview on relevant theoretical descriptions of the thermoelectric effects in the Boltzmann transport theory. Expressions for the conductivity, Seebeck coefficient and thermal conductivity for metals and semiconductors are derived. I tried to keep this section as short, yet as complete as possible. While the mathematical details would go beyond the scope of the chapter the interested reader is referred to classic solid state physics books.[43–46]

2.1.1 General thermoelectric transport equations

For a solid in thermodynamic equilibrium the number of electrons occupying an energy state E is given by the Fermi-Dirac distribution

$$f_0(E) = \frac{1}{\exp\left(\frac{E-E_F}{k_B T}\right) + 1} \tag{2.1}$$

where k_B is Boltzmann's constant, T is the absolute temperature, and E_F is the Fermi energy. By applying external perturbations to the system in form of e.g. an electrical field or a temperature gradient, the system is forced out of its equilibrium state. Electrons accelerated by a field, or moving along a concentration gradient, experience scattering events pushing the system back to their equilibrium state. The Boltzmann transport equation describes the behavior of a system in non-equilibrium state. The evolution of an electron distribution $f(t, s, k)$ at time t, space s, and wave vector k $(mv = \hbar k)$ is described by

$$\frac{df}{dt} = \left.\frac{\partial f}{\partial t}\right|_{field} + \left.\frac{\partial f}{\partial t}\right|_{diff.} + \left.\frac{\partial f}{\partial t}\right|_{scatter} \tag{2.2}$$

Assuming Liouville's theorem on the invariance of volume occupied in phase space, the distribution change rate due to diffusion is given by

$$\left.\frac{\partial f}{\partial t}\right|_{diff.} = -\dot{s}\nabla_s f \tag{2.3}$$

The rate at which the distribution function changes due to acceleration of electrons in k-space from an external electric field can be expressed as

$$\left.\frac{\partial f}{\partial t}\right|_{field} = -\dot{k}\nabla_k f \tag{2.4}$$

While the terms for diffusion and field perturbation are rather easily derived, the scattering term is more difficult to solve. Widely used is the relaxation time approach. By introducing a characteristic time τ, that a perturbed system (f) takes to relax back to its equilibrium state (f_0), the scattering term can be written as

$$\left.\frac{\partial f}{\partial t}\right|_{scatter} = -\frac{f - f_0}{\tau} \tag{2.5}$$

The relaxation time τ is often expressed as $\tau = \tau_0 E^r$, with r taking half integer values, dependent on the scattering mechanism applied. τ_0 is energy-independent, but can be temperature-dependent. The most commonly used scattering mechanisms include: $r = -1/2$ for acoustic phonon scattering, $r = 3/2$ for ionized impurity scattering, and $r = 1/2$ for optical phonon scattering. The Boltzmann transport equation under steady-state conditions ($\frac{df}{dt} = 0$) in the relaxation time approximation then reads

$$-\frac{f - f_0}{\tau} = \dot{s}\nabla_s f + \dot{k}\nabla_k f \tag{2.6}$$

In order to solve this equation and obtain f we must introduce some simplifications. Let's assume an electric field is applied solely in x-direction and the solid to be an isotropic conductor ($\dot{s} = v$). Further, the perturbation is assumed to be small so the distribution function can be linearized ($f - f_0 \ll f_0$). If we now express the field term in form of a

Coulomb force ($\dot{k}\frac{\partial f}{\partial k} = -eEv\frac{\partial f}{\partial E}$), equation 2.6 can be formulated as

$$f(E) = v\tau\frac{\partial f_0}{\partial E}\left(\frac{\partial E_F}{\partial x} + \frac{E - E_F}{T}\frac{\partial T}{\partial x}\right) \tag{2.7}$$

In this form the distribution function can be used to derive some figures, relevant for thermoelectrics: Conductivity, Seebeck coefficient, and thermal conductivity. An expression for conductivity can be found from the general form of electric current density j (the sign denotes directionality of the current flow)

$$j = \pm\int_0^\infty evD(E)f(E)dE \tag{2.8}$$

where $D(E)$ is the density of states and e the elemental charge. By substituting Equation 2.7 into Equation 2.8, one obtains

$$j = \pm\int_0^\infty ev^2\tau D(E)\frac{\partial f_0}{\partial E}\left(\frac{\partial E_F}{\partial x} + \frac{E - E_F}{T}\frac{\partial T}{\partial x}\right)dE \tag{2.9}$$

As the electrical conductivity is defined as the ratio of current over the electric field ($\sigma = \frac{j}{\frac{1}{e}\frac{\partial E_F}{\partial x}}$), and in the absence of a temperature gradient ($\frac{\partial T}{\partial x} = 0$) the conductivity is obtained as

$$\sigma = e^2\int_0^\infty v^2\tau ED(E)\frac{\partial f_0}{\partial E}dE \tag{2.10}$$

The Seebeck coefficient can be obtained from its definition in Equation 1.1 and under open circuit conditions ($j = 0$)

$$\alpha = \pm \frac{1}{eT} \left(\frac{\int\limits_0^\infty v^2 \tau E D(E)(E - E_F) \frac{\partial f_0}{\partial E} dE}{\int\limits_0^\infty v^2 \tau E D(E) \frac{\partial f_0}{\partial E} dE} \right) \tag{2.11}$$

To derive the electron thermal conductivity, the general form of the heat current density q_e is used (the heat flux is the sum of heat each electron carries times the drift velocity is $q_e = nv(E - E_F)$)

$$q_e = \pm \int\limits_0^\infty v(E - E_F) D(E) f(E) dE \tag{2.12}$$

Similar to the procedure above, Equation 2.7 can be substituted into Equation 2.12

$$q_e = \int\limits_0^\infty v^2 \tau D(E)(E - E_F) \frac{\partial f_0}{\partial E} \left(\frac{\partial E_F}{\partial x} + \frac{E - E_F}{T} \frac{\partial T}{\partial x} \right) dE \tag{2.13}$$

With the definition of thermal conductivity ($\kappa = \frac{q}{\frac{\partial T}{\partial x}}$) and in the absence of an electric field ($j \neq 0$) the electron thermal conductivity reads

$$\kappa_e = \frac{1}{T} \int\limits_0^\infty v^2 \tau D(E) E^3 \frac{\partial f_0}{\partial E} dE \tag{2.14}$$

The derivations stated above can be compressed by introducing the integral[†]

$$K_n = \int\limits_0^\infty v^2 \tau E D(E)(E - E_F)^n \frac{\partial f_0}{\partial E} dE \tag{2.15}$$

and the transport coefficients above can be expressed as functions thereof[‡]

$$\sigma = e^2 K_0 \tag{2.16}$$

$$\alpha = \frac{1}{eT} \frac{K_1}{K_0} \tag{2.17}$$

$$\kappa_e = \frac{K_2}{T} \tag{2.18}$$

Electric current and heat flux density can likewise be expressed with the transport coefficients

$$j = e^2 K_0 E + \frac{e}{T} K_1 (-\nabla T) \tag{2.19}$$

$$q_e = e K_1 E + \frac{1}{T} K_2 (-\nabla T) \tag{2.20}$$

By simple substitution we end up with the classic descriptions of electric, and thermal current density

$$j = \sigma E - \alpha \sigma \nabla T \tag{2.21}$$

$$q_e = \alpha T \sigma E - \kappa_e l \nabla T \tag{2.22}$$

[†] Here n is an index that takes positive integer values, not to be confused with the electron density.

[‡] In case of an electric field being present ($j = 0$) the electron thermal conductivity reads $\kappa_e' = \frac{K_2}{T} - \frac{1}{T^2} \frac{K_1^2}{K_0}$

For $\nabla T = 0$, the field terms can be eliminated and the two currents combined in one expression

$$\frac{1}{j}\frac{q_e}{T} = \alpha \tag{2.23}$$

The left side corresponds the ratio of an entropy current to an electric current. Thus the Seebeck coefficient is often interpreted as the entropy per charge carrier.

2.1.2 Metals

The generally valid transport equations can be used to derive simpler expressions for metals under some reasonable assumptions. In a parabolic band with effective mass m^* the density of states is given by

$$D(E) = \frac{1}{2\pi^2}\left(\frac{2m^*}{\hbar}\right)^{\frac{3}{2}} E^{\frac{1}{2}} \tag{2.24}$$

The drift velocity can be expressed as a third of the total electron kinetic energy $v^2 = \frac{2E}{3m^*}$. Equation 2.10 can then be expressed as

$$\sigma = -\int_0^\infty \sigma(E)\frac{\partial f_0}{\partial E}dE \quad \text{,with} \quad \sigma(E) = \frac{2(2m^*)^{\frac{1}{2}}}{3\pi^2\hbar^3}e^2E^{\frac{3}{2}}\tau \tag{2.25}$$

For metals ($\frac{E_F}{k_BT} \gg 1$) Equation 2.10 can be approximated by a Taylor series.[47]

$$\sigma = -\int_0^\infty \sigma(E)\frac{\partial f_0}{\partial E}dE = \sigma(E_F) + \frac{\pi^2}{6}(k_BT)^2\frac{\partial^2\sigma(E)}{\partial E^2}\bigg|_{E=E_F} \tag{2.26}$$

It becomes clear that only the electrons close to the Fermi energy contribute to the conductivity. By consequently dropping the second term the conductivity simplifies to

$$\sigma = \frac{2(2m^*)^{\frac{1}{2}}}{3\pi^2\hbar^3} e^2 E_F^{\frac{3}{2}} \tau \tag{2.27}$$

For metals where $(E - E_F)/k_B T \ll 0$, the Fermi-energy can be estimated from a free electron model and one arrives at the Drude model for conductivity, with electron mobility u

$$\sigma = \frac{ne^2\tau}{m^*} = neu \tag{2.28}$$

An expression for the thermal conductivity can be obtained by keeping the higher order term of the Taylor series in Equation 2.26, which will lead us to the Wiedemann-Franz law.

$$\frac{\kappa_e}{\sigma T} = \frac{\pi^2}{3}\left(\frac{k_B}{e}\right)^2 \tag{2.29}$$

The right hand side of the equation is the already mentioned Lorenz factor (Equation 1.6). By applying the same Taylor-series formalism as described for Equation 2.26 to Equation 2.11 it can be shown that the Seebeck coefficient is obtained as

$$\alpha = -\frac{\pi^2}{3e} k_B^2 T \frac{\partial \ln\sigma(E)}{\partial E}\bigg|_{E=E_F} \tag{2.30}$$

This representation is the well-known Mott formula. Substituting Equation 2.27 for conductivity and introducing an acoustic phonon scattering exponent $r = -1/2$, following the same conventions as above, the Seebeck coefficient ca be simplified to

$$\alpha = -\frac{2k_B^2}{3e\hbar^2} m^* T \left(\frac{\pi}{3n}\right)^{\frac{2}{3}} \tag{2.31}$$

2.1.3 Semiconductors

The expressions for semiconductors follow the derivations shown above and are thus shown somewhat compressed. However, the properties of semiconductors depend more heavily on the scattering mechanism of the electrons and are therefore often given as functions of the latter. In a non degenerate semiconductor where $\frac{(E-E_F)}{k_B T} \gg 1$, Equation 2.1 is reduced to a classical Maxwell-Boltzmann distribution function

$$f_0(E) \approx \exp\left(-\frac{E-E_F}{k_B T}\right) \tag{2.32}$$

Inserting this distribution function into Equation 2.10 and using a parabolic band approach as in Equation 2.24 one end up with an expression for conductivity very similar to that of metals

$$\sigma = \frac{ne^2 \langle\tau\rangle}{m^*} \tag{2.33}$$

with the exception that the relaxation time is replaced by the average relaxation time, which is given by

$$\langle\tau\rangle = \frac{\int\limits_0^\infty \tau E^{\frac{3}{2}} \exp\left(-\frac{E}{k_B T}\right) dE}{\int\limits_0^\infty E^{\frac{3}{2}} \exp\left(-\frac{E}{k_B T}\right) dE} \tag{2.34}$$

In the same manner an expression for the Seebeck coefficient and thermal conductivity, including the scattering exponent r is obtained as

$$\alpha = -\frac{k_B}{e}\left[\frac{-E_F}{k_B T} + \left(\frac{5}{2} + r\right)\right] \tag{2.35}$$

$$\frac{\kappa_e}{\sigma T} = L = \left(\frac{k_B}{e}\right)\left(r + \frac{5}{2}\right) \tag{2.36}$$

Note that the Lorentz number is to first approximation independent of the Fermi energy for a constant r.

The electron density can be expressed using a Gamma function, which is known as the Boltzmann approximation

$$n = \frac{1}{\sqrt{2}}\left(\frac{m_e^* k_B T}{\hbar^2 \pi}\right)^{\frac{3}{2}} \exp\left(\frac{E_F - E_C}{k_B T}\right) \tag{2.37}$$

The same expression is valid for holes (p) (replace $E_F - E_C$ with $E_V - E_F$) and the total charge carrier concentration in an intrinsic semiconductor, can thus be written as a function of the band gap.

$$\sqrt{np} = \frac{1}{\sqrt{2}}\left(\frac{k_B T}{\hbar^2 \pi}\right)^{\frac{3}{2}} (m_e^* m_h^*)^{\frac{3}{4}} \exp\left(\frac{-E_g}{2 k_B T}\right) \tag{2.38}$$

In praxis mostly doped semiconductors are of interest and an estimate for the carrier concentration can be made from the doping level, assuming fully ionized dopants.

2.2 Polaron transport

The band transport description given above is relatively successful for conventional semiconductor systems. Generally, however electrons moving through a lattice interact with its surrounding and may distort it. In polar lattices, like e.g. in metal oxides, the lattice deformation can lead to a localization of the electron (or hole). The electron coupling to its own lattice polarization is known as "self-trapping", and can be treated as a quasi-particle called polaron. Weakly interacting polarons, called large- or Fröhlich polarons, can still be treated in a band-like transport with an increased effective mass. Strongly interacting, small (Holstein) polarons are self-trapped in a local potential well. Their transport through the lattice can be described by classic diffusion theory, where mobility can be related to the diffusion constant by the Einstein relation ($D = uk_BT$).[48, 49] The mobility can then be described with an activation energy E_u that has to be overcome in order to jump from one potential well to another.

$$u = \frac{u_0}{T}\exp\left(\frac{-E_u}{k_BT}\right) \tag{2.39}$$

The exponential prefactor u_0 takes different forms depending on whether the hopping is adiabatic or non-adiabatic. In the adiabatic case the hopping frequency is larger than the phonon frequency and the hopping probability during an excitation is unity. In the non-adiabatic case the hopping probability is low, as its frequency is lower than the optical

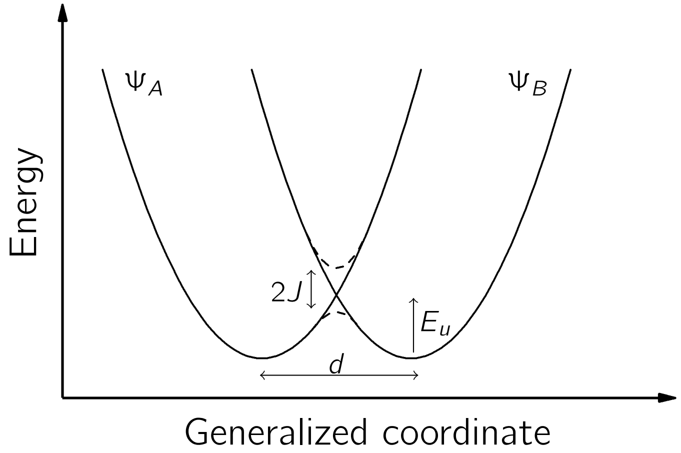

Figure 2.1: Configuration coordinate model depiction after the Marcus-Emin-Holstein-Austin-Mott theory for symmetric polaron transfer.[44] The carrier requires to overcome the potential energy E_u to "hop" from potential-well Ψ_A to Ψ_B. Electron overlap J between the two localized states is indicated by the dashed curves. The larger the interaction, the more stable a delocalized configuration. $2J$ can be interpreted as the polaron band width. Note that E_u is the non-adiabatic hopping energy, in the adiabatic case the hopping energy becomes $E_u - J$.

phonon frequency.

$$u_0 = \begin{cases} \frac{zed^2\nu_o}{k_B} & \text{adiabatic} \\ \frac{zed^2}{2k_B}\frac{J^2}{2h}\sqrt{\frac{\pi}{4E_uT}} & \text{non-adiabatic} \end{cases} \tag{2.40}$$

In the equations above d denotes the jump distance, z the number of nearest neighbors, ν_o the maximum optical phonon frequency, and J the overlap integral (h, e, T, and k_B have their usual meanings). To evaluate which of the cases applies to a certain material, the adiabatic paramter η_2 can be determined, as a graphic evaluation is often difficult, with both mechanisms producing satisfactory fits to experimental data.

$$\eta_2 = \frac{J^2}{h\nu_o}\sqrt{\frac{1}{E_u k_B T}} \tag{2.41}$$

The adiabatic parameter takes values of $\eta_2 \ll 1$ for non-adiabatic hopping, and $\eta_2 \gg 1$ in the adiabatic regime.[50]

The formation of small polarons is often associated with the change in oxidation state of a specific ion in the lattice. Polaron conductors can thus frequently be found in the family of transition metal oxides, due to their inherent multivalency. In transition metal oxides, especially with partially filled d-shells, the strong Coulomb interaction between the d-electrons gives rise to complex transport properties. These material systems are referred to as strongly correlated electron systems, and have proven very useful for many applications in solid state physics, including thermoelectrics. One of the most prominent examples for thermoelectrics, can be found in Co (usually a p-type conductor), where a hole can be viewed as an oxidized species $\mathrm{Co}^{3+} + \mathrm{h}^+ \rightarrow \mathrm{Co}^{4+}$. The Seebeck coefficient of small polaron conductors at high temperatures is equal to the classic mixing entropy of the two states, which came to be known as the Heikes formula.[45, 51]

$$\alpha_H = \frac{k_B}{e}\ln\left(\frac{x}{1-x}\right) \tag{2.42}$$

Here x denotes the site fraction of charge carriers, in the cobalt example

$$x = \frac{[\mathrm{Co}^{4+\;\bullet}_{\mathrm{Co}^{3+}}]}{[\mathrm{Co}^{4+\;\bullet}_{\mathrm{Co}^{3+}}] + [\mathrm{Co}^{3+\;X}_{\mathrm{Co}^{3+}}]} \tag{2.43}$$

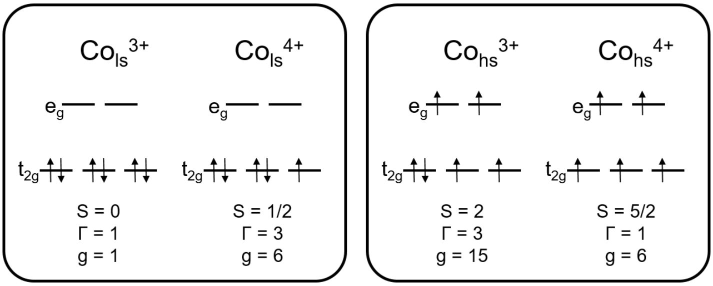

Figure 2.2: Electronic degeneracy of Co^{3+} and Co^{4+} in low- and high spin state for an octahedral crystalfield.

It builds on the consideration of spinless fermions, which can not simultaneously occupy the same site. However, neglecting the contributions of spin and orbital degeneracy to the configurational entropy led to an inadequate description of the Seebeck coefficient behavior in the layered cobaltites (see Section 3.1). Thus, an extension to the Heikes formula was proposed by Koshibae *et al.*, which includes spin-orbit degeneracies g_i and has since been able to successfully describe the Seebeck coefficient behavior of numerous open shell transition metal oxides.[52] The electronic degeneracy g_i of state A and B is calculated as the product of spin and orbital degeneracy.

$$g_i = g_i^{spin} g_i^{orbital} \tag{2.44}$$

An exemplary representation of the electronic degeneracy of Co^{3+} and Co^{4+} in an octahedral crystal field is depicted in Figure 2.2 It becomes clear that this treatment includes high spin - low spin transitions, in addition to different oxidation states. The spin orbit contributions to the entropy term in Heikes formula are included as the ratio of electronic degeneracies of the two states.

$$\alpha = \frac{k_B}{e} \ln\left(\frac{g_A}{g_B}\frac{x}{1-x}\right) \tag{2.45}$$

This modified Heikes formula has also been used in Publication I to successfully describe the charge carrier concentration from Seebeck measurements in the multivalent iron compound Fe_2WO_6. A complete theoretical description of polaron conductors in general is difficult, as the transitions from large to small polaron are often fluid and each correlated system exhibits its own peculiarities dependent on crystal structure, magnetic ordering, temperature, and doping.

2.3 Electronic interfaces

In the previous section, the bulk properties of materials were examined and discussed. In the following section we want to take a closer look at the properties of interfaces between materials, in particular semiconductors. A thermoelectric generator is built from several individual materials and the interface properties between these have significant impact on the overall device performance.

2.3.1 Semiconductor p-n junctions

A p-n junction is a contact between two semiconductors of opposite polarity. For simplicity we will treat a homojunction between an acceptor doped and a donor doped semiconductor of the same host material. When brought into contact, thermal equilibration will lead to a constant

Fermi level across the junction, giving rise to a "built-in" potential Φ_{bi}, equal to the difference in the Fermi levels of the individual semiconductors prior to the contacting. The Fermi energies can be obtained from the dopant concentrations (N_D and N_A)[†] over the intrinsic carrier concentrations n_i.

$$\Phi_{bi} = E_{f_p} - E_{f_n} = \frac{k_B T}{e} \ln\left(\frac{N_D N_A}{n_i^2}\right) \tag{2.46}$$

The potential is the result of diffusion current of electrons from the n-type to the p-type and holes from the p-type to the n-type, which stagnates in dynamic equilibrium with the drift current arising from the resulting space charge region.

$$\begin{aligned} j_n &= eu_n\Phi + eD_n\frac{\partial n}{\partial x} \\ j_p &= eu_p\Phi - eD_p\frac{\partial p}{\partial x} \end{aligned} \tag{2.47}$$

Here $u_{n/p}$ and $D_{n/p}$ are the carrier mobilities and diffusion coefficients, and Φ is the electrical potential along the one dimensional diffusion direction x perpendicular to the p-n junction. In equilibrium the sum of electron and hole current is zero and the space charge region building up on both sides of the junction is the charge depletion layer effectively blocking current flow. An exemplary band diagram depicting the flat band positions prior to contact, and the band bending at thermal equilibrium is shown in Figure 2.3. The band bending and the depletion layer

---

[†] D and A denote the index for donor and acceptor, respectively.

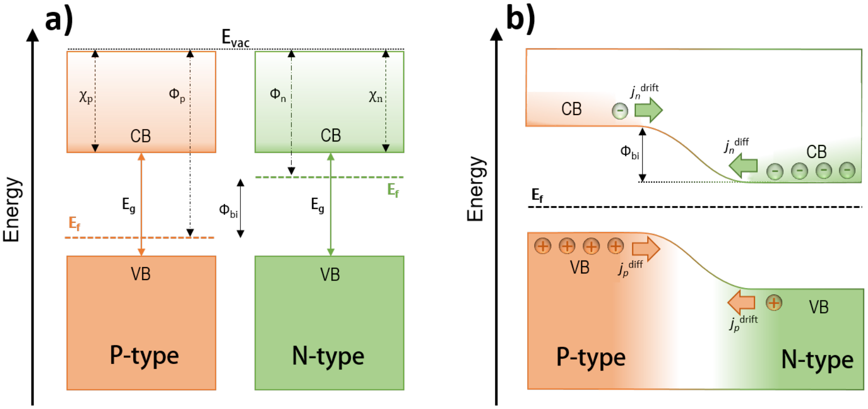

Figure 2.3: Exemplary band diagram of a p-n homojunction. a) Flat band condition prior to the contact where the reference energy is the vacuum level. b) Equilibrium condition with band bending where the common Fermi energy is the new reference energy.

width can be calculated from the Poisson-Boltzmann equation.

$$-\frac{\partial^2\Phi}{\partial x^2} = \frac{\rho(x)}{\epsilon_r} \tag{2.48}$$

Where $\rho(x)$ is the local charge density and ϵ_r is the relative permittivity of the material. The equation can be solved in the full depletion approximation where the field is taken to be confined to the depletion region, which has no free carriers ($n(x) = p(x) = 0$). We expand the potential Φ by an externally applied V_{ext} to be able to express the depletion layer width under non-equilibrium conditions.

$$w(V_{ext}) = \sqrt{\frac{2\epsilon_r}{e}\left(\frac{1}{N_D} + \frac{1}{N_A}\right)(\Phi_{bi} + V_{ext})} \tag{2.49}$$

We can see now, that applying an external voltage to the junction in

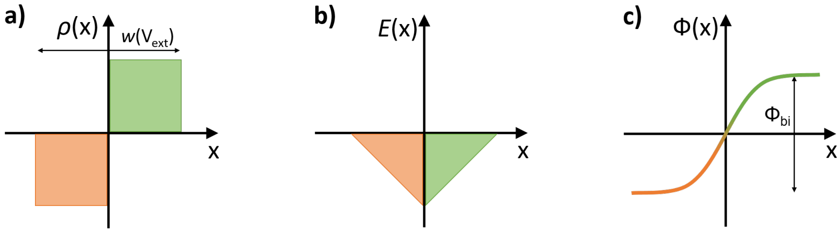

Figure 2.4: a) charge density, b) field, and c) potential along the x-axis, perpendicular to the p-n junction, in full depletion approximation for a p-n junction with symmetric charge carrier densities.

the same polarity as the built in potential will result in a growth of the depletion layer. Switching polarity on the external voltage will lead to a shrinking of the depletion layer and a decrease in resistance. When the external bias equals the built in potential, the drift current can no longer counteract the diffusion current, and the depletion layer collapses, allowing charge carriers to freely pass the junction, with the current increasing exponentially with applied voltage. A typical diode current voltage relation (I-V characteristic) is depicted in Figure 2.5 b. The total dependency of current on applied external voltage is described by the Schockley equation.[†]

$$\begin{aligned} j &= j_S \left(\exp\left(\frac{eV_{ext}}{\nu_{id} k_B T} \right) - 1 \right) \\ j_S &= e n_i^2 \left(\frac{D_p}{L_p N_D} + \frac{D_e}{L_e N_A} \right) \end{aligned} \tag{2.50}$$

j_S is called the reverse saturation current containing diffusion coefficients $D_{n/p}$, diffusion lengths $L_{n/p}$, and an ideality factor ν_{id} that takes

---

[†] The Schockley equation is given in the dimension of current density j which can be obtained from the experimentally accessible absolute current I and sample dimensions.

values between 1 and 2. The equation suggests a decrease in current density with increasing temperature. The charge carrier concentration and diffusion coefficients themselves, however are strong functions of temperature, but remain almost independent of V_{ext}. Thermally generated charge carriers can diffuse across the junction and generate a recombination current. While this saturation current, also known as leakage current, remains small at low temperatures, it can significantly contribute to the total current at high temperatures and even lead to a breakdown of the characteristic diode curve. This often leads to ohmic characteristics of p-n junctions at very high temperatures.

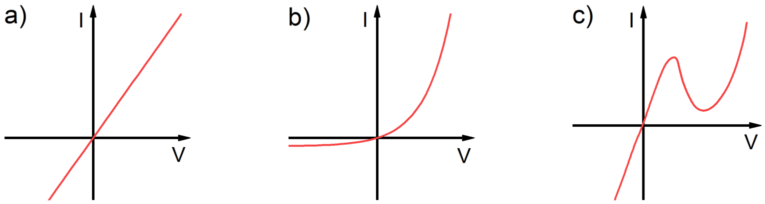

Figure 2.5: Schematic I-V characteristics for a) ohmic, b) rectifying, and c) tunneling junctions.

2.3.2 Non-rectifying p-n junctions

Under certain circumstances a p-n junction can be designed to be non-rectifying. This is desirable in e.g. tandem solar cells, where a serial connection of p-n junctions would lead to an unintended charge accumulation between the junctions. One possibility is the use of tunnel junctions (TJ). TJs can be constructed as both homo- or heterojunctions and rely on heavy doping of the interface in both n- and p- semi-

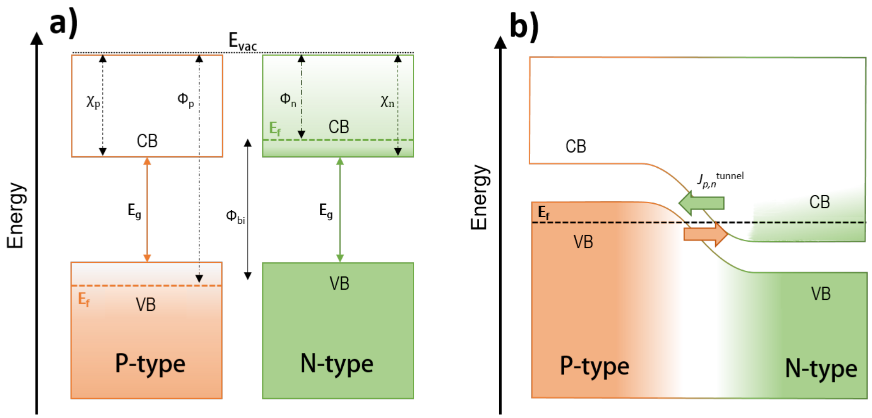

Figure 2.6: Schematic band diagram of a highly doped p-n junction forming a tunnel junction. a) Flat band condition prior to the contact where the reference energy is the vacuum level. b)Equilibrium condition with band bending where the common Fermi energy is the new reference energy.

conductors. The heavy doping shifts the Fermi level of the n-type into the conduction band and the Fermi level of the p-type into the valence band. The high charge carrier concentrations lead to a very thin depletion barrier width at the junction through which quantum mechanical tunneling of the charge carriers, directly between the n-type conduction band and the p-type valence band is possible. Under reverse bias the overlap between p-type valence band and the n-type conduction band will increase steadily and the current will increase linearly with the applied voltage. Under low forward bias the current will likewise follow the applied voltage linearly. The overlap between the p-type valence band and the n-type conduction band will, however, decrease steadily until it reaches a critical point at which the tunneling current breaks down and the junction behaves like a normal rectifying diode. The *I*-*V* characteristics will show a typical "negative resistance" region during the tunneling current breakdown, depicted in Figure 2.5 c.[53, 54]

The second possibility is the formation of a broken gap junction (BGJ), which forms in the special case of a p-n heterojunction where the electron affinity[†] of the n-type semiconductor is greater than the sum of the electron affinity and the band gap of the p-type semiconductor.

$$\chi_n > \chi_p + E_{g,p} \tag{2.51}$$

With the valence band of the p-type being higher in energy compared to the conduction band of the n-type (and consequently their respective Fermi levels), thermal equilibration will result in an electron flow from the p-type to the n-type. The consequential charge accumulation layer, leaves both semiconductors automatically highly doped on both sides of the junction, independent of the individual semiconductors own doping levels.[55] Under applied bias electrons and holes now recombine directly between the n-type conduction band and the p-type valence band, across the accumulation region, regardless of the applied voltage direction. Thus, broken gap junctions show linear *I*-*V* characteristics with no rectification (Figure 2.5 a). Charge carriers are believed to be strongly accelerated, when entering the charge accumulation zone and cross the junction with high kinetic energy with a ballistic transport mechanism.[56, 57]

[†] The electron affinity here refers to the energy difference between the conduction band minimum of the semiconductor and the vacuum level and should not be confused with the electron affinity E_{ea} as defined in atom physics.

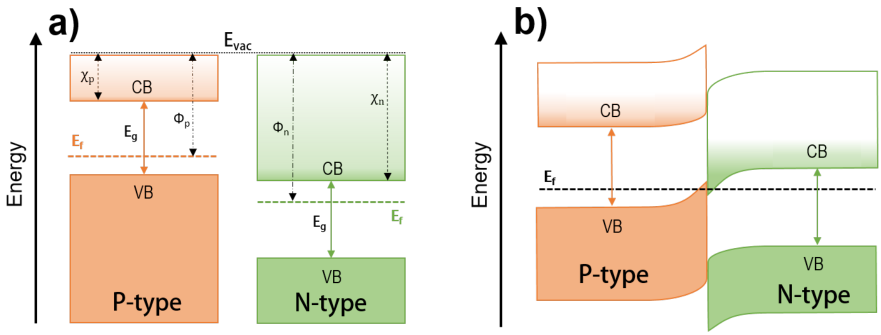

Figure 2.7: Schematic band diagram of a p-n heterojunction with broken gap alignment. a) Flat band condition prior to the contact where the reference energy is the vacuum level. b) Equilibrium condition with band bending where the common Fermi energy is the new reference energy.

2.3.3 Metal-semiconductor junctions

An electric junction between a semiconductor and a metal can either form an ohmic contact, or a rectifying contact, called Schottky contact. Whether the junction forms an ohmic or a Schottky contact, is described by the Schottky-Mott rule. It gives an expression for the Schottky barrier height Φ_b from the metal's work function Φ_M and the electron affinity of the semiconductor χ_{sc}.

$$\Phi_b = \Phi_M - \chi_{sc} \tag{2.52}$$

Small Schottky barriers exhibit ohmic contact behavior, whereas substantial Schottky barriers are rectifying. As a rule of thumb the Schottky-Mott rule can be simplified to: Large work function metals form ohmic contacts with p-type semiconductors whereas small workfunction metals form ohmic contacts with n-type semiconductors. Although in theory correctly predicting the junction barrier height, in practice the junction characteristics are less sensitive to the metal workfunction but rather to the semiconductor energy states. Metal induced gap states or surface states, pinning the Fermi level, in reality often lead to a lower barrier height than predicted and ohmic behavior. For thermoelectrics an ohmic contact is in any case favored over a Schottky contact, as the rectifying behavior present a parasitic resistance, lowering the overall device performance.

3 Materials review

The following chapter will give a short review on some relevant oxide thermoelectric materials followed by an introduction of the materials class of transition metal tungstates, which are of relevance for this thesis. Traditionally thermoelectric materials have been discovered and investigated separately as individual materials and only later combined to a p-n pair in thermoelectric test modules. Throughout this work, an alternative approach was attempted by the targeted selection of a materials pair (p- and n-type), which show similar physical properties in order to exclude complications, like e.g. thermal expansion mismatch, reactions or interdiffusion at the development stage. A suitable pair can be found in the family of transition metal tungstates, of which an outline will be given in section 3.4.

3.1 Layered cobaltites

When Terasaki *et al.* fist reported on the thermoelectric properties of $Na_{0.5}CoO_2$ (NCO) in 1997, they discovered a large Seebeck coefficient of $\sim 100\ \mu VK^{-1}$ in conjunction with metallic conductivity ($200\ \mu\Omega$), resulting in a power factor of $50\,^{x}10^{-4}Wm^{-1}K^{-2}$ that could compete with the state-of-the-art thermoelectric material Bi_2Te_3 and a zT of ~ 1.[31]

Its structure consists of alternating layers of CdI_2 type CoO_2 and intercalated Na atoms, with the Na atoms donating their valence electrons to the CoO_2 layer resulting in a high charge carrier concentration. The combination of large Seebeck coefficient and high charge carrier density seemed contradictory at the time, but could be explained a few years later by Koshibae *et al.* by a modified Heikes formula which included the spin orbit contributions to the configurational entropy (see Equation 2.45).[52] With the sodium donating its valence electrons to the

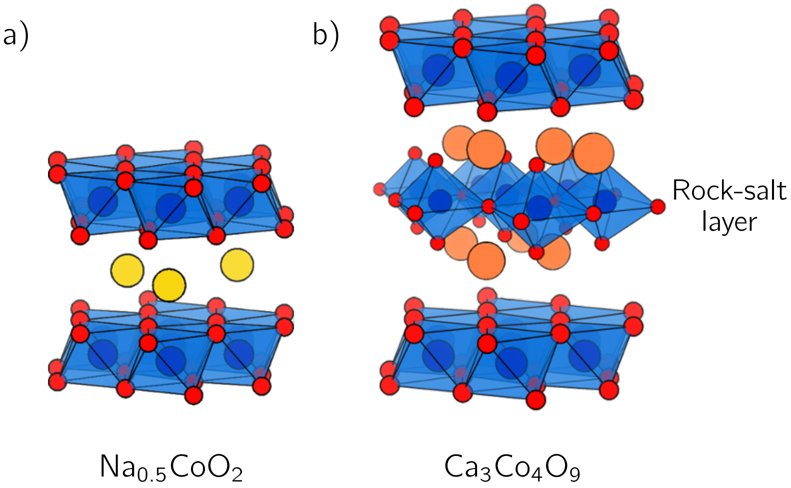

Figure 3.1: Crystal structure of layered cobaltites a) $Na_{0.5}CoO_2$ and b) $Ca_3Co_4O_9$.

CoO_2 layer, Co exists in two oxidation states Co^{3+} and Co^{4+}. As both states have different electronic configurations with different spin and orbital degeneracy, each charge carrier carries the difference in spin-orbit degeneracy as additional configurational entropy contributing to the Seebeck coefficient in the material. The modified Heikes formula and the determination of the electronic degeneracy have been described in Section 2.2. The surprising discovery sparked the research on thermoelectric oxide materials, especially correlated transition metal oxides, where the spin orbit contribution to the Seebeck coefficient can be used as screening tool to explore new materials like $Ca_3Co_4O_9$,[58] $Ca_3Co_2O_6$,[59] $La_{1-x}Sr_xCoO_3$,[60] $CaMnO_3$,[61] $LiMn_2O_4$,[62] and $SrFeO_3$.[63] Since NCO shows limited thermal stability due to the mobility of Na and a tendency to hydrate, it was quickly recognized that similar layered structures and electronic properties could also be found in the related compound $Ca_3Co_4O_9$ (CCO-349). Here the CoO_2 layers are separated by a misfitting rock salt structured Ca_2CoO_3 layer, making CCO-349 a complex material with an incommensurate crystal structure. Similar to Na in NCO, the rock-salt layer donates electrons into the CoO_2 layer, while the misfit between the layers leads to a remarkably low thermal conductivity. Undoped samples already exhibit a thermal conductivity as low as 1.8 $Wm^{-1}K^{-1}$, which could further be decreased down to below 1 $Wm^{-1}K^{-1}$ when doped with rare earth elements like Yb or Lu.[58, 64] While publications on single crystalline CCO-349 report figures of merit of up to $zT = 0.87$,[26] the more application relevant poly-crystalline reports commonly reach $zT \approx 0.3$.[65] The most popular dopants for CCO proved to be Bi and Ag, increasing both conductivity and Seebeck coefficient, while simultaneously reducing the thermal conductivity.[66, 67] Several publications have indicated that an oxygen-nonstoichiometry in the rock-salt layer allows for tuning of the charge carrier concentration in CCO-349.[68, 69] The layered cobaltites are by far the highest performing p-type thermoelectric oxides and their success has inspired and fueled a lot of research in other materials.

3.2 Perovskites

The perovskite family with the general formula ABX_3 offers the unique possibility to explore a large amount of element compositions through its immense structural tolerance. The most successful candidates for thermoelectrics oxides from the family of perovskites are $SrTiO_3$ and $CaMnO_3$, where the high degree of spin degeneracy of the transition metal d-orbitals, like in the layered cobaltites, is positively reflected in a high Seebeck coefficient.

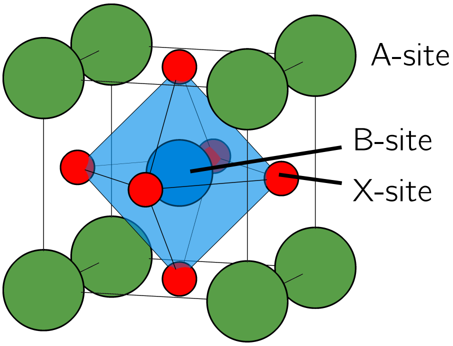

Figure 3.2: Cubic perovskite crystal structure.

3.2.1 $SrTiO_3$

Pristine $SrTiO_3$ is an insulator with a band gap of 3.2 eV and is one of the few oxides that have been shown to exhibit both n- and p-type conductivity.[32] However, since the n-type properties can be established more easily and are more stable over larger temperature and p_{O_2} scales,

$SrTiO_3$ is almost exclusively discussed as an n-type thermoelectric material. Like all perovskite structures, it can be doped on all of the three sites, whereby single or double doping on the A and B sites are the most common ones. Higher valent donor dopants are the elements of choice to reduce the Ti^{4+} to Ti^{3+} and increase the charge carrier concentration. Trivalent lanthanides are the most commonly chosen A site dopants, with La being the most frequently investigated dopant, resulting in figures of merit between 0.1-0.25.[30, 70] B site doping is less effective but has shown to positively influence the thermal conductivity when heavy transition metals like Nb are used in rather large amounts of up to 15%.[71] Doping both A and B site, appears to improve the electrical properties and simultaneously reduce the thermal conductivity. Major improvements on the figure of merit could be achieved by nanostructure engineering through spark plasma sintering or the targeted introduction of nano-grained secondary phases, reaching zT values of 0.37 at $\sim$770 °C.[72] The utilization of oxygen vacancies as donor dopants has been successfully demonstrated to boost electrical properties, while effectively scattering phonons in A-site deficient tantalum doped $Sr_{1-x/2}Ti_{1-x}Ta_xO_{3-\delta}$, reaching a zT value of 0.3.[73] Reduced Ti^{3+} however, tends to oxidize to its preferred Ti^{4+} state above ca. 400 °C, which severely limits the use of $SrTiO_3$ in air.[74]

3.2.2 $CaMnO_3$

$CaMnO_3$ is another perovskite structured n-type thermoelectric, which has a lower conductivity compared to $SrTiO_3$, Mn however, is much more stable in various oxidation states and remains reducible in air even at high temperatures. The room temperature orthorhombic crystal structure of $CaMnO_3$ changes to a cubic symmetry at high temperatures, which has been shown to beneficially influence the electronic conduction properties.[75] Donor doping to increase the n-type charge carrier concentration is realized by doping with trivalent elements, mostly lanthanides and Bi, on the A side and heavy transition metals on the B side. The most commonly used elements for B side doping are Nb, Ta, W, and V. Co-doping with Bi and V typically reaches zT values of 0.21 at 800 °C,[76, 77] and could be further improved up to 0.3 by nano-structuring.[28] In undoped samples $CaMnO_{3-\delta}$, the charge carrier concentration can be increased by the formation of oxygen vacancies at high temperatures. This improves the electrical conductivity and consequently the thermoelectric properties, however the conductivity passes through a maximum at $\delta = 0.12$ and drops at increased concentrations, which suggests a strong interaction between the polaron charge carriers.[78–80]

$CaMnO_3$ together with $Ca_3Co_4O_9$ has been used in several recent publications for the implementation of a direct junction TEG. However, since the two phases are not thermodynamically stable towards one another, an intermediate phase with the formula Ca_3CoMnO_6 is formed at the interface. This highly insulating phase, however, does not seem to impair the thermoelectric properties of the couple significantly and its role is subject to current research.[81, 82]

3.3 Binary oxides

3.3.1 NiO

NiO is the archetype of a p-type correlated semiconductor that has already proven to be interesting in various fields, including thermoelectrics.[83–85] It crystallizes in the cubic rock-salt structure and has a band gap of 3.6-4.0 eV.[86–88] In its pure form it is poorly conducting ($\sigma \lesssim 0.01$ Scm^{-1}) and has a high Seebeck coefficient (≈ 500 μVK^{-1}). However, when doped with mono-valent alkali metals such as Li or Na, the conductivity can be drastically increased to 10-100 Scm^{-1}, whereby the Seebeck coefficient is only moderately reduced to 200-300 μVK^{-1}. NiO achieves power factor values of up to $3^{\times}10^{-4}$ Wm^{-1}K^{-2}, however, the zT is limited by the rather high thermal conductivity of 5 Wm^{-1}K^{-1} to $zT \approx 0.01$-0.1.[89]

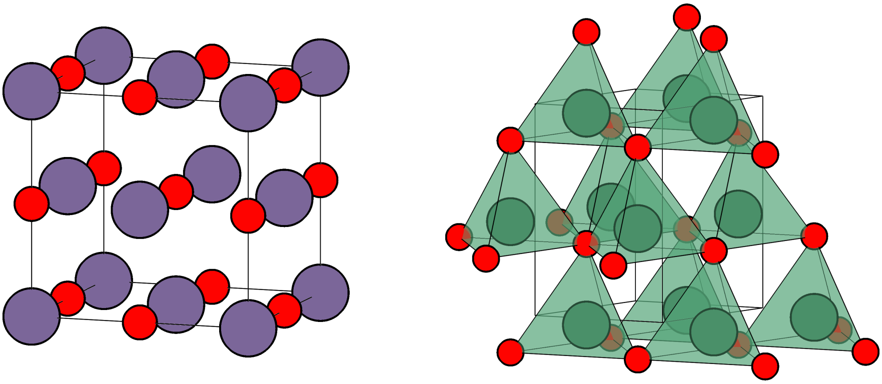

Figure 3.3: Left: Cubic rock-salt structure of NiO. Right: Hexagonal Wurzite type structure of ZnO.

3.3.2 ZnO

An alternative to the strongly correlated systems are high charge carrier mobility band conductors, like ZnO, exhibiting a more covalent bonding character. The n-type semiconductor with a band gap of $\sim$3.4 eV has been extensively studied for applications in the fields of solar cells, displays, and LEDs. It is attractive for thermoelectric applications not only because of its abundance, non-toxicity and thermal stability, but also due to its high conductivity. With a charge carrier mobility of up to 200 $\mathrm{cm^2V^{-1}s^{-1}}$ it has one of the highest of all oxide materials.[90] The charge carrier concentration can be adjusted to the optimum by doping with trivalent elements such as Al, Ga, or In, with which ZnO reaches power factors of 10-18^{x}10^{-4} $\mathrm{Wm^{-1}K^{-2}}$.[91] Despite this, the figure of merit only reaches about $zT = 0.3$ due to the very high thermal conductivity of 40-50 $\mathrm{Wm^{-1}K^{-1}}$. Co-doping with Al and Ga in combination with nano-structuring approaches, however, have managed to reduce the thermal conductivity down to about 5 $\mathrm{Wm^{-1}K^{-1}}$ reaching a zT of 0.65.[35]

The two binary oxides NiO and ZnO represent two semiconductors of opposite polarity that show a large miscibility gap between them in a quasi binary phase diagram and do not form any intermediate phases. Thus they have been investigated as a promising couple for the realization of coexistent direct junction thermoelectric generators. However, direct junctions between the two materials form a typical charge depletion layer at the interface, leading to diode like behavior and large parasitic resistances.[42] Additionally, their coefficients of thermal expansion differ by a factor of roughly two (13.9^{x}10^{-6} $\mathrm{K^{-1}}$ for NiO and

5-7^{x}10^{-6} K^{-1} for ZnO), which can lead to stress induced cracking of a co-sintered module upon thermal cycling.[92, 93]

3.4 Tungstates

Tungsten oxides have already had an occurrence in the field of thermoelectric oxides earlier, in the form of the n-type tetragonal tungsten bronzes. Here tungsten is forced into a mixed valence state by reduction, making it a semiconducting oxide with moderate Seebeck coefficient. Reduced WO_{3-x} forms crystallographic sheer planes, known as Magnéli phases, exhibiting low thermal conductivity, and reaching zT values of up to 0.3.[94, 95] The material, however, re-oxidizes quickly under ambient atmosphere and returns to the rather rigid tungsten valency of W^{6+}.

The family of metal tungstates (MWO_4) on the other hand relies on the W^{6+} as the rigid backbone of their structure and draw the majority of their properties from the second cation M^{2+}, which the $WO_4{}^{2-}$ anion is paired with. Dependent on the size of the M^{2+} site cation, the system adopts one of two characteristic structures. Large ions like earth-alkaline metals and main-block elements lead to the structure of tetragonal Scheelite, consisting of WO_4 tetrahedra and MO_6 octahedra. The Scheelite type tungstates usually show large band-gaps and little to no electrical conductivity. Their optical properties, however, make them interesting for various applications like scintillators, optical fibers, laser hosts, and sensors. $ZnWO_4$ and $PbWO_4$ for instance are among the best scintillating materials used at *CERN* in the *ALICE* and *CMS* experiments.[97] Paired with a smaller ion, like transition metals, the

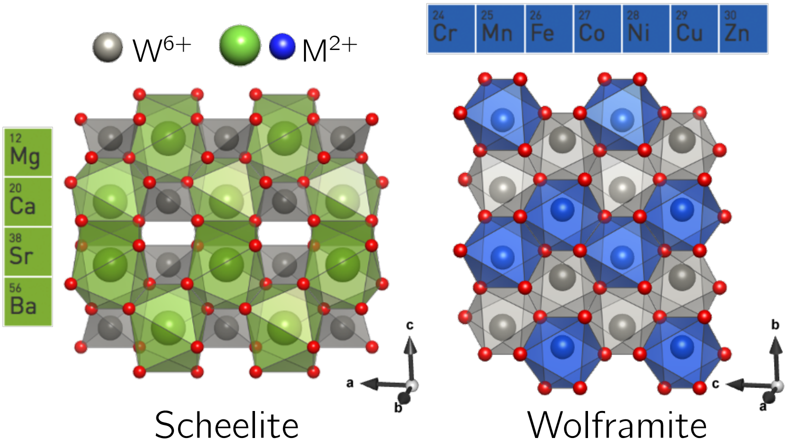

Figure 3.4: Illustration of the crystal structures of earth-alkali metal tungstates with Scheelite strucutre and transition metal tungstates adopting Wolframite structure.[96]

tungstates adapt the crystal structure of the mineral Wolframite, where both WO_6 and MO_6 are in octahedral coordination.

The Wolframite tungstates have gained increasing scientific interest over the past decades due to their stability, easy synthesis, and electronic and magnetic properties. The transition metal tungstates typically show band-gaps in the optical regime, making them promising candidates for photocatalytic water splitting and photo-luminescence applications.[98, 99] They can be grown in various nano-structures like particles, shells, whiskers, and flowers, and show excellent stability in a large pH-regime. Photoelectrochemical water oxidation was successfully demonstrated on e.g. $CuWO_4$, and $NiWO_4$ has been used in heterojunction photoanodes. The interested reader is revered to a detailed review on the photocatalytic properties of the Wolframite tungstates, available under reference [96].

Single valent alkali metal tungstates (M_2WO_4) can not be categorically assigned to a crystal structure. They show a variety of crystal structures,[100–102] may exist in polymorphic forms,[103] and are susceptible to hydration.[104] For higher-valent tungstates it is likewise difficult to describe a general trend for the adapted crystal structures, which is why only a brief overview of notable representatives of this family is given here. Trivalent metal tungstates with tetrahedral WO_4 tend to crystallize in the $Sc_2(WO_4)_3$ structure, which is known for surprisingly high ionic diffusivity of M^{3+} ions due to its layered structure and low electrostatic interaction between O^{2-} and M^{3+}.[105] Small trivalent ions, like Cr^{3+}, Fe^{3+}, and Co^{3+} result in an octahedral WO_6, and ordering of the cation in ratio of 2:1 (M_2WO_6) typically leads to a tripling of the unit cell compared to the divalent tungstates. Co_2WO_6 has proven to be an excellent CO oxidation catalyst.[106] Bi_2WO_6 with an Aurivillius structure has been successfully used as a photoelectrochemical catalyst for the oxidation of organic pollutants.[107] And last, the tetravalent cubic tungstates ZrW_2O_8 and HfW_2O_8 with tetrahedral WO_4 are famous for their constant negative expansion coefficients over large temperature regions, from 0.3 K to over 1000 K.[108]

In the tungstate family especially the transition metal tungstates with Wolframite structure have been extensively, and systematically studied, as they provide the opportunity to combine transition metal oxide semiconducting properties with the structural stability of the tungstates. Semiconducting transition metal binary oxides, like NiO and ZnO, have proven quite successful candidates for high temperature thermoelectrics but other candidates are discarded as they show limited stability and phase transitions at higher temperatures. Here their respective tungstates could prove as promising alternatives.

3.5 Iron tungstates

In the following the two tungstates most relevant to the thesis are reviewed in further detail, namely Fe_2WO_6 and $FeWO_4$, where details of their structure, transport properties, and defect landscape are presented.

3.5.1 Fe_2WO_6

Crystal structure

Despite its stability, the trivalent iron tungstate does not occur as natural mineral. It is part of the trivalent tungstates mentioned in the earlier section and has been reported to crystallize in three different polymorphic modifications, dependent on the synthesis conditions.[109] The α-Fe_2WO_6 polymorph, with an orthorhombic Columbite structure is formed under synthesis conditions below 800 °C. The high temperature γ-Fe_2WO_6 phase forms at temperatures above 900 °C, with the typical tri-α-PbO_2 structure. In between, with rather ill-defined phase boundaries, the monoclinically distorted β-Fe_2WO_6 forms. Experimentally the tri-α-PbO_2 is found to be the most stable one and once formed, a conversion to the other polymorphs seems kinetically hindered. The structure is an ordered variant of the α-PbO_2 structure, in which half of the octahedral voids are filled with metal ions in a distorted hexagonal close packing of oxygen atoms. The 2:1 cation ratio causes a tripling

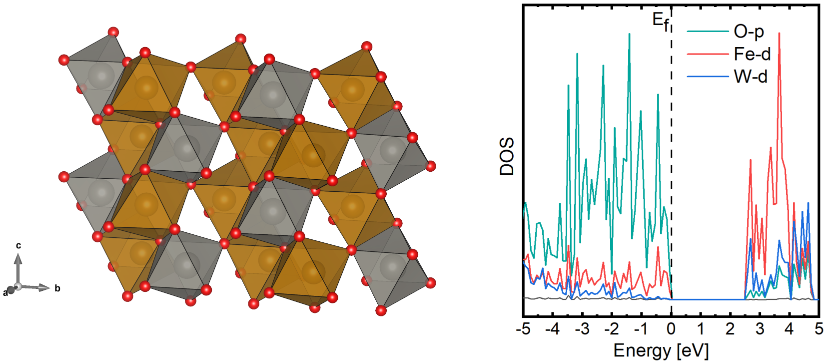

Figure 3.5: Crystal structure and projected density of states of Fe_2WO_6

of the b-axis (in the Columbite variant the a-axis is tripled), hence tri-α-PbO_2. This results in zig-zag chains of skew-edge sharing MO_6 octahedra along the c-axis, where one third of the chains contain only FeO_6, and two thirds contain alternating FeO_6 and WO_6 octahedra. It belongs to the crystallographic space group $Pbcn$ with cell parameters of $a = 4.578$ Å, $b = 16.757$ Å, and $c = 4.968$ Å.

Fe_2WO_6 shows an anti-ferromagnetic ordering of the magnetic Fe^{3+} moments, with a Néel temperature of $T_N \approx 240$ K.[110] There is some disagreement in the literature about the ground state of the magnetic order, although the $\uparrow\uparrow\downarrow\downarrow\downarrow\downarrow\uparrow\uparrow$ ordering, in the magnetic space group $Pbc'n'$ seems to have prevailed.[111, 112]

Transport properties

Fe_2WO_6 is an n-type semiconductor, with thermally activated polaron hopping conduction. The valence band is comprised of O-2p bands and the conduction band mainly of the empty Fe-3d sub-band. Reports on the optical and thermal band gap differ greatly, ranging from 1.5 eV to 2.45 eV.[113–115] The charge carriers are electrons localized on Fe sites with a mobility in the order of $\sim 10^{-3}\mathrm{cm^2V^{-1}s^{-1}}$ at room temperature. The mobility is thermally activated with an activation energy of 0.33-0.35 eV and corresponds to electron hopping along the skew edge sharing Fe octahedra in c direction.

Defect chemistry

The appearance of localized charge carriers as electronic defects, must be accompanied by the occurrence of point defects of opposite charge in order to guarantee charge neutrality. We will in the following discuss the arise of $\mathrm{Fe'}$ species in $\mathrm{Fe_2WO_6}$ and discuss possible defects and their reactions, whereby we will make use of the Kröger-Vink notation.[116] We will first treat internal disorder, on the example of site-exchange defects. Cation-anion exchanges are less likely than cation-cation defects due to the electrostatic forces and the size differences. We therefore assume the following defect reaction

$$\mathrm{Fe_{Fe}}^{\mathrm{X}} + \mathrm{W_W}^{\mathrm{X}} \rightleftharpoons \mathrm{Fe_W}^{3\prime} + \mathrm{W_{Fe}}^{3\bullet} \tag{3.1}$$

In the limit of small defect concentrations and non-interacting defects, the according mass action law is

$$K_S = \frac{[\mathrm{Fe_W}^{3\prime}][\mathrm{W_{Fe}}^{3\bullet}]}{[\mathrm{Fe_{Fe}}^{\mathrm{X}}][\mathrm{W_W}^{\mathrm{X}}]} \tag{3.2}$$

In this reaction no free charge carriers are generated (Fe_2WO_6 shows no ionic conductivity), so these site exchange defects represent merely a defect background. An increase in the concentration of these defects is to be expected at high temperatures from a thermodynamic point of view, which, however, should not have have any major influence on the conductivity. Although an interruption of the ordered zigzag chain structure through site exchange defects can affect the conductivity in theory, the ability of intra-chain conduction in Fe_2WO_6 has been pointed out in literature.[117] The occurrence of free charge carriers must therefore be rooted in external influences such as non-stoichiometry or reactions. An imbalance between the cations, with W in excess and Fe in deficit, leads to an effective donor doping of the material. The resulting negative charge carriers are not free but we assume that they are localized as polarons on Fe sites.

$$3\,[\mathrm{W_{Fe}}^{3\bullet}] = [\mathrm{Fe_{Fe}}'] \tag{3.3}$$

This inherent doping is rigid and remains constant with changing oxygen partial pressure and temperature. A change in charge carrier concentration must therefore be based on defect equilibria. The most natural example for this would be the assumption of intrinsic charge carrier generation, through the excitation of electrons from the valence into the conduction band; or to stay in the frame of localized states: A charge transfer from O to Fe.

$$\mathrm{O_O}^{\mathrm{X}} + \mathrm{Fe_{Fe}}^{\mathrm{X}} \rightleftharpoons \mathrm{O_O}^{\bullet} + \mathrm{Fe_{Fe}}' \tag{3.4}$$

The mass action law of the intrinsic ionization when expressed as site fractions then reads

$$K_i = \frac{[\mathrm{O_O}^{\bullet}][\mathrm{Fe_{Fe}}']}{[\mathrm{O_O}^{\mathrm{X}}][\mathrm{Fe_{Fe}}^{\mathrm{X}}]} \tag{3.5}$$

When relating the equilibrium constant to the Gibbs free energy one can find an expression for the charge carrier density.[†]

$$\sqrt{[\mathrm{O_O}^{\bullet}][\mathrm{Fe_{Fe}}']} = \sqrt{[\mathrm{O_O}^{\mathrm{X}}][\mathrm{Fe_{Fe}}^{\mathrm{X}}]}\exp\left(\frac{-\Delta G}{2k_B T}\right) \tag{3.6}$$

Note that the expression is essentially the same as Equation 2.1.3 and the Gibbs free energy corresponds to the band gap. Accordingly, the band gap can be obtained from an Arrhenius plot.

Alternatively, an oxygen exchange reaction, for n-type conductors typically a reduction creating oxygen vacancies, can be considered for a charge carrier generation.

$$\mathrm{O_O}^{\mathrm{X}} + 2\,\mathrm{Fe_{Fe}}^{\mathrm{X}} \rightleftharpoons \mathrm{v_O}^{\bullet\bullet} + 2\mathrm{Fe_{Fe}}' + \frac{1}{2}\mathrm{O_2} \tag{3.7}$$

With the corresponding equilibrium constant

$$K_{\mathrm{v_O}^{\bullet\bullet}} = \frac{[\mathrm{v_O}^{\bullet\bullet}][\mathrm{Fe_{Fe}}']^2 {p_{\mathrm{O_2}}}^{1/2}}{[\mathrm{O_O}^{\mathrm{X}}][\mathrm{Fe_{Fe}}^{\mathrm{X}}]^2 {p^0_{\mathrm{O_2}}}^{1/2}} \tag{3.8}$$

With a number of possible relevant defects now identified, we can find their concentrations as a function of $p_{\mathrm{O_2}}$ and construct a Brouwer dia-

---

[†] In an intrinsic semiconductor the number of electrons and holes is equal therefore the intrinsic charge carrier concentration can be expressed as $n_i = \sqrt{np}$. The full localization of charge carriers, whereby the density of states effectively corresponds to the atomic site density, is somewhat over-simplified, but is retained for reasons of continuity of the localized defect picture.

gram. I am here getting a bit ahead and use the findings of **Publication I** that Fe_2WO_6 does indeed develop oxygen vacancies at high temperatures, the activation energy of the conductivity is too small to infer an intrinsic charge carrier excitation, and the material has a constant charge carrier concentration below a threshold temperature, which suggests a background doping, as shown here by the example of non-stoichiometry or a frozen-in oxygen exchange reaction.

$$[\mathrm{Fe_{Fe}}'] = 2[\mathrm{v_O}^{\bullet\bullet}] + 3[\mathrm{W_{Fe}}^{3\bullet}] + [\mathrm{O_O}^{\bullet}] \tag{3.9}$$

By applying the Brouwer approximations, simplified analytical expressions can be found for the mass action laws in Equations 3.3, 3.5, and 3.8. The approximations for the predominant main defects are given in Figure 3.6 above the relevant regions. Experimentally only the very left part of the Brouwer diagram can be observed, and the emerge of metal vacancies at very high p_{O_2} is added for completeness, but remains speculative. The temperature dependence of the defect species can now be found by relating the equilibrium constants 3.3, 3.5, and 3.8 to the Gibbs free energy, as already exemplary shown for the intrinsic ionization in Equation 3.6.

$$K = \exp\left(\frac{-\Delta G^{\ominus}}{k_B T}\right) = \exp\left(\frac{\Delta S^{\ominus}}{k_B}\right)\exp\left(\frac{-\Delta H^{\ominus}}{k_B T}\right) \tag{3.10}$$

The same Brouwer approximations can be used to simplify the expressions and plot the concentrations against inverse temperature at ambient p_{O_2}, as shown in Figure 3.6 on the right panel. Experimentally, the intrinsic ionization dominated region is not reached up to 950 °C, but is

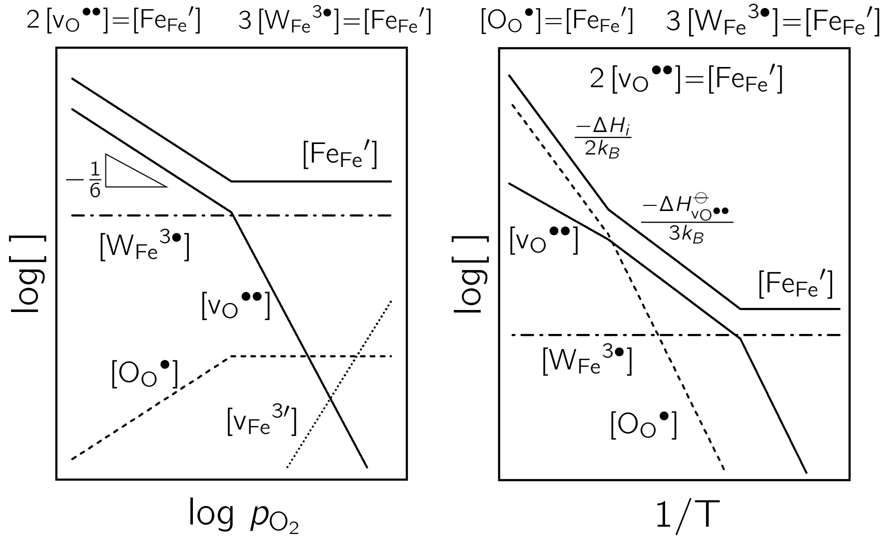

Figure 3.6: Left: Proposed Brouwer diagram for Fe_2WO_6 dominated by oxygen vacancies (low p_{O_2}) and donor dopants due to non-stoichiometry. Speculative Fe vacancies emerge as compensating defects at very high p_{O_2}. Right: Proposed temperature dependence of defect concentrations for Fe_2WO_6 with intrinsic, oxygen deficient and extrinsic dominated regions. In the intrinsic region the two lines for $O_O{}^{\bullet}$ and $Fe_{Fe}{}'$ should lie on top of each other, but are depicted with a little distance for clarity. A dominance of frozen-in of oxygen vacancies at low temperatures instead of non-stoichiometry is likewise conceivable.

included for completeness. At intermediate temperatures charge carriers emerge mainly from the oxygen exchange reaction and becomes constant below a certain temperature. In the presented example, to complete the defect model, intrinsic dopants from non-stoichiometry are shown as the cause for the constant charge carrier concentration at low temperatures, as suggested by some authors in literature.[118] As explained in detail in **Publication I**, however, we do not find any indications of Fe under-stoichiometry, which suggests that the oxygen vacancies remain the charge balancing species, but the oxygen exchange reaction below the threshold temperature comes to a standstill, freezing-in the oxygen vacancy concentration.

3.5.2 $FeWO_4$

Structure

$FeWO_4$ is known as the natural mineral Ferberite and the end member of the original Wolframite solid solution $(Fe, Mn)WO_4$. It crystallizes in the monoclinic pace group $P2/c$ with cell parameters $a = 4.729$ Å, $b = 5.707$ Å, $c = 4.962$ Å, and $\beta = 90.04°$. Like Fe_2WO_6, the structure consists of edge sharing MO_6 octahedra along the c direction, however, the 1:1 cation ordering leads to parallel chains, which are fully occupied by either Fe or W.

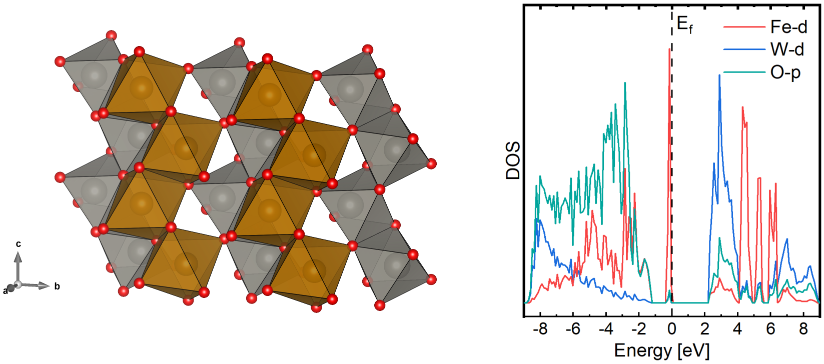

Figure 3.7: Crystal structure and projected density of states of Wolframite type $FeWO_4$

The magnetic structure consists of ferromagnetic [100] planes, antiferromagnetically stacked along the a-axis, with the moments tilted in a 29° against the a-axis. The antiferromagnetic $FeWO_4$ has a Néel temperature of $T_N \approx 66$ K.[119]

Transport

$FeWO_4$ is a p-type semiconductor with a band gap of ca. 2.00 eV.[120–122] The valence band is composed of a Fe-3d band disconnected from the lower lying O-2p bands. The conduction band is made up of empty W-5d bands. Electronic conduction between room temperature and 1200 K is typical small polaron hopping with an activation energy of 0.16-0.21 eV,[123, 124] which is close to the theoretically predicted minimum migration energy of 0.14 eV.[120] Higher activation energies are connected to site defects which interrupt the chains, caused by impurities of other divalent ions like Mn. Electron holes are considered to be localized on Fe sites and hop along the Fe chains in c-direction. The hole drift mobility is in the range of $\sim 10^{-2}$ $cm^2V^{-1}s^{-1}$.

Defect chemistry

The defect chemistry of $FeWO_4$ mostly relies to purely theoretical studies, since experimental studies are difficult, owed to the limited stability towards oxygen at high temperatures. From these theoretical studies, it turns out, that the most energetically favorable defects are Fe vacancies and localized holes on Fe sites.[120] Their formation mechanism remains speculative at the moment. An oxygen exchange reaction, which oxidizes the material is conceivable, as this analogous mechanism has already been demonstrated in several other p-type transition metal oxides, like NiO, CoO, MnO, and FeO.

$$3\mathrm{Fe_{Fe}}^{X} + \frac{1}{2}\mathrm{O_2} \leftrightharpoons \mathrm{v}''_{\mathrm{Fe}} + 2\mathrm{Fe}^{\bullet}_{\mathrm{Fe}} + \mathrm{FeO} \tag{3.11}$$

Several reports agree that the metal cations leaving the structure find space on interstitial sites and form clusters with the vacancy that has been left behind.[125–127] The crystal structures of the binary oxides and the tungstate are not the same, but the tungstate structure also offers enough space for octahedral interstitials, since the octahedral gaps of the oxygen sub-lattice are only half occupied. It should be noted, however, that the tungstate is a tertiary phase, which, without the simultaneous formation of tungsten vacancies, should lead to the precipitation of a binary iron oxide. Schmidbauer *et al.* report a significant difference in conductivity for $\mathrm{FeWO_4}$ samples annealed in very low versus medium $p_{\mathrm{O_2}}$, in line with the assumed defect reaction, where more available oxygen leads to an increase in charge carrier concentration.[124] A constant charge carrier concentration can thus be expected to arise either from a freeze-in of metal vacancies due to the standstill of the oxygen exchange reaction, or a fixed acceptor dopant concentration. This can possibly be reflected in a cation non-stoichiometry, in which an over stoichiometry on Fe acts as an inherent acceptor dopant.

$$4[\mathrm{Fe}^{4\prime}_{\mathrm{W}}] = [\mathrm{Fe}^{\bullet}_{\mathrm{Fe}}] \tag{3.12}$$

Theoretically, however, these defects are predicted to be extremely energetically unfavorable. Intrinsic ionization in $\mathrm{FeWO_4}$ at higher temperatures corresponds to a charge transfer from Fe to W.

$$\mathrm{Fe_{Fe}}^{\mathrm{X}} + \mathrm{W_W}^{\mathrm{X}} \leftrightharpoons \mathrm{Fe_{Fe}}^{\bullet} + \mathrm{W_W}' \tag{3.13}$$

I will here again get a bit ahead and make use of the results presented in **Publication II**, where we find a constant charge carrier concentration below 500 °C, and an increase in charge carriers at higher temperatures, which is too shallow to correspond to intrinsic ionization and is thus ascribed to the defect chemical reaction presented above, with a formation enthalpy of ca. 1 eV.

3.5.3 Phase relations in the Fe-W-O system

There exist only few studies on the phase relations between the two tungstates. Fe_2WO_6 and $FeWO_4$ are the only ternary compounds occurring in the Fe-W-O system.[128] $FeWO_4$ is fully miscible with the isostructural and isoelectric $MnWO_4$, even at temperatures as low as 160 °C.[129] The most sensitive lattice parameter to the Mn content in the solid solution $Mn_{1-x}Fe_xWO_4$ is the a-axis, changing by more than 0.1 Å over the range $0 \leq x \leq 1$.[130] On the other hand $FeWO_4$ has been shown to be coexistent with Fe_2WO_6 and other trivalent oxides, like Fe_2O_3.[129, 131] In reaction and miscibility experiments the lattice constants do not show any comparably large changes, despite the significantly larger radius difference between Mn^{2+} (0.97 Å) and Fe^{3+} (0.785 Å), compared to Mn^{2+} and Fe^{2+} (0.92 Å).[132] It can therefore be expected that the two phases $FeWO_4$ and Fe_2WO_6 are separated by a large miscibility gap in a quasi-binary phase diagram.

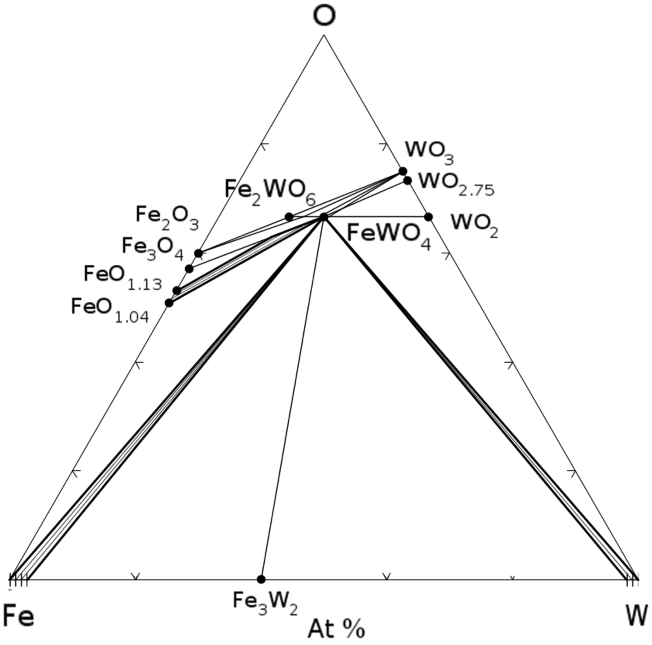

Figure 3.8: Isothermal ternary phase diagram at 900 °C of the Fe-W-O system.[128]

4 Methods

The following chapter will give an overview on experimental methods used in this thesis and a brief introduction of the theory underlying the measurements.

4.1 Synthesis

The preparation of polycrystalline solid samples in this work was done via the solid state reaction route. The trivalent iron tungstate Fe_2WO_6 was obtained via this route, reacting Fe_2O_3 and WO_3 precursors at 950 °C for a total of 36 hours in air, with 2 intermediate grinding and subsequent uniaxial pressing steps.

$$Fe_2O_3 + WO_3 \longrightarrow Fe_2WO_6 \tag{4.1}$$

In order to keep the possibility of cross contamination as low as possible, each reaction was carried out in a specially provided crucible with a cover.

Air sensitive compositions can be obtained by the evacuated quarz ampule method, where the mixed precursors are transferred into a quarz tube which is sealed off under dynamic vacuum using a hydrogen torch.

Using this route, no decomposing precursors can be used, as the expanding decomposition gases will explode the ampule. $FeWO_4$ can be obtained by this method with two different precursor routes.

$$\begin{aligned} FeO + WO_3 &\longrightarrow FeWO_4 \\ \frac{1}{3}Fe_2O_3 + \frac{1}{3}Fe + WO_3 &\longrightarrow 2FeWO_4 \end{aligned} \tag{4.2}$$

$FeWO_4$ could be obtained on both routs, however the second one proved more successful with less steps necessary and less secondary phase problems, probably due to the fact that FeO itself is known to be a cation deficient non-stoichiometric compound which is better described by $Fe_{1-x}O$, also known as the mineral Wüstite. Satisfactory single phase products was usually obtained after a total reaction time of 36 hours with two intermediate grinding steps and re-sealing.

Precipitation methods are in principle an alternative, and usually preferred route to synthesize transition metal tungstates, however the iron-tungstates proved problematic in this respect. Here usually a solution of Na_2WO_4 is added to a transition metal nitrate precursor solution. The non-soluble transition metal tungsates will precipitate, while the sodium and nitrate stay dissolved and the product can be filtrated. The precipitate from an Fe(III) precursor and Na_2WO_4 will yield the metastable garnet $Fe_2(WO_4)_3$, which will then decompose to Fe_2WO_6 and WO_3 in the following calcination step. A stable Fe(II) precursor, e.g. $(NH_4)_2Fe(SO_4)_2(H_2O)_6$ precipitates $FeWO_4$, the following calcination step, however has to be done under continuous flow of inert gas to prevent re-oxidation to Fe(III). Precursors containing nitrates contain the additional uncertainty of crystal water, as they tend to hydrate to different degrees, and need to be either fully hydrated or fully dried, prior to the stoichiometric weighing, in order to not falsify their molecular weight.

Sintered pellets were produced from the finely ground powders by uniaxial pressing in a cylindrical die of 13 mm diameter with 2-3 tons of pressure, followed by a thermal treatment of at 1000-1150 °C for 4-20 hours. The pellets reached densities of 80-90% relative density.

4.2 X-ray diffraction

X-ray diffraction is the most widely used technique to characterize solid crystalline materials. It is based on the principles of Bragg's law, which describes the occurrence of constructive and destructive interference of x-rays when diffracted on a three dimensional grating.

$$n\lambda = 2d_{hkl}\sin\Theta \tag{4.3}$$

Here λ is the incident x-ray wavelength, d_{hkl} denotes the lattice plane distance for a given lattice plane with Miller indices $[hkl]$, Θ is the incident beam angle, and n is an integer. By scanning Θ and observing the diffracted x-ray intensity, a peak is produced at angles where the Bragg condition is met. Where this diffraction pattern consists of distinct points for single crystals, the random crystal orientation of powder samples gives a pattern of concentric rings.

The interplanar distance d_{hkl} is a function of the lattice parameters a,b, and c and angles α, β, and γ from which the lattice system can be determined of which 7 different exist: Cubic, Tetragonal, Orthorhombic, Hexagonal, Monoclinic, and Triclinic; with Cubic being the most symmetric to Triclinic least symmetric. The Triclinic expression is generally valid for all systems.

$$\frac{1}{d^2} = \frac{\begin{pmatrix} b^2c^2\sin^2\alpha h^2 + a^2c^2\sin^2\beta k^2 + a^2b^2\sin^2\gamma l^2 \\ \hfill +2abc^2(\cos\alpha\cos\beta - \cos\gamma)hk \\ \hfill +2a^2bc(\cos\beta\cos\gamma - \cos\alpha)kl \\ \hfill +2ab^2c(\cos\gamma\cos\alpha - \cos\beta)hl \end{pmatrix}}{\left(abc\sqrt{1-\cos^2\alpha-\cos^2\beta-\cos^2\gamma+2\cos\alpha\cos\beta\cos\gamma}\right)^2} \tag{4.4}$$

The expression takes much simpler forms for systems with 90° angles and equidistant lattice parameters (higher symmetries). The lattice systems are subdivided into 14 Bravais lattice and 32 crystallographic point groups, resulting in a total of 230 space groups to describe all possible crystal symmetries, all of which are described in detail in the international tables for crystallography.[133] The intensity of each reflection is a function of structure factor F, Lorenz polarization LP, absorption $A(\Theta)$, and temperature factors u.

$$I = |F(hkl)^2| LPA(\Theta)u \tag{4.5}$$

The biggest contribution to intensity is the structure factor F, which is the sum of all atomic form factors f_j in the unit cell for each hkl, given by the structure factor equation.

$$F(hkl) = \sum_j f_j exp[2\pi i(hx_j + ky_j + lz_j)] \tag{4.6}$$

The atomic form factors f_j are only dependent on the number of electrons in the atom and the incident beam angle. Thus lattice planes at low angles containing more heavy atoms give larger intensity peaks. The representations given are somewhat simplified and do not include the phase angle, which would go beyond the scope of this short introduction.

4.2.1 Data acquisition

In this work several different x-ray diffraction techniques were used. The standard measurements for all powder samples was done on a Bruker D8 Discover with Cu Kα1 radiation, Ge (111) Johanssen monochromator and a Lynxeye detector in Bragg-Brentano-geometry. Flatbed low background glass sample holders were used, where a fine dispersion of sample powder in ethanol was applied.

High temperature x-ray diffraction was perfomed on a Bruker D8 A25 with a focusing Goebel mirror and LynxEye XE detector. Measurements were carried out in a Anton Paar HTK1200 oven chamber using Mo x-ray source without monochromator. For air sensitive samples the chamber was continuously flooded with a 10 $\mathrm{ml\,s^{-1}}$ flow of Ar.

Besides in-house XRD, also synchrotron radiation diffraction experiments at BM31 (SNBL) at ESRF (France) were carried out on selected samples. The diffraction principles are the same but the incident x-rays are generated from bending accelerated electrons, which gives a highly monochromatic x-ray beam with much larger intensity compared to laboratory x-ray sources. In this case 0.5 mm capillary samples were irradiated with x-rays of $\lambda = 0.4943$ Å wavelength and a Dexela 2923 CMOS two-dimensional detector was used. The 2D detector allows to obtain the whole diffraction pattern in "one-shot", corresponding to ca. 2 seconds of acquisition time, compared to the 30-90 minutes for a laboratory x-ray diffraction experiment.

4.2.2 Rietveld Refinement

Where single crystal diffraction data contains information on atomic positions, their occupancy and their temperature factors, this information is "masked" in powder patterns by the overlapping of the peaks and not easily accessible. The Rietveld method however allows to extract some of that information by building a model structure and comparing it to the experimental pattern. The more accurate the model, the more reliable are the obtained values, however, high quality diffraction data is necessary to make the extracted parameters meaningful. The model structures diffraction pattern is simulated according to Equation 4.4, and Equation 4.5, along with background and peak shape terms, and its parameters are refined until it best matches the experimental data. The method minimizes the function M with weighing factor W_i and scaling factor c by a least squares algorithm.

$$M = \sum_i W_i \left(I_i^{obs} - \frac{1}{c} I_i^{calc} \right)^2 \tag{4.7}$$

The refinement is usually assessed on the weighted profile residual R_{wp}.

$$R_{wp} = \sum_{i}^{n} \sqrt{\frac{W_i(I_i^{obs} - I_i^{calc})^2}{\sum_i^n W_i(I_i^{obs})^2}} x100\% \tag{4.8}$$

There exist several additional validation figures like R_p, R_B, R_{exp}, and X^2, however, there is no defined threshold that indicates a good fit, which is why the visual inspection of high 2Θ reflections is often used to evaluate the fit.

4.3 Conductivity and Seebeck coefficient

Conductivity and Seebeck coefficient measurements were carried out on sintered pellets in a custom built assembly mounted setup in a ProboStat cell from NORECS AS. The setup consists of a long sample holder rod, which can be inserted into the hot zone of a tube furnace. The sample, electrodes and thermocouples are held in place by spring loaded alumina rods. The setup is encapsulated by a fused silica tube, to differentiate it from ambient atmosphere. A connected gas mixing station with three oxygen-argon dilution stages allows to control the partial pressure of oxygen to which the sample is exposed to over several orders of magnitude. Conductivity of individual materials was measured by the van der Pauw method, for which four thin electrode wires of platinum were pressed on the sample near the outer edges. The measurements included reversed polarity measurements to compensate for the Seebeck effect.

For Seebeck coefficient measurements two Pt-Pt10Rh thermocouples (S-type) made from 0.2 mm wires are pressed in a line on top of the

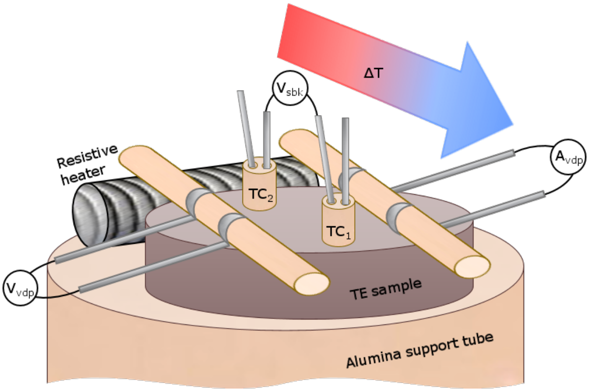

Figure 4.1: Schematic illustration of a probostat thermoelectric measurement setup, depicting the top piece of the support finger, accommodating the sample, 4-point electric contacts, in-plane heater, and thermocouples. The setup is described in detail under reference [134].

sample. The thermocouples function as both temperature sensors and voltage probes. This way, the thermovoltage is measured as close to the actual temperature as possible. A small resistive heater next to the sample is gradually ramped up to produce an in-plane thermal gradient, while the voltage between the thermocouples is monitored, producing ΔV vs. ΔT plots, from which slope the Seebeck coefficient can be extracted. The measured voltage is automatically corrected for the additional Seebeck voltage generated by the Pt-wires under the locally applied thermal gradient by the data acquisition program.

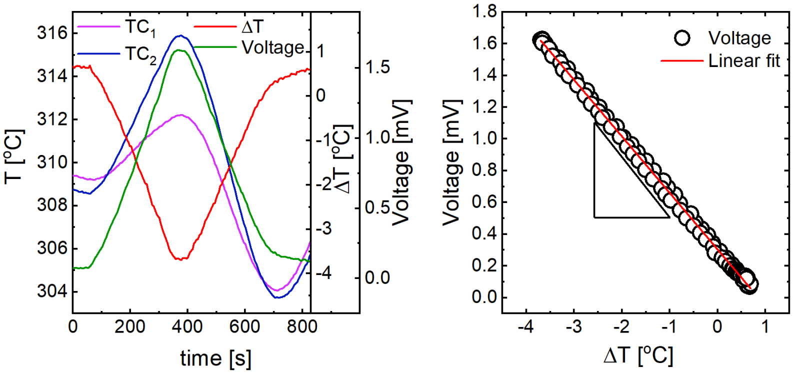

Figure 4.2: Raw data of a Seebeck coefficient measurement at 300 °C depicting the temperature course of the two thermocouples, their ΔT and the resulting thermovoltage between them. Plotting voltage vs. ΔT allows to directly obtain the Seebeck coefficient from the slope.

4.4 Thermal conductivity

Thermal conductivity was measured by the laser flash analysis (LFA) method, where the thermal diffusivity α is measured and thermal conductivity κ obtained from sample density ρ and specific heat capacity C_p.

$$\kappa = \alpha \rho C_p \tag{4.9}$$

A laser pulse is fired on one side of a disc shaped sample of thickness d, and the temperature on the counter side is monitored with an infrared sensor. The thermal diffusivity is related to the time it takes to heat the sample to half of its maximum value $\tau_{1/2}$.

$$\alpha \cong \ln\left(\frac{1}{4}\right) \frac{d^2}{\pi^2 \tau_{1/2}} \tag{4.10}$$

LFA was conducted on a Netzsch LFA 457 microFlash™ under nitrogen atmosphere on graphite coated pellets. The heat capacity was estimated by comparing the maximum temperature difference of the sample to a Pyroceram 9606 standard reference sample from Netzsch, and a Cape-Lahmann pule correction model.[135]

4.5 Optical absorption

Electronic transitions are typically in the energy range of ultraviolet to visible light (UV-Vis) and contain information on the energy difference between the highest occupied- (HOMO) to the lowest unoccupied molecular state (LUMO). In a semiconductor these states correspond to the respective band edges of the valence band and the conduction band. Optical absorption spectroscopy can thus be applied to probe the band gap (E_g) of a semiconducting material. This is done by construction of Tauc plots, relating the absorption coefficient (α) to the incident light energy ($h\nu$).

$$(\alpha h\nu)^n = C(h\nu - E_g) \tag{4.11}$$

Here C is a proportionality constant, ν is the frequency of the incident light, and the exponent n is characteristic for the nature of the transition, taking values of 2 for direct allowed, 2/3 for direct forbidden, 1/2 for indirect allowed, and 1/3 for indirect forbidden transitions.[136, 137] Plotting $(\alpha h\nu)^n$ vs. $h\nu$ and extrapolating the linear portion to the baseline, allows to extract the band gap E_g. For some solids, this method proves problematic, as the absorption coefficient is not easily accessible. The theory of Kubelka and Munk however, allows to use diffuse reflectance spectroscopy, by relating the absorption coefficient directly to the remission R_∞ in the Kubelka-Munk function.[138]

$$\alpha \propto F(R_\infty) = \frac{(1 - R_\infty)^2}{2R_\infty} \tag{4.12}$$

Consequently, the band gap can be extrapolated from an analogous Kubelka-Munk plot, showing $[F(R_\infty)h\nu]^n$ vs. $h\nu$. Optical reflectance spectroscopy experiments in conjunction with this thesis were carried out with a USB2000+ *OceanOptics* spectrometer, and a halogen lamp light source. A flat $BaSO_4$ sample was used as white reference.

4.6 X-ray photoelectron spectroscopy (XPS)

Photoelectron spectroscopy is a technique for chemical analysis of a materials surface. Irradiating a material with photons and measuring the kinetic energy of the electrons emitted from the sample by the photoelectric effect, gives insight in the elemental composition, chemical environment, and electronic states of the elements within the sample. The ejected electrons kinetic energy depends on the incident photon energy $E_{h\nu}$, and the binding energy of the electron E_B.

$$E_{kin} = E_{h\nu} - E_B \tag{4.13}$$

The binding energy is characteristic for the element, chemical environment, and the orbital from which it is emitted. Detected electrons consist of the primary electrons, which are not scattered and contain the information on discrete core level binding energies, and the secondary

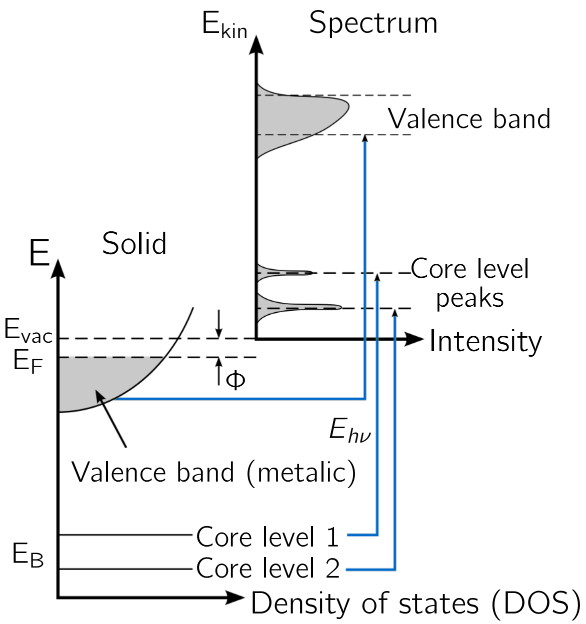

Figure 4.3: Schematic illustration of the photoelectron emission process from a solid surface and the resulting spectrum.

electrons, which are inelastically scattered and give rise to a continuous background in the spectrum. The secondary electron cut-off can be used to obtain a materials work function Φ. The primary electron onset contains additional information on the density of states near the Fermi level. Quantitative information on the elements can be obtained from the core level peaks, when fitted properly. For background subtraction standard correction algorithms are available: Linear, Shirley, and Tougaard. A simple linear background is sufficient for highly ionic materials. The Shirley method uses spectral information to model a background sensitive to alterations in the data, and the Tougaard algorithm tries to estimate the probability of a scattering event based on the energy loss cross section at a certain energy offset.[139, 140] Likewise there exist a number of line shapes to model the core peaks in a spectrum. Symmetric peaks can by default be fitted with Gaussian-Lorentzian line shapes, however, the chemical environment of an atom, like vibrational anisotropy, can make it necessary to use asymmetric Doniachi-Sunjic peak shapes for the fit.[141] In this work XPS experiments were performed on a ThermoFisher Scientific Thetaprobe, with calibrated energy scale to the Ag-3d$_{\frac{5}{2}}$ peak of 368.21 eV binding energy with the stage polarized to -16 V during the experiments. As XPS is only surface sensitive, the experiments were perfomred on freshly fractured surfaces of sintered pellets. Quantitative results were obtained from Shirley background corrected spectra, fitted with Voigt shapes (GL(50)) for symmetric peaks, and asymmetric Lorenzian shapes (LA(α,β,w)).

5 Publications

In this chapter the publications included in this thesis are presented and a summarizing overview on the main findings is provided.

Included publications and manuscripts

- **Paper I**:
  Defects and polaronic electron transport in Fe_2WO_6, Raphael Schuler, Truls Norby, and Helmer Fjellvåg, Physical Chemistry Chemical Physics, **2020**, 22, 15541-15548

- **Paper II**:
  Near-broken gap alignment between $FeWO_4$ and Fe_2WO_6 for ohmic p-n junction thermoelectrics, Raphael Schuler, Federico Bianchini, Truls Norby, and Helmer Fjellvåg (*Submitted to ACS Applied Materials & Interfaces*)

- **Paper III**:
  Versatile 4-leg thermoelectric module test setup adapted to a commercial sample holder system for high temperatures and controlled atmospheres, Raphael Schuler, Reshma K. Madathil, and Truls Norby (*Submitted to Journal of Scientific Instruments*)

Co-authored publications and manuscripts, not included

- Time-enhanced performance of oxide thermoelectric generator based on hybrid p-n junction, Nikola Kanas, Rasmus Bjørk, Kristin Wells, Raphael Schuler, Mari-Ann Einarsrud, Nini Pryds, Kjell Wiik, ACS Omega, **2021**, 6, 1, 197-205
- Fabrication of a silicide thermoelectric module employing fractional factorial design principles, Joachim Seland Graff, Raphael Schuler, Xin Song, Gustavo Castillo-Hernandez, Gunstein Skomedal, Erik Enebakk, Daniel Nilsen Wright, Marit Stange, Johannes de Boor, Ole Martin Løvvik, Matthias Schrade (*Submitted to Journal of Electronic Materials*)

Summarizing overview of publications I-III

In **Publication I** we investigate the conduction mechanism and the origin of charge carriers in the n-type Fe_2WO_6, with a combination of high quality synchrotron x-ray diffraction, x-ray photoelectron spectroscopy, p_{O_2}-dependence, conductivity, thermogravimetry, and Seebeck coefficient measurements. Based on the results we establish a defect chemical model, identifying oxygen vacancies on the O3 site as inherent donors present in Fe_2WO_6. The formation of oxygen vacancies and two electrons has a standard formation enthalpy of 113(5) $\mathrm{kJmol^{-1}}$ and a standard formation entropy of 41(5) $\mathrm{Jmol^{-1}K^{-1}}$. We identify charge carriers in Fe_2WO_6 to be trapped electrons on Fe sites and conducting via an adiabatic small polaron hopping mechanism along the zigzag chains of FeO_6 octahedra. Below 650 °C we find a constant charge carrier concentration as a result of the freeze-in of oxygen vacancies as the exchange reaction comes to a standstill. This allowed to decouple the carrier mobility from the overall conductivity and parameterize the polaron mobility, where we find an activation energy of 0.34(1) eV and a pre-exponential $u_0 = 400(50)$ cm^{2}KV^{-1}s^{-1}. Laser flash analysis determined a thermal conductivity of 1.5-2.5 Wm^{-1}K^{-1}, which, to our knowledge, is reported for the first time. From the measured electrical conductivity, Seebek coefficient, and thermal conductivity we calculate the thermoelectric figure of merit $zT = 0.027$ at 900 °C.

The p-n junction between the p-type $FeWO_4$ and n-type Fe_2WO_6 as candidates for the realization of a direct junction thermoelectric generator with omitted interconnect was investigated as part of **Publication II**. The p-n junction exhibits non-rectifying behavior in a large temperature and bias range. We determine electron affinities for both materials by x-ray photoelectron spectroscopy, and combine the affinities with band gap measurements from UV-VIS reflectance spectroscopy to construct a band alignment diagram. The band alignment indicates a near-broken gap junction, but with a small enough offset of 0.16 eV to be bridged by tail states above the p-type valence band. Further we carried out density functional theory calculations on the individual bulk materials to get a better understanding of the crucial band edges involved. We find a highly localized Fe-3d band at the valence band of the p-type $FeWO_4$ and a Fe-3d dominated conduction band edge in Fe_2WO_6, which are the two aligning bands in the suggested broken gap junction. This suggests that the similarity of the character of the involved bands plays an essential role in their energy proximity and overlap.

For the characterization and testing of pilot thermoelectric modules we designed and constructed a test setup, which is reported in **Publication III** The setup is adapted to the NORECS AS ProboStat™sample holder cell and enables the characterization of thermoelectric modules with up to four legs at high temperatures, under large temperature gradients, and in various atmospheres. The setup utilizes a water cooled stainless steel support tube, on which four 5×5 mm^2 TE-legs with no height restriction can be mounted via springload, and inserted into a tube furnace hot zone. Thermocouples, electrodes, gas supply, and outer enclosing tube use standard ProboStat™ feedthroughs and dimensions. The thermoelectric module is surrounded by a ceramic housing to prevent losses and horizontal heat exchange. The setup tolerates temperatures of 1000 °C and is able to build temperature gradients of up to 600 °C accordingly.

We demonstrate the setup by characterizing a 4-leg module of oxide thermoelectrics p-type Li-NiO and n-type Al-ZnO with gold interconnects between 100-900 °C. We find a large discrepancy between individual materials parameters and experimentally obtained module performance and further decrease in module's performance upon thermal cycling. This underlines the necessity for long-term stability studies of thermoelectric materials in combination with interconnects under realistic operational conditions.

Publication I

Defects and polaronic electron transport in Fe_2WO_6

Raphael Schuler, Truls Norby, and Helmer Fjellvåg,

Physical Chemistry Chemical Physics, **2020**, 22, 15541-15548

PCCP

PAPER

View Article Online
View Journal | View Issue

Published on 23 June 2020. Downloaded by Universitetet I Oslo on 10/16/2020 7:43:57 PM.

Cite this: *Phys. Chem. Chem. Phys.*, 2020, **22**, 15541

Defects and polaronic electron transport in Fe_2WO_6

Raphael Schuler, Truls Norby and Helmer Fjellvåg*

We report the synthesis of phase pure Fe_2WO_6 and its structural characterization by high quality synchrotron X-ray powder diffraction, followed by studies of electric and thermoelectric properties as a function of temperature (200–950 °C) and pO_2 ($1–10^{-3}$ bar). The results are shown to be in accordance with a defect chemical model comprising formation of oxygen vacancies and charge compensating electrons at high temperatures. The standard enthalpy and entropy of formation of an oxygen vacancy and two electrons in Fe_2WO_6 are found to be 113(5) kJ mol^{-1} and 41(5) J mol^{-1} K^{-1}, respectively. Electrons residing as Fe^{2+} in the Fe^{3+} host structure act as charge carriers in a small polaron conducting manner. A freezing-in of oxygen vacancies below approximately 650 °C results in a region of constant charge carrier concentration, corresponding to an iron site fraction of $X_{Fe^{2+}} \cong 0.03$. By decoupling of mobility from conductivity, we find a polaron hopping activation energy of 0.34(1) eV and a charge mobility pre-exponential u_0 = 400(50) cm^2 kV^{-1} s^{-1}. We report thermal conductivity for the first time for Fe_2WO_6. The relatively high conductivity, large negative Seebeck coefficient and low thermal conductivity make Fe_2WO_6 an interesting candidate as an n-type thermoelectric in air, for which we report a maximum zT of 0.027 at 900 °C.

Received 24th March 2020,
Accepted 22nd June 2020

DOI: 10.1039/d0cp01588a

rsc.li/pccp

Introduction

Transition metal (TM) tungstates have received increasing scientific interest over the last decade due to possible applications in catalysis, supercapacitors and multiferroics.[1–3] Whereas the divalent TM tungstates (MWO_4) have been investigated intensively, the trivalent TM variants (M_2WO_6) remain largely unexplored. Nevertheless, due to its semiconducting nature, Fe_2WO_6 is of special interest. Its small bandgap (1.8 eV), relatively high electrical conductivity ($\sigma_{rt} \approx 0.02$ S cm^{-1}), and absorption in the visible light spectrum, make Fe_2WO_6 a candidate for photoanodes in photoelectrochemical cells.[4] The relatively high electrical conductivity is attributed to small polaron electrons that may be seen as Fe^{2+} states hopping along host Fe^{3+} zigzag chains. The crystal structure can be described as a superstructure variant of the α-PbO type (space group *Pbcn*) with unit cell parameters a = 4.578, b = 16.757, and c = 4.968 Å. The structure consists of zigzag chains of edge sharing WO_6 and FeO_6 octahedra along [001]. Bharati *et al.* reported a large positive Seebeck coefficient, indicating p-type conductivity.[5] However, several other publications have rather reported n-type conductivity. In this work, we provide an experimental assessment of defect chemical and electrical transport properties, providing a model of the origin and transport of charge carriers. Specifically, we address these question by first synthesizing phase pure samples of Fe_2WO_6 for which detailed crystallographic information, including possible vacancies at oxygen sites, is deduced from Rietveld refinement of high quality synchrotron X-ray powder diffraction data. By means of careful conductivity, and Seebeck coefficient measurements over a wide range of temperature and oxygen partial pressure, we clearly prove that Fe_2WO_6 is an n-type material. In order to support the findings from diffraction and electrical studies concerning the likeliness of oxygen vacancies being a cause for the interesting transport properties, XPS studies are undertaken for clarifying the potential presence of reduced Fe^{2+} species, that could act as charge carriers in a polaron hopping manner. To our knowledge, there exist no studies on thermal conductivity of Fe_2WO_6 in the literature so far, and we are the first ones to report this property. Our findings indicate a potential relevance of Fe_2WO_6 for high temperature thermoelectric applications. The field of thermoelectric oxides has yet to find a suitable n-type material, able to compete with the unmatched performance of the layered cobaltite p-type $Ca_3Co_4O_9$. With just a few systems showing promising results, *e.g.* TiO_2, $CaMnO_3$ and ZnO, the discovery of new high temperature stable n-type thermoelectric oxides is a valuable contribution in the search for better materials.

Experimental

Powder samples of Fe_2WO_6 were synthesized using standard solid-state reaction techniques. Stoichiometric amounts of the

---

Department of Chemistry, Centre for Materials Science and Nanotechnology, University of Oslo, POB 1126 Blindern, NO-0318 Oslo, Norway.
E-mail: raphael.schuler@smn.uio.no, truls.norby@kjemi.uio.no, helmer.fjellvag@kjemi.uio.no

This journal is © the Owner Societies 2020

View Article Online

Published on 23 June 2020. Downloaded by Universitetet I Oslo on 10/16/2020 7:43:57 PM.

starting materials Fe_2O_3 (STREM chemicals 99.8%), and WO_3 (Sigma Aldrich 99.9%) were mixed, thoroughly ground in an agate mortar and pressed into 10 mm pellets with a cylindrical die. The pellets were reacted at 950 °C for 16 hours in a covered alumina crucible. The pellets were reground and the procedure repeated until a single-phase product was confirmed by powder X-ray diffraction (XRD). Disk shaped pellets were produced by uniaxial pressing and sintering at 1100 °C for 6 hours in air. In house XRD measurements were obtained on a Bruker D8 Discover with CuKα1 radiation, Ge(111) Johanssen monochromator and a Lynxeye detector. High-resolution powder XRD patterns were measured at BM31 (SNBL) at ESRF (France), λ = 0.4943 Å using a Dexela 2923 CMOS two-dimensional detector. Structure refinement was carried out according to the Rietveld method using the TOPAS V5 software. Peak shapes were fitted using a pseudo Voigt peak shape. Corrections applied to the pattern included a second order Chebyshev polynomial, a broad background peak at $2\Theta = 7.5°$ and a cylindrical 2Θ correction term for the capillary geometry. A total of 39 independent parameters were used in the refinement for a total of 427 Bragg reflections in the range $4 \leq 2\Theta \leq 37°$.

Electrical conductivity and Seebeck coefficients were measured at high temperatures in a tube furnace with a custom-built assembly mounted setup in a ProboStat™ cell (NORECS AS, Oslo, Norway).[6] The disc shaped pellets were placed on an alumina plate with an integrated S-type thermocouple. Four Pt-electrodes were pressed on the top surface of the pellets in a van der Pauw geometry by springload. Two additional thermocouples made of 0.2 mm Pt and Pt/10Rh wire were pressed to the top surface of the pellet at a 6–8 mm distance. A resistive heater next to the sample provided a temperature difference of 4–6 °C across the sample. The setup allowed simultaneous measurement of in-plane Seebeck coefficient and in-plane conductivity under identical experimental conditions. A custom gas mixer with several O_2 + Ar dilution stages controlled the oxygen partial pressure. The sample was equilibrated at each of the selected oxygen partial pressures for 48 hours whereupon the Seebeck coefficient and conductivity data were measured.

Thermal conductivity was measured by the laser flash analysis method on a Netzsch LFA 457 MicroFLASH from 25 °C to 1000 °C in nitrogen flow. The graphite coated disk sample was irradiated with laser pulse lengths of 0.5 ms and a Netzsch Pyroceram standard sample was used to determine the specific heat. At 100 °C intervals, 3 measurements were taken at each temperature point, of which the mean value was determined.

Thermogravimetric analysis was carried out on a Netzsch TA 449 F1 Jupiter with a sample powder weight of 0.861 mg in an aliumina crucible. In order to reproduce the conditions of the conductivity measurements as precisely as possible, the chamber was flushed with 40 ml min^{-1} of synthetic air during the experiment and the same heating rate of 1 °C min^{-1} was set between 50 °C and 950 °C.

X-ray photoelectron spectroscopy (XPS) data was collected on a ThermoFisher Scientific Thetaprobe, with energy scale calibration relative to the Ag $3d_{5/2}$ peak at 368.21 eV and with the stage polarized to −16 V during experiments. XPS measurements were performed on freshly fractured surfaces of densely sintered pellets of Fe_2WO_6. Data analysis was carried out using CasaXPS software.[7] The spectra were corrected for Shirley backgrounds. Symmetric peaks were fitted using a Voigt peak shape (GL(50)). Asymmetric peaks were fitted using an asymmetric Lorenzian.

Results

The obtained fit to the synchrotron powder XRD pattern of Fe_2WO_6 is shown in Fig. 1. The Rietveld refinement analysis confirmed a single phase sample of Fe_2WO_6, crystallizing in space group *Pbcn*. There is no indication for any presence of secondary phases. In the refinement process, the occupancy of the W-site was fixed to 1.00. The results show complete occupation of all other sites except for the O3 site. Unit cell dimensions, atomic coordinates, occupancies and isotropic temperature factors are displayed in Table 1. The refinement converged to R_{wp}= 9.035, R_p = 7.121 (R_{exp}-value and goodness-of-fit are not relevant owing to the 2D detector statistics).[8] The structure consists of WO_6 and FeO_6 octahedra which form edge sharing chains in along [001] and corner sharing along [100] and [010]. The Fe1 site belongs to the chains solely consisting of FeO_6 octahedra, whereas the chains containing the Fe2 site

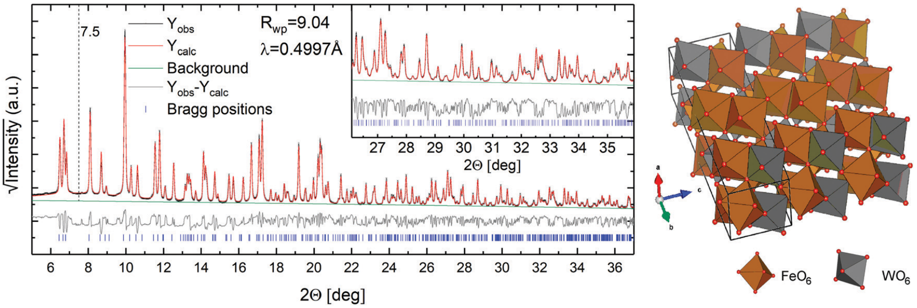

Fig. 1 Synchrotron X-ray powder diffraction pattern of Fe_2WO_6 with zoomed high angle region (inset). The intensity is displayed as square root to help emphasize weak reflections. The broad fitted background peak is marked by the dotted line at $2\Theta = 7.5°$.

This journal is © the Owner Societies 2020

Published on 23 June 2020. Downloaded by Universitetet I Oslo on 10/16/2020 7:43:57 PM.

Table 1 Crystallographic data for Fe_2WO_6 derived by Rietveld refinement of synchrotron powder X-ray diffraction data, space group *Pbcn*; *a* = 4.5607(1), *b* = 16.6938(4) and *c* = 4.9493(1) Å, (*Z* = 4). Calculated standard deviations in parentheses

Atom	Multipl.	*x*	*y*	*z*	Occ.	Beq.
O1	8	0.232(2)	0.2065(8)	0.069(2)	1.00(4)	0.60(18)
O2	8	0.257(2)	0.0393(7)	0.108(3)	1.00(4)	0.60(18)
O3	8	0.282(2)	0.3724(10)	0.074(2)	0.98(2)	0.60(18)
W	4	0	0.11211(8)	0.25	1	1.59(3)
Fe1	4	0	0.44424(17)	0.25	1.000(9)	0.19(5)
Fe2	4	0	0.77651(19)	0.25	1.000(8)	0.19(5)

consist of alternating WO_6 and FeO_6 octahedra. The refinements indicate a presence of vacancies at the O3 site. Both the O1 and O2 anions are exclusively linking Fe2–W–Fe2 and Fe1–W–Fe1 octahedra, respectively. On the other hand, the O3 site connects the Fe1 and Fe2 sites, thereby providing linkage to the pure FeO_6 and the alternating WO_6–FeO_6 chains. The occupation refinement points towards a stoichiometry of $Fe_2WO_{5.96}$, but the quantification of the oxygen under-stoichiometry is accompanied by considerable uncertainty (as seen by the calculated standard deviations), owing to the light oxygen atoms (Nb. 8) compared to the electron rich tungsten (Nb. 74). High quality neutron diffraction data appears required to provide more accurate determination of the non-stoichiometry at the O-sites.

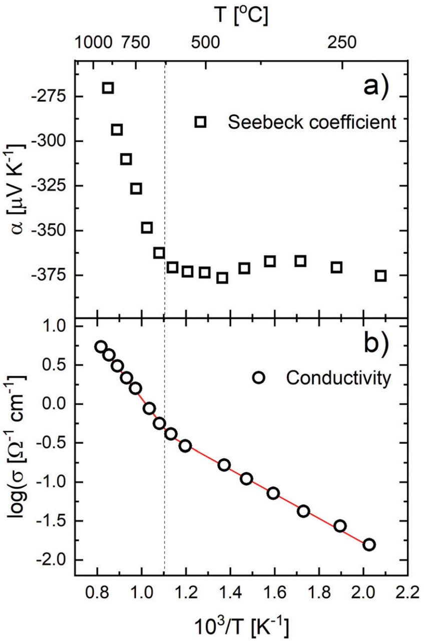

Fig. 2 Inverse temperature dependence of (a) Seebeck coefficient and (b) conductivity of Fe_2WO_6 in air.

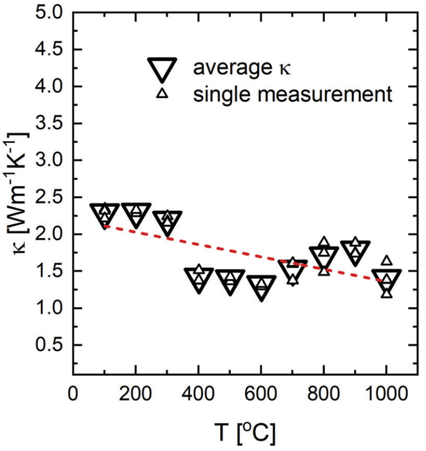

Fig. 3 Thermal conductivity determined by Laser Flash Analysis. The dotted line is a guide to the eye indicating the decreasing trend.

Fig. 2a shows the Seebeck coefficient as a function of inverse temperature. It remains large and negative with two recognizable regions, delimited at about 650 °C. The decrease in magnitude of the Seebeck coefficient at higher temperatures indicates an increasing charge carrier concentration whereas the low temperature range indicates a constant charge carrier concentration as seen by an almost constant Seebeck coefficient. Noteworthy, the Seebeck data reported by Bharati *et al.* has similar absolute values, but of positive sign. Hence, they discuss their findings under the assumption that holes are the dominant charge carriers. Support to the present findings is provided by various reports on n-type conductivity from qualitative Seebeck measurements.[9,10] The electrical conductivity as a function of inverse temperature is shown in Fig. 2b. The conductivity increases with temperature in a thermally activated manner, depicting two straight lines in the logarithmic plot, with a change in slope around 650 °C, coinciding with the transition in the Seebeck coefficient.

The thermal conductivity of Fe_2WO_6, depicted in Fig. 3 is no strong function of temperature, despite some fluctuation, and shows a declining trend with increasing temperature, reaching a minimum of 1.25 W m^{-1} K^{-1} at 600 °C. The low thermal conductivity can be attributed to the low dimensionality of the structure and large unit cell.

It has been suggested that oxygen non-stoichiometry may play an important role in Fe_2WO_6, but to our knowledge there are no detailed studies at hand.[11] Thermogravimetric analysis in air, depicted in Fig. 4, shows a nearly constant sample weight below 600 °C with minor fluctuations, attributed to buoyance of the scale. Above 650 °C a close to linear weight loss can be observed, followed by an equivalent weight gain during the cooling process, flattening out below about 600 °C with a slight hysteresis.

Fig. 5 shows the electrical conductivity and charge carrier concentration from Seebeck coefficient measurements at various oxygen partial pressures, and measured simultaneously at 750 °C. For consistency, the charge carrier concentration is expressed as Fe^{2+} site fraction obtained from the Seebeck coefficient, which will

Published on 23 June 2020. Downloaded by Universitetet I Oslo on 10/16/2020 7:43:57 PM.

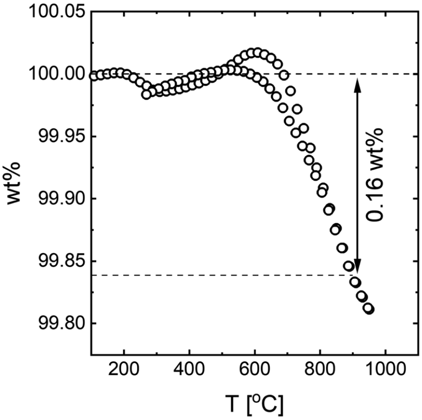

Fig. 4 Thermogravimetric analysis of Fe_2WO_6 in air during heating and cooling ramps of 1 °C min^{-1} in accordance with the conductivity and thermopower measurements. The weight loss from the baseline to 900 °C is indicated.

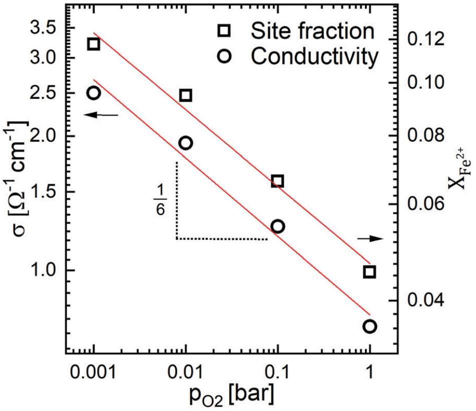

Fig. 5 Brouwer diagram showing logarithmic conductivity and charge carrier concentration given as Fe^{2+} site fraction, obtained from Seebeck measurements, as function of oxygen partial pressure. The data were collected isothermally at 750 °C. Both datasets show slopes of around −1/6.

be discussed later. The dependency remains negative over the investigated p_{O_2} region, with a slope of the order of −1/6 for both conductivity and charge carrier concentration, as expected for non-stoichiometry dominated by oxygen vacancies.

Fig. 6a shows a narrow scan of the iron 2p region of the X-ray photoelectron (XPS) spectrum of Fe_2WO_6 at room temperature. The two well separated spin–orbit features $2p_{3/2}$ and $2p_{1/2}$ at 710.8 eV and 724.4 eV are visible. The typical Fe^{3+} satellite peak at 719.39 eV is clearly distinguishable and shows the typical shift of 8.6 eV towards higher binding energies. The intensity ratio between the $2p_{1/2}$ and $2p_{3/2}$ peaks matches closely the ratio of 1 : 2 (1 : 1.994), which is typical for Fe_2O_3. This indicates that the Fe^{3+} atoms in Fe_2WO_6 have similar electronic properties as in Fe_2O_3.[12] However, the Fe $2p_{3/2}$ peak is fitted insufficiently when using only one component. Fig. 6a shows an additional shoulder at low binding energy and a weak, broad feature at higher binding energy. The latter feature is attributed to a surface signal, similar to what has been reported for Fe_2O_3.[12] Surface peaks are considered to arise for a freshly cleaved surface that leaves atoms at the surface with a reduced coordination.[13,14] The shoulder at lower binding energy is typical for FeO and Fe^{2+} containing compounds and is taken as an indication of the presence of Fe^{2+} species in the Fe^{3+} host structure. The presence of Fe^{2+} species in Fe_2WO_6 has been discussed in earlier literature.[15] The area ratio between the Fe 2p peaks of Fe^{3+} and the Fe^{2+} shoulder indicates a site fraction of approximately 0.03 (see Table 2). It appears that Fe_2WO_6 in this way behaves quite similar to its Fe^{2+} sister compound $FeWO_4$ which in turn has been found to host small amounts of Fe^{3+} as (p-type, hole) conducting species.[16]

Fig. 6b shows an XPS narrow scan for the tungsten 4f region. The $4f_{7/2}$ and $4f_{5/2}$ spin orbit peaks were fitted with symmetric Voigt functions and are located at 35.3 eV and 37.4 eV, split by 2.14 eV. The intensity ratio of 1 : 1.308 closely matches the

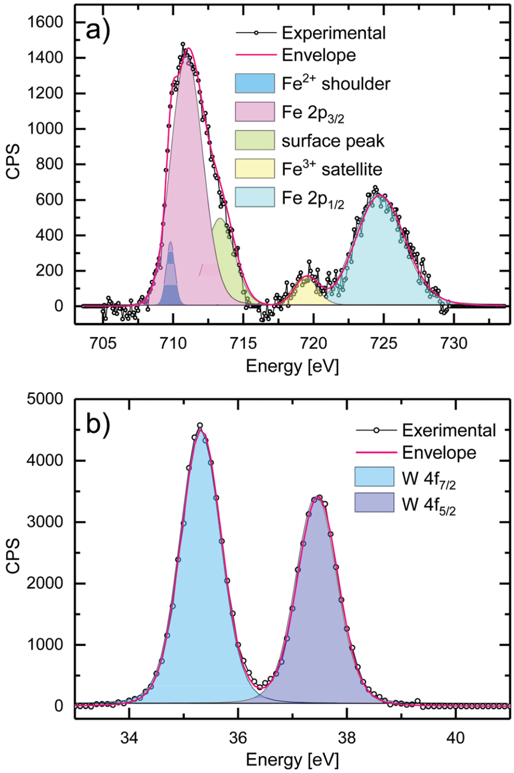

Fig. 6 Shirley background subtracted close up X-ray photoelectron spectra of (a) Fe 2p and (b) W 4f signals in Fe_2WO_6.

This journal is © the Owner Societies 2020

Published on 23 June 2020. Downloaded by Universitetet I Oslo on 10/16/2020 7:43:57 PM.

Table 2 Parameters derived from fitting of XPS data for the Fe 2p, W 4f and reference Ag 3d peak regions

Signal	Position (eV)	FWHM (eV)	Area
Fe $2p_{3/2}$	710.80	2.63	4066
Fe $2p_{1/2}$	724.39	4.09	2839
Fe^{3+} satellite	719.40	1.99	357
Fe^{2+} shoulder	709.87	0.68	256
Surface peak	713.33	2.44	1340
W $4f_{7/2}$	35.32	0.86	4367
W $4f_{5/2}$	37.46	0.87	3339
Ag $3d_{5/2}$	368.21	0.55	29 839

typical f subshell ratio of 3 : 4. These XPS data show close resemblance to those of WO_3 with W^{6+} in fully oxidized state. No sign of any shoulder at lower binding energies is visible, which would be indicative of tungsten in a lower oxidation state. Peak positions, FWHM, and integrated area are summarized in Table 2.

Discussion

The n-type conductivity in Fe_2WO_6 can be assigned to mixed iron valence with Fe^{2+} species being the active conducting species hopping along the Fe^{3+} host sites. We make use of the modified Heikes formula for transition metal oxides, containing the degeneracy factors of the valence states, to estimate the charge carrier concentration from the Seebeck coefficient.[17,18]

$$\alpha = -\frac{k_B}{e}\ln\left(\frac{g_{Fe^{3+}}}{g_{Fe^{2+}}}\frac{(1 - X_{Fe^{2+}})}{X_{Fe^{2+}}}\right) \tag{1}$$

Here, α is the Seebeck coefficient, k_B the Boltzmann constant, e the elemental charge, and $X_{Fe^{2+}}$ denotes the number of Fe^{2+} per iron site $\left(X_{Fe^{2+}} = \frac{[Fe^{2+}]}{[Fe^{3+}] + [Fe^{2+}]}\right)$. The factors $g_{Fe^{2+}}$ and $g_{Fe^{3+}}$ take into account the degeneracies for Fe^{2+} and Fe^{3+} states. In Fe_2WO_6, Fe^{3+} exists in the non-degenerate d^5_{hs} configuration with spin 5/2, and thus the degeneracy factor is $g_{Fe^{3+}} = 6$. Fe^{2+} has been shown to exist in d_{hs}^6 state in both FeO and $FeWO_4$ and is expected to keep the high spin configuration of $(t_{2g}\uparrow^3)(t_{2g}\downarrow^1)(e_g\uparrow^2)$ in Fe_2WO_6 as well. The large crystal field splitting leaves the sixth d electron to enter the lower lying, triply degenerate $(t_{2g}\downarrow)$ orbital, with a total spin of 2, the degeneracy factor is thus given by $g_{Fe^{2+}} = 15$.[19,20] The site fraction calculated accordingly from Seebeck data is shown in Fig. 7 and decreases towards lower temperatures until it becomes almost constant below 650 °C with a value of $X_{Fe^{2+}} \cong 0.031–0.034$, corresponding to a charge carrier concentration of approximately $6.9(5) \times 10^{20}$ cm^{-3}. In the following, we will refer to these two regions as the equilibrium and frozen-in regions.

The temperature dependent site fraction of Fe^{2+} as deduced from the Seebeck data and the oxygen non-stoichiometry data derived from XRD and XPS data are in good overall agreement taking the accuracies of the methods and analyses into account. The room temperature XRD data suggest that the oxygen vacancies occur only at one of the three oxygen sites (O3). We assume that this situation is maintained also at high temperatures.

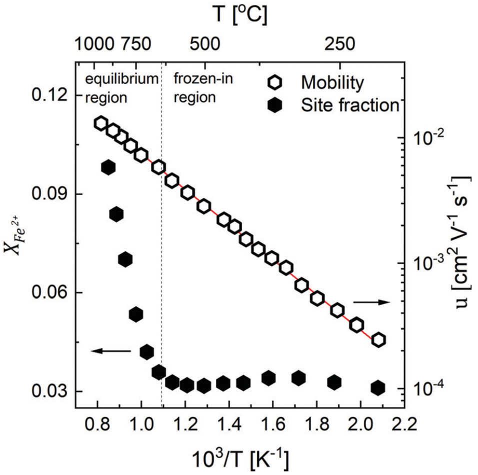

Fig. 7 Site fraction ($X_{Fe^{2+}}$) of Fe^{2+} in Fe_2WO_6 obtained from Heikes formula and charge carrier mobility (u) obtained from combination with conductivity data. The dotted line indicates transition from the equilibrium region to the frozen-in region around 650 °C.

Since there are two O3 atoms and two Fe atoms per Fe_2WO_6 formula unit, the electroneutrality condition for electrons (*i.e.* Fe^{2+}) that are charge compensating the oxygen vacancies at the O3-site can be expressed as site fractions according to Kröger–Vink notation as

$$X_{Fe^{2+}} = 2X_{v_{O3}^{\bullet\bullet}} \tag{2}$$

The formation of O3 oxygen vacancies and Fe^{2+} species reads

$$2Fe_{Fe}^{x} + O_{O3}^{x} = v_{O3}^{\bullet\bullet} + 2Fe_{Fe^{3+}}^{2+\prime} + \frac{1}{2}O_2 \tag{3}$$

The equilibrium coefficient, including the electron degeneracy is given by

$$K_{v_{O3}^{\bullet\bullet}} = \frac{a_{v_{O3}^{\bullet\bullet}}\left(g_{Fe^{2+}}a_{Fe_{Fe^{3+}}^{2+\prime}}\right)^2}{a_{O_{O3}^{x}}\left(g_{Fe^{3+}}a_{Fe_{Fe}^{x}}\right)^2}p_{O_2}{}^{\frac{1}{2}} = \frac{\left[v_{O3}^{\bullet\bullet}\right]\left(g_{Fe^{2+}}\left[Fe_{Fe^{3+}}^{2+\prime}\right]\right)^2}{\left[O_{O3}^{x}\right]\left(g_{Fe^{3+}}\left[Fe_{Fe}^{x}\right]\right)^2}p_{O_2}{}^{\frac{1}{2}} \tag{4}$$

In the approximation of small defect concentrations we can express the oxygen vacancy and Fe^{2+} concentrations as site fractions and the equilibrium coefficient simplifies to

$$K_{v_{O3}^{\bullet\bullet}} = X_{v_{O3}^{\bullet\bullet}}\left(\frac{g_{Fe^{2+}}}{g_{Fe^{3+}}}\right)^2(X_{Fe^{2+}})^2 p_{O_2}{}^{\frac{1}{2}} \tag{5}$$

By assuming the electroneutrality condition (2) eqn (5) can be rearranged to

$$X_{Fe^{2+}} = \left(2K_{v_{O3}^{\bullet\bullet}}\right)^{\frac{1}{3}}\left(\frac{g_{Fe^{2+}}}{g_{Fe^{3+}}}\right)^{-\frac{2}{3}}p_{O_2}{}^{\frac{1}{6}} \tag{6}$$

The charge carrier site fraction can be obtained indirectly from its proportionality to conductivity *via* the charge mobility

Published on 23 June 2020. Downloaded by Universitetet I Oslo on 10/16/2020 7:43:57 PM.

or directly from the Seebeck coefficient as depicted in Fig. 5. The two methods are independent and both datasets exhibit the characteristic slope of −1/6 in the double logarithmic Brouwer plot.

The transition temperature of 650 °C from equilibrium to frozen-in region coincides with the onset of weight loss in the thermogravimetric measurement. Between 500 °C to 900 °C a fully reversible weight loss of 0.16 wt% is observable. Assuming this weight loss is solely due to the proposed formation of oxygen vacancies, 0.16 wt% correspond to an oxygen site fraction of $\Delta X_{\nu_{\mathrm{O3}}^{\bullet\bullet}} = 0.039$. Following the electroneutrality condition (2) this corresponds to a $\Delta X_{\mathrm{Fe}^{2+}} = 0.078$, which is in close agreement with the charge carrier increase of $\Delta X_{\mathrm{Fe}^{2+}} = 0.068$ in the equilibrium region, visible in Fig. 7.

This typical behavior confirms our model on the formation of doubly charged oxygen vacancies as the source of the n-type charge carriers in form of reduced Fe^{2+} species in $\mathrm{Fe_2WO_6}$ under equilibrium conditions. We can accordingly formulate the chemical sum formula as $\mathrm{Fe}_{2-X}{}^{3+}\mathrm{Fe}_X{}^{2+}\mathrm{WO}_{6-X/2}$.

We can now parameterize the defect chemical reaction (3) by expressing the temperature dependent equilibrium coefficient $K_{\nu_{\mathrm{O3}}^{\bullet\bullet}}$ by means of the van't Hoff equation, allowing us to extract the standard enthalpy of formation and the associated standard entropy change.

$$K_{\nu_{\mathrm{O3}}^{\bullet\bullet}} = \exp\left(\frac{\Delta S^{\Theta}_{\nu_{\mathrm{O3}}^{\bullet\bullet}}}{k}\right)\exp\left(-\frac{\Delta H^{\Theta}_{\nu_{\mathrm{O3}}^{\bullet\bullet}}}{kT}\right) \tag{7}$$

From the van 't Hoff plot in Fig. 8, we obtain a standard formation enthalpy of 113(5) kJ mol^{-1} [1.18(5) eV] from the slope and a standard entropy change of 41(5) J mol^{-1}K^{-1} from the intersect. The model established for the charge carrier concentration in equilibrium with oxygen, allows us to decouple the mobility from the conductivity and to describe it in a frame of thermally activated polaron hopping ($u < 0.1$ cm^2 V^{-1} s^{-1}).[21] We use quantitative charge carrier concentrations for this *via* $n = 8X_{\mathrm{Fe2}\ +}/V$ (V is the unit cell volume of 376.83×10^{-24} cm^{-3}).

$$\sigma = enu = enu_0\frac{1}{T}\exp\left(-\frac{E_\mathrm{u}}{k_\mathrm{B}T}\right) \tag{8}$$

Here, e is the elemental charge, n the charger carrier concentration, and k_B Boltzmann's constant. E_u is the activation energy for hopping, u_0 is the mobility pre-factor. The mobility prefactor is dependent on whether the polaron hopping is adiabatic or non-adiabatic.

$$\begin{aligned} u_0 &= \frac{zed^2\nu_\mathrm{ph}}{2k_\mathrm{B}} \quad \text{Adiabatic} \\ u_0 &= \frac{zed^2}{2k_\mathrm{B}}\frac{J^2}{2h}\left(\frac{\pi}{4E_\mathrm{u}k_\mathrm{B}T}\right)^{\frac{1}{2}} \quad \text{Non-adiabatic} \end{aligned} \tag{9}$$

here ν_ph denotes the maximum longitudinal phonon frequency, J the overlap integral, and z is the number of neighboring sites in jump distance d. We consider the Fe1–Fe1 distance of 3.097 Å to be the most relevant jump distance as it corresponds to the edge sharing octahedra along the crystallographic c-axis. The structure of hexagonal close packed oxygen with half of the octahedral voids filled, results in two nearest Fe neighbors ($z = 2$). By comparing the two mechanisms on the basis of the adiabatic parameter η_2, one can deduce the actual transport mechanism ($\eta_2 > 1$ for adiabatic, $\eta_2 \ll$ for non-adiabatic).[22,23]

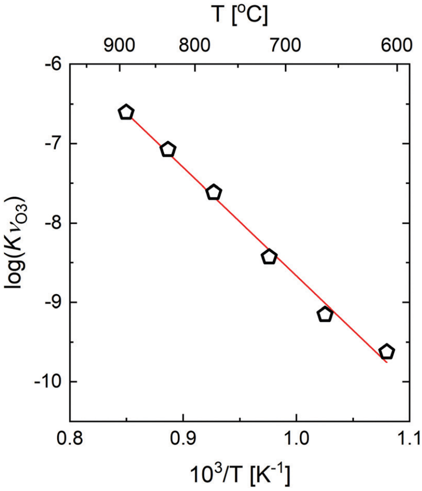

Fig. 8 van't Hoff plot of equilibrium coefficient *versus* inverse temperature. The equilibrium coefficient is obtained from eqn (5) taking into account the electroneutrality as stated in eqn (2).

$$\eta_2 = \frac{J^2}{h\nu_\mathrm{ph}}\left(\frac{1}{E_\mathrm{u}k_\mathrm{B}T}\right)^{\frac{1}{2}} \tag{10}$$

The polaron hopping activation energy of $E_\mathrm{u} = 0.34(1)$ eV was obtained from the slope in the Arrhenius plot and is invariant in both the equilibrium- and frozen-in regions. In the frozen-in region E_u corresponds to the conductivity activation energy [$E^\mathrm{f}_\sigma = 0.35(1)$ eV from $\ln(\sigma T)$ *vs.* $1/T$] and is in good agreement with previously reported values of 0.33 eV.[5] From the adiabatic mobility pre-exponential we estimate a maximum optical phonon frequency of $\nu_\mathrm{ph} = 3.3(2) \times 10^{13}$ Hz. No comparable phonon frequencies are available experimentally for $\mathrm{Fe_2WO_6}$. However, the frequency lies rather close to typical maximum optical frequencies of $\mathrm{Fe_2O_3}$ (1.9×10^{13} Hz) and $\mathrm{WO_3}$ (3.23×10^{13} Hz).[24,25] We obtain an overlap integral of $J = 0.28(1)$ eV from a $\ln(uT^{3/2})$ *vs.* $1/T$ plot and conclude on an adiabatic polaron hopping, as the adiabatic parameter exceeds unity $\eta_2 \gg 1$.

The mobility obtained from combination of charge carrier concentration with conductivity data is depicted as a function of inverse temperature in Fig. 7, and a complete description of the mobility reads

$$u = 400(50)\ \mathrm{cm^2\ KV^{-1}\ s^{-1}}\frac{1}{T}\exp\left(\frac{0.34(1)\ \mathrm{eV}}{k_\mathrm{B}T}\right) \tag{11}$$

Furthermore, we may derive an expression for the conductivity in the equilibrium region that includes variable charge

This journal is © the Owner Societies 2020

Published on 23 June 2020. Downloaded by Universitetet I Oslo on 10/16/2020 7:43:57 PM.

carrier concentration by combining eqn (6)–(8) (Absolute charge carrier concentrations in cm^{-3} are used). As only the mobility activation term and the enthalpy of formation term are temperature dependent, the conductivity activation energy in the equilibrium region in Fig. 2b is the sum of the activation energy for polaron hopping and the standard enthalpy of formation of oxygen vacancies

$$\sigma_{\mathrm{eq}} = \frac{eu_0}{T}\frac{2^{\frac{1}{3}}8}{V}\left(\frac{g_{\mathrm{Fe}^{2+}}}{g_{\mathrm{Fe}^{3+}}}\right)^{-\frac{2}{3}} p_{\mathrm{O}_2}{}^{-\frac{1}{6}} \exp \ \frac{\Delta S^{\Theta}_{\nu^{\bullet\bullet}_{\mathrm{O3}}}}{3k}\Bigg) \exp\left(\frac{-E^{\mathrm{eq}}_{\sigma}}{kT}\right),$$

$$\text{with } E^{\mathrm{eq}}_{\sigma} = \frac{\Delta H^{\Theta}_{\nu^{\bullet\bullet}_{\mathrm{O3}}}}{3} + E_{\mathrm{u}} \qquad (12)$$

From the conductivity activation energy E^{eq}_{σ} = 0.79(4) eV in the equilibrium region and with the polaron hopping activation energy E_{u} = 0.34(1) eV we estimate a standard enthalpy of formation of 130(15) kJ mol^{-1} [1.35(15) eV]. The intersect allows for an estimate of the standard entropy change of 56(20) J mol^{-1} K^{-1}, which is close to the empirically expected 60 J mol^{-1} K^{-1} upon the release of half a mole of gaseous oxygen. The thermodynamic parameters from the conductivity analysis largely agree with those obtained from the charge carrier site fraction, albeit with higher standard deviations, since more terms are involved.

The relatively high conductivity, large Seebeck coefficient, and low thermal conductivity in addition to its remarkable stability towards temperature and oxidizing conditions, make Fe_2WO_6 an interesting n-type material for thermoelectric applications. The power factor ($\alpha^2\sigma$) increases exponentially with temperature, governed by the activated conductivity and reaches the highest observable value of 42 μWK^{-2} m^{-1} at 950 °C. As the thermal conductivity stays low over the entire temperature range, the dimensionless figure of merit $\left(zT = \frac{\alpha^2\sigma}{\kappa}T\right)$ follows the course of the power factor closely, as evident in Fig. 9, reaching zT = 0.027 at 900 °C. It should be noted that the samples in this study are undoped and that further improvements in the thermoelectric performance should be pursued by exploring doping of the system.

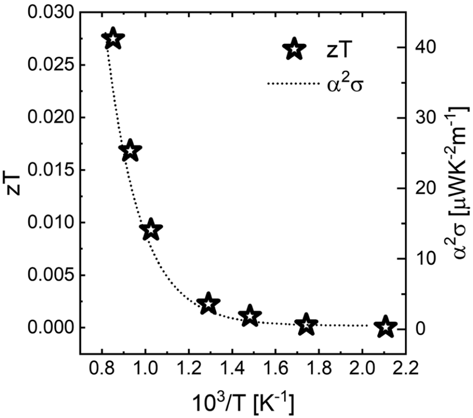

Fig. 9 Dimensionless figure of merit $\left(zT = \frac{\sigma\alpha^2}{\kappa}T\right)$ and power factor (PF = $\sigma\alpha^2$) in air as function of temperature for Fe_2WO_6.

Conclusions

In this work, we have established a defect chemical model to describe the electrical transport and the oxygen non-stoichiometry in Fe_2WO_6. Conductivity and Seebeck coefficient measurements concluded Fe_2WO_6 is an n-type conductor over the entire temperature and oxygen partial pressure ranges investigated. From detailed refinements of high quality synchrotron X-ray powder diffraction data, we could show that one of the oxygen sites (O3) is a preferred oxygen deficient site. Oxygen vacancies are compensated by reduced Fe^{2+} species, acting as charge carriers in an adiabatic polaron hopping manner. At high temperatures the material is in chemical equilibrium with atmospheric oxygen and forms oxygen vacancies and charge carriers with a standard formation enthalpy of 130(15) kJ mol^{-1} and a corresponding standard change in entropy of 41(5) J $mol^{-1}K^{-1}$. A freezing-in of oxygen vacancies below 650 °C results in a region of constant charge carriers, with a Fe^{2+} site fraction of $X_{\mathrm{Fe}^{2+}} \cong 0.03$. We show that the polaron hopping activation energy of 0.34(1) eV is constant across both regions, which reconciles the conductivity and chemical equilibrium model. We measure a low thermal conductivity for Fe_2WO_6, which was reported for the first time. The stability at high temperatures and oxidizing conditions makes Fe_2WO_6 a promising n-type thermoelectric oxide with a zT of 0.027 at 900 °C.

Conflicts of interest

There are no conflicts of interest to declare.

References

1 K. Hoang, M. Oh and Y. K. Choi, Electronic structure, polaron formation, and functional properties in transition-metal tungstates, *RSC Adv.*, 2018, **8**(8), 4191–4196.
2 O. Heyer, *et al.*, A new multiferroic material: $MnWO_4$, *J. Phys.: Condens. Matter*, 2006, **18**(39), L471–L475.
3 R. D. Kumar and S. Karuppuchamy, Microwave-assisted synthesis of copper tungstate nanopowder for supercapacitor applications, *Ceram. Int.*, 2014, **40**(8), 12397–12402.
4 F. F. Abdi, *et al.*, Assessing the Suitability of Iron Tungstate (Fe_2WO_6) as a Photoelectrode Material for Water Oxidation, *J. Phys. Chem. C*, 2017, **121**(1), 153–160.
5 R. Bharati and R. A. Singh, The electrical properties of Fe_2WO_6, *J. Mater. Sci.*, 1981, **16**(2), 511–514.
6 M. Schrade, *et al.*, Versatile apparatus for thermoelectric characterization of oxides at high temperatures, *Rev. Sci. Instrum.*, 2014, **85**(10), 103906.
7 C. S. Ltd, *CasaXPS Version 2.3.19PR1.0*, Casa Software Ltd.
8 L. B. McCusker, *et al.*, Rietveld refinement guidelines, *J. Appl. Crystallogr.*, 1999, **32**(1), 36–50.

Published on 23 June 2020. Downloaded by Universitetet I Oslo on 10/16/2020 7:43:57 PM.

9 K. Sieber, *et al.*, Preparation and Properties of Substituted Iron Tungstates, *J. Solid State Chem.*, 1983, **47**(3), 361–367.

10 H. Leiva, K. Dwight and A. Wold, Preparation and Characterization of Conducting Iron Tungstates, *J. Solid State Chem.*, 1982, **42**(1), 41–46.

11 S. N. Panja, J. Kumar, L. Harnagea, A. K. Nigam and S. Nair, Magnetic and dielectric investigations of $\gamma - Fe_2WO_6$, *J. Magn. Magn. Mater.*, 2018, 354–358.

12 T. Yamashita and P. Hayes, Analysis of XPS spectra of Fe^{2+} and Fe^{3+} ions in oxide materials, *Appl. Surf. Sci.*, 2008, **254**(8), 2441–2449.

13 M. Bronold, Y. Tomm and W. Jaegermann, Surface states on cubic d-band semiconductor pyrite (FeS_2), *Surf. Sci.*, 1994, **314**(3), 931–936.

14 T. Droubay and S. A. Chambers, Surface-sensitive Fe 2p photoemission spectra for α-Fe_2O_3: the influence of symmetry and crystal-field strength, *Phys. Rev. B: Condens. Matter Mater. Phys.*, 2001, **64**(20), 205414.

15 T. Birchall, C. Hallett, A. Vaillancourt and K. Ruebenbauer, *et al.*, A study of iron-tungsten oxides and iron-chromium-tungsten oxides, *Can. J. Chem.*, 1988, **66**(4), 698–702.

16 E. Schmidbauer, U. Schanz and F. J. Yu, Electrical transport properties of mono- and polycrystalline $FeWO_4$, *J. Phys.: Condens. Matter*, 1991, **3**(3), 5341–5352.

17 P. M. Chaikin and G. Beni, Thermopower in the correlated hopping regime, *Phys. Rev. B: Solid State*, 1976, **13**(2), 647–651.

18 W. Koshibae, K. Tsutsui and S. Maekawa, Thermopower in cobalt oxides, *Phys. Rev. B: Condens. Matter Mater. Phys.*, 2000, **62**(11), 6869–6872.

19 N. Guskos, *et al.*, Magnetic and EPR Studies of α-, β-, and γ-Fe_2WO_6 Phases at Low Temperatures, *J. Solid State Chem.*, 1995, **120**(2), 216–222.

20 K. Sieber, *et al.*, Preparation and photoelectronic properties of $FeWO_4$, *Mater. Res. Bull.*, 1982, **17**(6), 721–725.

21 I. G. Austin and N. F. Mott, Polarons in Crystalline and Non-Crystalline Materials, *Adv. Phys.*, 1969, **18**(71), 41–102.

22 J. M. Casado, J. H. Harding and G. J. Hyland, Small-Polaron Hopping in Mott-Insulating Uo_2, *J. Phys.: Condens. Matter*, 1994, **6**(25), 4685–4698.

23 I. G. L. A. Y. A. Firsov, Kinetic theroy of semiconductors with low mobility, *J. Exp. Theor. Phys.*, 1963, **16**(5), 1843–1860.

24 S. Onari, T. Arai and K. Kudo, Infrared lattice vibrations and dielectric dispersion in a-Fe_2O_3, *Phys. Rev. B: Solid State*, 1977, **16**(4), 1717–1721.

25 Y. Ping, D. Rocca and G. Galli, Optical properties of tungsten trioxide from first-principles calculations, *Phys. Rev. B: Condens. Matter Mater. Phys.*, 2013, **87**, 165203.

This journal is © the Owner Societies 2020

Publication II

Near-broken gap alignment between $FeWO_4$ and Fe_2WO_6 for ohmic direct p-n junction thermoelectrics

Raphael Schuler, Federico Bianchini, Truls Norby, Helmer Fjellvåg

(Submitted to ACS Applied Materials & Interfaces)

Near-broken gap alignment between $FeWO_4$ and Fe_2WO_6 for ohmic direct p-n junction thermoelectrics

Raphael Schuler,* Federico Bianchini,* Truls Norby,* and Helmer Fjellvåg*

University of Oslo, Department of Chemistry, Centre for Materials Science and Nanotechnology (SMN), POB 1126 Blindern, NO-0318 Oslo, Norway

E-mail: raphael.schuler@smn.uio.no; federico.bianchini@smn.uio.no; truls.norby@kjemi.uio.no; helmer.fjellvag@kjemi.uio.no

Abstract

We report a near-broken gap alignment between p-type $FeWO_4$ and n-type Fe_2WO_6, a model pair for the realization of ohmic direct junction thermoelectrics. Both undoped materials have a large Seebeck coefficient and high electrical conductivity at elevated temperatures, due to inherent electronic defects. A band alignment diagram is proposed based on x-ray photoelectron and ultraviolet-visible light reflectance spectroscopy. Experimentally acquired non-rectifying I-V characteristics and the constructed band alignment diagram support the proposed formation of a near-broken gap junction. We have additionally performed computational modelling based on density functional theory (DFT) on bulk models of the individual compounds to rationalize the experimental band alignment diagram, and to provide deeper insight into the relevant band characteristics. The DFT calculations confirm an Fe-3d character of the involved band edges, which we suggest is a decisive feature for the unusual band overlap.

Introduction

A known problem of state-of-the-art thermoelectric generators (TEGs) is their low thermal stability and poor environmental friendliness, as they are built up from low melting point inter-metallic alloys, containing toxic and scarce elements like Pb, Te, and Bi. The use of oxide thermoelectrics promises increased temperature stability, better environmental compatibility and lower costs through the use of more abundant elements, and is hence likely to expand the field of application of thermoelectrics.[1,2] TEGs however, are not only limited by the thermoelectric (TE) materials properties, but also by the electric and thermal contacts between the materials and the metal interconnects, which pose additional challenges.[3,4] It is essential to establish good non-rectifying ("ohmic") contacts between the TE material and the metal interconnect, while avoiding interdiffusion, melting, and oxidation of the contact materials. This often makes it unavoidable to use expensive noble metal interconnects. At the same time, it must be ensured that the thermal expansion coefficients of the individual components such as TE materials, interconnect, solder, and diffusion barrier do not differ too much from one another in order to avoid failure of the module during thermal cycling.[5]

Many of these issues could be tackled by the approach of Shin *et al.* through the use of oxide thermoelectrics with a direct p-n junction hereby omitting the metal interconnects at the hot side.[6–8] However, p-n junctions are usually not ohmic, but exhibit rectifying behavior, which represent large parasitic resistances in the device. A solution to the rectifying behavior is a broken gap junction couple, well known in the field of photovoltaics.[9–11] A broken gap junction forms a charge accumulation region instead of a charge depletion zone, which leads to fully ohmic characteristics.

In this work, we study the p-n junction of the thermoelectric couple p-type $FeWO_4$ and n-type Fe_2WO_6. The two phases show no reactivity towards each other and can be regarded as coexistent. We combine experimental studies with *ab initio* calculations on the individual materials to establish a model for the band alignment between the two materials. Our findings support a near-broken gap junction alignment, with a non-rectifying junction behavior. The implementation of broken-gap junctions in direct junction TEGs, could give them a significant advantage over their diode-like alternatives without the need of high temperature thermionic emission.

Experimental

Fe_2WO_6 was synthesized by standard solid state reaction route. The starting materials Fe_2O_3 (STREM chemicals 99.8%), and WO_3 (sigma Aldrich 99.9%) were mixed stoichiometrically, thoroughly ground in an agate mortar, and pressed into 10 mm pellets with a cylindrical die. The pellets were reacted at 950 ℃ for 16 h in a covered alumina crucible. The pellets were reground and the procedure repeated three times until a single phase product was confirmed by powder XRD. A dense pellet of 87% relative density was fabricated by sintering at 1050 ℃ for 4 h in air. $FeWO_4$ was synthesized by mixing Fe_2O_3 (STREM chemicals 99.8%), Fe (sigma Aldrich $\leq$99.9%) and WO_3 stoichiometrically, thorough grinding in an agate mortar, sealing in an evacuated quarz tube and reacting at 950 ℃ for 48 h. The powder was reground and the procedure repeated for a total of 200 h reaction time until a single phase product was confirmed by powder XRD. A cylindrical pellet with a relative density of 85% was obtained by sintering a pressed powder pellet at 1150 ℃ for 4 h in argon atmosphere. In-house x-ray diffraction measurements were performed on a Bruker D8 Discover with Cu K-alpha-1 radiation, Ge (111) Johanssen monochromator and Lynxeye detector. Structural refinement was carried out in a Rietveld refinement using the software TOPAS V5. Optical reflectance spectroscopy was measured on each material separately with a *OceanOptics* USB2000+ spectrometer and a halogen lamp light source at room temperature. The background was calibrated to the reflectance spectrum of a $BaSO_4$ reference sample.

X-ray photoelectron spectroscopy (XPS) was performed on a ThermoFisher Scientific Thetaprobe, with carefully calibrated energy scale to the Ag $3d_{\frac{5}{2}}$ peak of 368.21 eV binding energy with the stage polarized to -16 V during the experiments. XPS experiments were carried out on freshly broken surfaces of the respective sintered pellets of $FeWO_4$ and Fe_2WO_6. Electrical conductivity and Seebeck coefficient at high temperatures were measured in a custom built assembly mounted ProboStat (NORECS, Oslo, Norway) measurement cell, described in detail elsewhere.[12] The disc shaped pellets were placed on an alumina plate with an integrated S-type thermocouple. Two thermocouples and four platinum electrodes for the van der Pauw measurements were pressed on top of the surface of the pellet by springload. A resistive heater on one side of the sample allowed to apply a temperature difference in-plane of the sample. The setup allows to measure in-plane Seebeck and conductivity under identical experimental conditions. $FeWO_4$ was measured under protective Ar atmosphere to avoid decomposition of the compound above 540 °C. To establish the direct p-n junction individual pellet surfaces were thoroughly ground to 1.5 mm height, polished, and one side of each pellet was painted with platinum-ink. The n-type and p-type pellets were sandwiched between platinum net and flat platinum electrodes and pressed together by springload to ensure good electrical contact. After an initial "as-prepared" characterization, the stack was annealed at 900 °C for 24 h in protective atmosphere to ensure good surface contact. *I*-*V* characteristics of the p-n junction were measured using a *Gamry* Reference 3000 potentiostat in three-wire mode.

Density functional theory (DFT) calculations are performed with the Vienna *ab initio* simulation package (VASP)[13–15], using the projector augmented wave (PAW) method for computational efficiency[16]. An initial optimisation of the structural models is performed, starting from experimental outputs, within the general gradient approximation (GGA) for the exchange and correlation functionals, following the implementation proposed by Perdew, Burke and Ernzerhof (PBE)[17]. The Hubbard parameter U is introduced to account for the strong on-site Coulomb interaction of localized d electrons, not correctly described within the GGA approach, using the rotational invariant method, introduced by Dudarev and coworkers[18], with an effective U value of 4 eV for both Fe and W. The energy cut-off for the expansion in plane waves is set to a 500 eV, while reciprocal space is sampled using a Monkhorst-Pack (MP) grid[19] with a 0.1 Å^{-1} spacing between adjacent points. Integrals over the Brillouin zone are computed using the tetrahedron method with Blöchl corrections[20]. These parameters ensure a convergence of the total energies within 5 meV. The non-local part of the pseudopotential is evaluated using the real space projection scheme to improve the computational efficiency[21]. The energy convergence thresholds of the self-consistent field and of the structural optimisation calculations are set to 10^{-5} eV and 10^{-3} eV respectively. Each calculation is repeated for distinct magnetic orderings of the Fe sub-lattice, considering ferromagnetic and anti-ferromagnetic configurations. The properties of the energetically most favourable systems are then recalculated using the screened hybrid functional originally developed by Heyd, Scuseria and Ernzerhof (HSE)[22,23]. We follow both the well-established recipes known in literature, HSE03 and HSE06, for the ratio between the screened Hartree-Fock and the standard PBE exchange. We find better agreement with experimental data for the HSE03 approach. Due to the large computational cost of these calculations, we have reduced the density of the sampled points in reciprocal space to 0.5 Å^{-1}, while the other parameters are unmodified with respect to the GGA calculations. A test calculation with a 0.3 Å^{-1} density, performed only for the $FeWO_4$ system because of its smaller unit cell, revealed a convergence within 5 meV and 30 meV for the total and the band gap energy respectively, indicating a good accuracy level.

Results and discussion

$FeWO_4$

The electric conductivity of $FeWO_4$ follows a thermally activated trend, with a smooth transition at about 500 °C as seen in Figure 1a. The p-type conductivity is maintained over the entire temperature range, which is evident from the positive Seebeck coefficient plotted in Figure 1b. The p-type charge carriers have been described as small polaron holes, localized on Fe sites, representing oxidized Fe^{3+} species.[24–26] Bharati *et al.*[27] proposed the change at 500 ℃ to stem from a transition from small to large polarons, however we find this as untypical and suggest a relation to defect chemistry.[28]

The Seebeck coefficient below 500 ℃ is nearly constant (see Figure 1b). In the Hubbard model for correlated systems[29] this indicates a region of constant charge carrier concentration, which can be attributed either to a specific doping level or to a frozen-in defect concentration. Activation energies are obtained from a $\ln(\sigma T)$ vs. $1/T$ plot, as these materials conduct in a polaron hopping manner with a diffusion-like mechanism. The conductivity activation energy of 0.18(2) eV in the constant charge carrier region is thus equal to the polaron mobility migration barrier. The experimental value of 0.18(2) eV is close to the theoretically predicted minimum migration barrier of 0.14 eV.[30] Above 500 ℃, a decrease in the Seebeck coefficient can be identified, which indicates an increase in the charge carrier concentration. The conductivity activation energy now reflects both concentration (formation) and mobility (migration) of the charge carriers. Assuming the mobility migration barrier of 0.18(2) eV remains unchanged, the total conductivity activation energy of 0.52(3) eV results in a charge carrier formation energy of 0.34 eV, which is again close to the theoretically predicted formation energy of 0.48 eV.[30] As this energy is too small to be half the band gap and to reflect intrinsic ionization, it may rather be attributed to a charge carrier formation reaction in the form of oxygen interstitials or cation vacancies. This would result in a standard enthalpy of formation of the point defect and two hole charge carriers of 0.34 eV x 3 $\approx$ 1 eV, which is a typical value for formation of oxygen excess or cation deficiency defects from O_2(g). According to DFT calculations Fe vacancies are the most stable intrinsic defects,[30] and if formed alone (without simultaneous formation of W vacancies) must be accompanied by exsolution of an iron rich phase, such as a binary iron oxide. The leveling out below 500 ℃ in both conductivity and Seebeck coefficient - as indicated above - is accordingly interpreted as a region of the frozen-in defect formation reaction, or an overtaking of a slight non-stoichiometry in the cation ratio inherent to the synthesis. Band gap measurements for $FeWO_4$ are quite

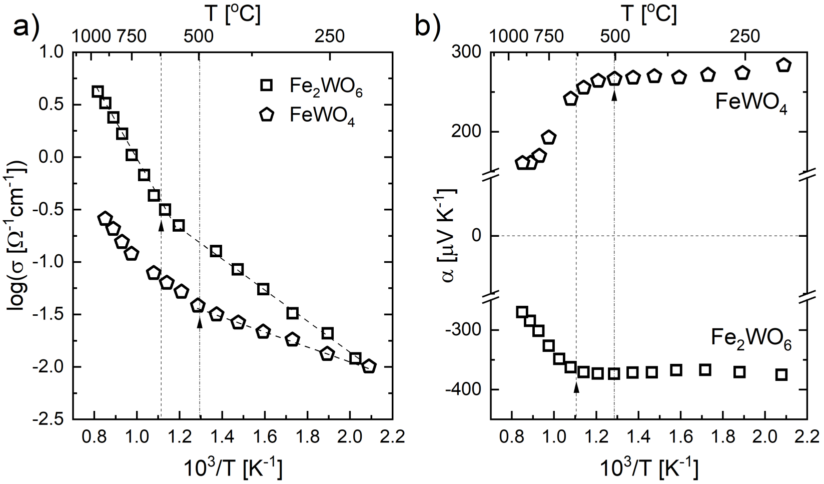

Figure 1: a) Conductivity and b) Seebeck coefficient of Fe_2WO_6 (□) and $FeWO_4$ (⬠) as a function of inverse temperature.

consistently around 2 eV in literature,[26,30,31] and supported by our DFT calculations, which will be discussed in a later section. Optical reflectance measurements, analyzed in a Kubelka-Munk plot, revealed a major indirect absorption edge at 1.48(2) eV, which is too low to be in the region of the band gap (shown in the supplementary information Figure A.5). DFT calculations suggest major parallels in the density of states near the band gap between $FeWO_4$ and FeO,[32] we thus compare the two briefly in the following. Balberg *et al.* report an absorption feature at ∼1.3 eV,[33] assigned to the $^5T_{2g} \rightarrow ^5 E_g$ transition,[34] which effectively "blackens-out" higher absorption edges. Although they could observe the hint of an absorption edge at 2 eV, representing the band gap, this was not possible for $FeWO_4$. For the construction of the band alignment diagram (see below), we assume a band gap of 2.00 eV for $FeWO_4$.

$\mathbf{Fe_2WO_6}$

Likewise, thermally activated conductivity is observable in an Arrhenius plot for Fe_2WO_6, with two straight lines and a transition at 650 °C. The negative Seebeck coefficient indicates n-type conductivity over the accessible temperature range. A decrease in the absolute Seebeck coefficient coincides with the transition in the Arrhenius plot at 650 ℃. The conductivity is of small polaron hopping nature with electrons localized on Fe sites, representing reduced Fe^{2+} states.[35] In an earlier publication, we have investigated the electrical transport and oxygen non-stoichiometry of Fe_2WO_6 in detail, based on a defect chemical description.[36] Band gap estimates for Fe_2WO_6 are not straightforward and several energies have been reported in literature. Optically measured band gaps are often reported to be of 1.5-1.7 eV,[37] which is close to, but smaller than the absorption edge visible for our sample in the Kubelka-Munk-plot occurring at 1.84(2) eV (see supplementary Figure A.5). A band gap smaller than 1.66 eV would indicate a degenerate semiconductor with the Fermi level in the valence band (as this corresponds to the valence band off-set determined for our sample by XPS), contradicting the non-degenerate semiconductor properties from conductivity measurements. Our DFT calculations (see Figure 6) predict a band gap of 2.3 eV, which is much larger than the experimentally obtained values. However it should be noted that the calculations do not include any defects or mixed valence states in the structure, and it is possible that the presence of oxygen vacancies and reduced iron species lower the band gap significantly. We take the band gap estimate of 1.84 eV as a realistic assumption for the construction of the band diagram. As indicated above, the two tungstates show related, yet opposite characteristics. The charge carrying species of one of the tungstates, represents the matrix component of second tungstates, and vice versa - specifically: In the divalent iron matrix of $FeWO_4$, Fe^{3+} represents an electron hole, whereas in Fe_2WO_6 the opposite situation is given, with Fe^{2+} representing an extra electron in the trivalent iron the host structure. $FeWO_4$ and Fe_2WO_6 are the only ternary compounds in the phase diagram of the Fe-W-O system, and have been shown to coexist as separate phases.[38–40] The lattice constants of $FeWO_4$ and Fe_2WO_6 prior and after being in contact with each other at high temperatures for an extended period of time did not change significantly and there is no indication for the formation of other phases. For comparison, in the solid solutions of $Fe_{1-x}Mn_xWO_4$ the a-axis lattice parameter shows a high sensitivity on the Mn content, varying by more than

0.1 Å.[41] We therefore expect $FeWO_4$ and Fe_2WO_6 to be separated by a large miscibility gap in a quasi-binary phase diagram.

The electronic junction between $FeWO_4$ and Fe_2WO_6

The *I*-*V* characteristics of the p-n junction is shown in Figure 2a. Already the as-assembled junction of polished separate pellets showed fully ohmic behavior at room temperature in a bias window from -5 to +5 V, with no sign of rectification. Annealing of the junction at 900 ℃ for 24 h decreased the absolute resistance as the two pellets grew together, increasing the effective contact area. Ohmic behavior did, however not change, and was observable at temperatures from -196 ℃ to 1000 ℃. The course of the area specific resistance (ASR) as a function of temperature is depicted in Figure 2b (low temperature *I*-*V* characteristics are available in the supplementary information). Above 500 ℃ the ASR levels out, becoming seemingly temperature independent at approximately 1.2 Ωcm^2. We attribute this to the collective resistances of setup wiring and current collectors, which can not be fully eliminated in the 2-electrode 3-wire measurements. The individual materials resistances are by one order of magnitude lower compared to the

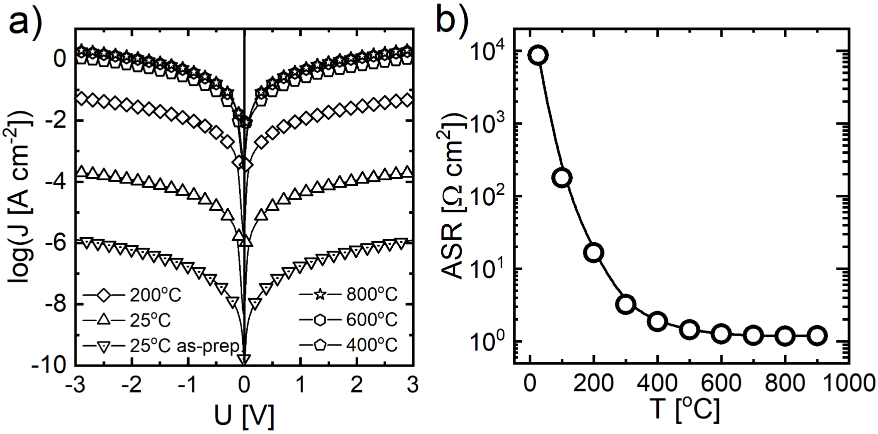

Figure 2: a) Logarithmic *I*-*V* characteristics of the p-n junction of Fe_2WO_6 and $FeWO_4$ from room temperature to 900 ℃ b) Junction area specific resistance (ASR) as function of temperature.

measured total junction resistance, indicating that the majority of voltage drops across the junction and not in the individual materials.

The ohmic behavior of the p-n junction points towards the band alignment of a broken gap junction. A broken gap junction forms between materials with a large difference in electron affinities, where the respective band gaps do not overlap. Bringing such two materials into contact results in a flow of electrons from the p-type to the n-type, as the Fermi level of the p-type lies above the Fermi level of the n-type. This leads to a charge accumulation region at the junction in contrast to a charge depletion zone in classic staggered junctions. With the Fermi level aligned in equilibrium, charge transfer takes place directly between the p-type valence band and the n-type conduction band. A schematic illustration of the broken band junction is shown in Figure 3. Non-rectifying, low contact resistance is also typical for tunnel junctions at low biases.[10] These tunnel junctions however usually depend highly on the applied bias, and show a characteristic breakdown region of negative differential resistance in forward bias, due to a bias driven misalignment between the n-type conduction band and p-type valence band, when crossing a critical transition point. At further increased forward bias, beyond the negative resistance region the tunnel junctions behave like typical rectifying p-n junctions with exponential current increase. For the iron tungstates junction the tunneling junction explanation can be ruled out, due to the absence of a breakdown region and of an exponential growth region. Below temperatures of 500 °C the junction shows an activation energy of 0.42(2) eV in an Arrhenius plot. The activation energy has to be attributed to the potential barrier arising

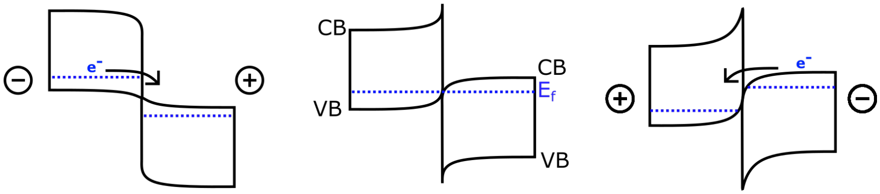

Figure 3: Schematic illustration of a broken gap junction in a) reverse bias, b) equilibrium, and c) forward bias.

from the charge accumulation layer forming at the junction.

X-ray photoelectron spectroscopy

To confirm the validity of this type of band alignment, x-ray photo electron spectroscopy (XPS) measurements were carried out. XPS provides insight on the Fermi level position via the work function (Φ) in respect to the vacuum level, and valence band offset (VBO) with respect to the Fermi level, and allows calculation of the electron affinity (χ). From the primary electron onset, the valence band offset (VBO) in respect to the Fermi level can be obtained, whereas the secondary electron cut-off gives the work function (Φ), which is the position of the Fermi energy in respect to the vacuum level. Intensity onsets can in most cases be extracted from linear fit intersects, between baseline and leading edge of the onset slope. Following this practice, valence band offsets with respect to the Fermi energy were determined to be 1.66 eV and 0.17 eV for Fe_2WO_6 and $FeWO_4$, respectively (see Figure 4b,d). The primary electron onset for $FeWO_4$ shows a peculiar double onset, shifted by 1.2 eV to which we will return in a later section. Secondary electron cut-off for Fe_2WO_6 produced a work-function of 4.51 eV. The cut-off for $FeWO_4$, however, is not accessible by this method as the onset is smeared out, which is likely to stem from tail states, surface space charge or surface roughness. An exclusion principle based on the confidence interval of the baseline was used to determine the real onset in $FeWO_4$ (described in the supplementary information). Applying this method resulted in a work function of 4.32 eV for $FeWO_4$. For comparison, applying this method to the cut-off in Fe_2WO_6 produces the same work function as the linear extrapolation method.

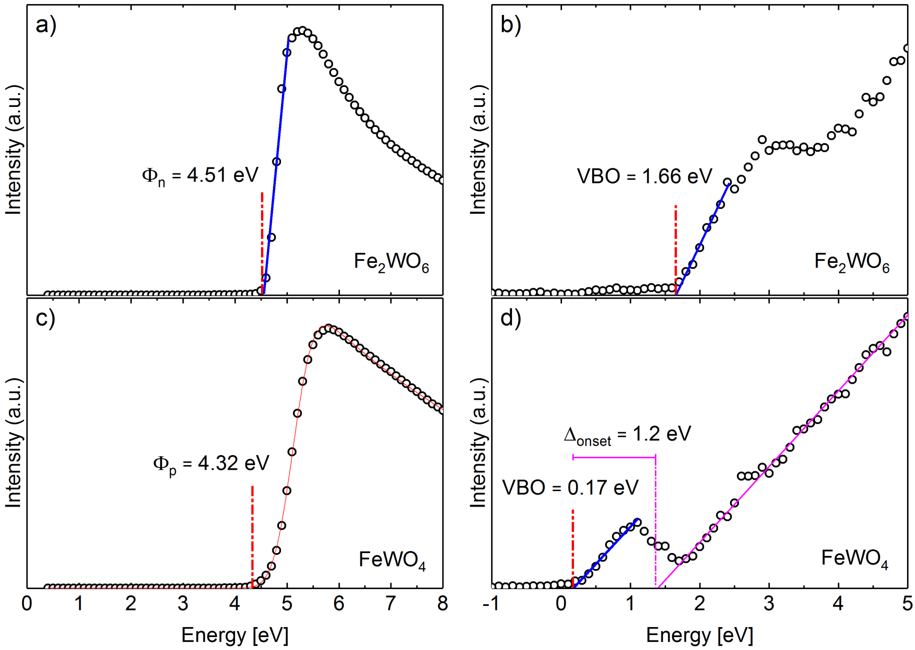

Figure 4: X-ray photo emission spectra narrow scans of selected regions. The narrow scans a) and c) depict the secondary electron cut-off, representing the work function of Fe_2WO_6 and $FeWO_4$. Narrow scans b) and d) show primary electron onset narrow scans, representing valence band offsets (VBO) with respect to the Fermi energy of Fe_2WO_6 and $FeWO_4$.

The junction band alignment

From work-function (Φ), valence band offset (VBO) and band gap (E_g), a simple band-alignment diagram can be constructed and the electron affinity (χ) calculated. Electron affinities $\chi_p = 2.49$ eV and $\chi_n = 4.33$ eV were calculated for $FeWO_4$ and Fe_2WO_6, respectively from the relation

$$\chi = \Phi + E_{\text{VBO}} - E_g \tag{1}$$

The schematic energy band diagram is shown in Figure 5. The vacuum level is taken as reference point. The Fermi level of the p-type $FeWO_4$ lies 0.19 eV higher in energy than E_f for the n-type Fe_2WO_6, fulfilling the condition $\Phi_p < \Phi_n$ for non-rectifying p-n

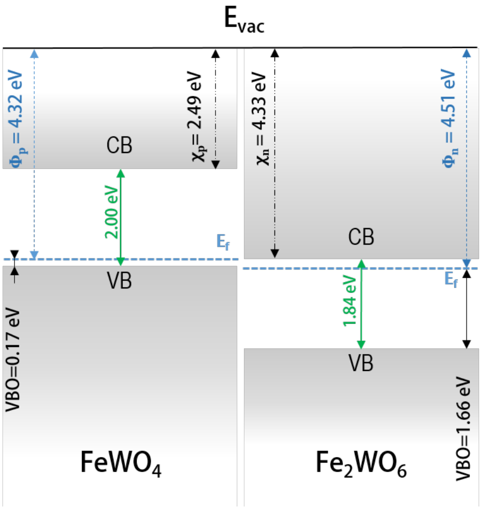

Figure 5: Schematic illustration of the band alignment between $FeWO_4$ and Fe_2WO_6 before equilibrium. The alignment resembles a near-broken gap junction, with the Fermi level of $FeWO_4$ lying higher than that of Fe_2WO_6, thus resulting in a charge accumulation region at equilibrium in contrast to a charge depletion zone in staggered junctions.

junctions.[42] It becomes clear that the alignment is not a fully broken one, but rather a near-broken gap junction, as the CBM of Fe_2WO_6 still lies 0.16 eV above the VBM of $FeWO_4$. Near-broken gap junctions, however can still exhibit the ohmic behavior of full-broken gap junctions, assuming band tails to enable the crossing between the conduction and valence band.[11] We thus suggest a band bending as described in Figure 3b, where the n-type conduction band bends downwards and the p-type valence band bends upwards, forming an s-shape like alignment.

DFT calculations

The density of states (DOS) obtained from *ab initio* density-functional calculations are shown in Figure 6 and provide additional insight into the dominant character of the crucial bands involved. Hybrid functional HSE potentials are capable of providing an accurate description of complex structures.[43,44] We present results from HSE03 calculations, which shows better correspondence to experiments than HSE06. The DOS is spin averaged for clarity and limited to the section that is relevant for the band gaps. A more detailed spin-resolved DOS plot in an extended range is available in the supplementary information in Figure A.7. The calculations assume perfect crystallinity at 0K without the presence of defects, mixed valencies or surface effects. Thus no inter-band gap states occur and the Fermi level is put to the valence band edge at zero energy. In Figure A.7, the DOS plot of Fe_2WO_6 is shifted downwards to represent the band alignment and the dashed line indicates the common Fermi level as proposed by our XPS results.

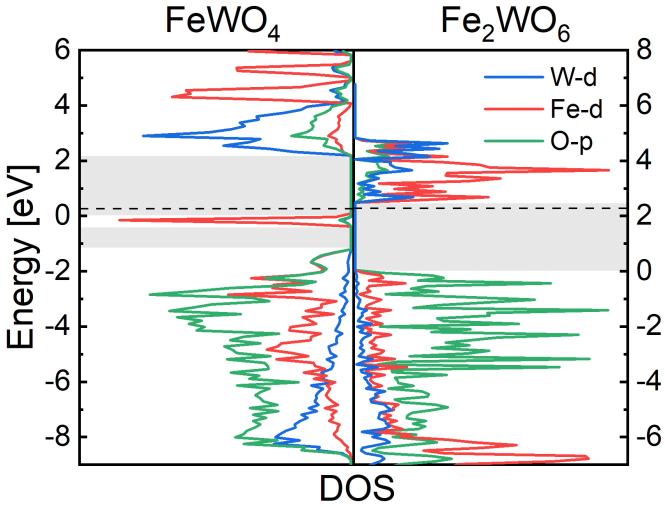

Figure 6: DFT (HSE03) calculated projected densities of states for a) $FeWO_4$ and b) Fe_2WO_6. The energy scales are shifted by the difference in their work functions to indicate the junctions alignment as proposed above. The contributions are averaged over spin for clarity. The common Fermi level is indicated by a dotted line and the grey overlays display band gaps.

Our DFT calculations predict a band gap of 2.00 eV for $FeWO_4$ in good accordance with previously reported DOS of $FeWO_4$ using a hybrid functional.[30,45] The main band gap is followed by a second band gap of 1.1 eV, between the localized Fe-3d state and lower lying filled O-2p bands. This second band gap is indeed observable in Figure 4d, as a second onset shifted by 1.2 eV in the XPS primary electron onset. GGA+U calculations are not able to reproduce the isolated Fe-3d band above the O-2p valence bands. It should be emphasized that the VBM of $FeWO_4$ is a cationic state, in contrast to an anionic state that is usually the case for binary/ternary semiconductors (e.g. from the common anion rule).

The calculations predict a band gap of 2.3 eV for Fe_2WO_6, which is experimentally estimated at 1.84 eV. Intra-band gap states from oxygen vacancies and reduced Fe species are not considered in the calculations, and would expectedly reduce the calculated band gap.[46] The VBM of Fe_2WO_6 is mainly composed of O-2p and the CBM is dominated by Fe-3d bands. Since the VBM of $FeWO_4$ and the CBM of Fe_2WO_6 are both of Fe-3d character, the band alignment as proposed above, conclusively takes place between bands of the same character. To date the band alignment between semiconducting transition metal oxides in heterojunctions is not well investigated. We would like to emphasize, that several other transition metal oxides, containing e.g. Co or Mn, show cationic states at the VBM. It remains open whether the presence of a low lying cation band is beneficial for the formation of ohmic p-n junctions, and can be exploited. Mentionable here is the p-n junction between $Ca_3Co_4O_9$ and $CaMnO_3$, reported by Kanas *et al.*, showing non-rectifying behavior.[47] The p-type $Ca_3Co_4O_9$ does indeed show a cationic Co-3d band at the valence edge.[48] We can compare this to the well investigated heterojunction of n-ZnO and p-NiO, where both VBMs are dominated by O-2p bands. Sultan *et al.* undertook a study on band alignment and I-V characteristics of ZnO/NiO heterojunctions, showing a staggered band alignment and rectifying behavior with a "turn-on" voltage of 0.9 V. Based on band gap values for ZnO (3.28 eV) and NiO (3.45 eV), they show a staggered band alignment with $\Delta_{CB} = 2.82$ eV and $\Delta_{VB} = 2.65$ eV offsets for conduction and valence bands, respectively. This leaves a band discontinuity $\mathrm{CB}_{\mathrm{ZnO}} - \mathrm{VB}_{\mathrm{NiO}}$ of merely 0.63 eV between ZnO conduction and NiO valence band edge.[49] Despite the small band discontinuity that junction exhibits rectifying behavior. For comparison, the $FeWO_4/Fe_2WO_6$ heterojunction in thermal equilibrium results in a band discontinuity of $\mathrm{CB}_{\mathrm{Fe_2WO_6}} - \mathrm{VB}_{\mathrm{FeWO_4}} = 0.35$ eV.

Conclusion

We have investigated $FeWO_4$ and Fe_2WO_6 as a model p-n couple for high temperature direct junction thermoelectrics. In contact, these materials stay p-type/ n-type, show no reactivity towards each other, and remain coexistent phases. Assembled p-n junctions show non-rectification over a large temperature range from -196 ℃ to 1000 ℃. This is consistent with the model of a near-broken gap junction, forming a charge accumulation zone and a band alignment between the p-type VB and the n-type CB, in contrast to a depletion zone and a VB-VB / CB-CB alignment in a common staggered-gap junction. Based on XPS and UV-VIS reflectance measurements, we schematically describe the band alignment diagram for the p-n couple. Our findings are supported by *ab initio* calculations, showing that both $FeWO_4$ VBM and Fe_2WO_6 CBM are of Fe-3d character. These observations may have a wider validity. However, further investigations are needed to clarify whether the presence of d-bands at the VBM represent a good criterion for designing broken gap junctions in transition metal oxide p-n couples. As $FeWO_4$ is not stable in air above 500 ℃, air stable alternatives should be investigated in the future. We have demonstrated the first near-broken gap junction to the field of thermoelectrics, which presents a promising approach to direct junction p-n junction thermoelectrics. They circumvent the rectifying diode behavior of classic staggered-gap junctions and their large parasitic resistance.

Acknowledgement

We thank prof. Terje Finstad (University of Oslo) for helpful comments and Martin Fleissner Sunding (SINTEF Industry, Oslo) for assistance in the XPS data acquisition. The authors acknowledge the Research Council of Norway for providing the computing time (under the project number NN2875k and NS2875k) at the Norwegian supercomputer facility.

References

(1) Ohtaki, M. Recent Aspects of Oxide Thermoelectric Materials for Power Generation from Mid-to-High Temperature Heat Source. *Journal of the Ceramic Society of Japan* **2011**, *119*, 770–775.

(2) Walia, S.; Balendhran, S.; Nili, H.; Zhuiykov, S.; Rosengarten, G.; Wang, Q. H.; Bhaskaran, M.; Sriram, S.; Srano, M. S.; Kalantar-zadeh, K. *Progress in Materials Science* **2013**, *58*, 1443–1489.

(3) Liu, W.; Bai, S. Thermoelectric Interface Materials: A Perspective to the Challenge of Thermoelectric Power Generation Module. *Journal of Materiomics* **2019**, *5*, 321 – 336.

(4) Aswal, D. K.; Basu, R.; Singh, A. Key Issues in Development of Thermoelectric Power Generators: High Figure-of-Merit Materials and their Highly Conducting Interfaces with Metallic Interconnects. *Energy Conversion and Management* **2016**, *114*, 50 – 67.

(5) Ni, J. E.; Case, E. D.; Schmidt, R. D.; Wu, C.-I.; Hogan, T. P.; Trejo, R. M.; Kirkham, M. J.; Lara-Curzio, E.; Kanatzidis, M. G. The Thermal Expansion Coefficient as a Key Design Parameter for Thermoelectric Materials and its Relationship to Processing-Dependent Bloating. *Journal of Materials Science* **2013**, *48*, 6233–6244.

(6) Shin, W.; Murayama, N.; Ikeda, K.; Sago, S. Thermoelectric Power Generation Using Li-doped NiO and (Ba, Sr)PbO3 Module. *Journal of Power Sources* **2001**, *103*, 80 – 85.

(7) Chavez, R.; Angst, S.; Hall, J.; Maculewicz, F.; Stoetzel, J.; Wiggers, H.; Hung, L. T.; Van Nong, N.; Pryds, N.; Span, G.; Wolf, D. E.; an Gabi Schierning, R. S. Efficient p-n Junction-based Thermoelectric Generator that can operate at extreme Termperature Conditions. *Journal of Physics D: Applied Physics* **2018**, *51*, 014005.

(8) Chavez, R.; Angst, S.; Stoetzel, J.; Kessler, V.; Bitzer, L.; Maculewicz, F.; Benson, N.; Wiggers, H.; Wolf, D.; Schierning, G.; Schmechel, R. High Temperature Thermoelectric Device Concept Using Large are p-n Junctions. *Journal of Electronic Materials* **2014**, *43*, 2376–2383.

(9) Johnson, F.; Song, S. H.; Abrahamson, J.; Liptak, R.; Aydil, E.; Campbell, S. A. Sputtered Metal Oxide Broken Gap Junctions for Tandem Solar Cells. *Solar Energy Materials and Solar Cells* **2015**, *132*, 515 – 522.

(10) Song, S. H.; Aydil, E. S.; Campbell, S. A. Metal-Oxide Broken-Gap Tunnel Junction for Copper Indium Gallium Diselenide Tandem Solar Cells. *Solar Energy Materials and Solar Cells* **2015**, *133*, 133 – 142.

(11) Johnson, F.; Pankow, J.; Teeter, G.; Benton, B.; Campbell, S. A. High Stability Near-Broken Gap Junction for Multijunction Photovoltaics. *Journal of Vacuum Science & Technology A* **2019**, *37*, 011201.

(12) Schrade, M.; Fjeld, H.; Norby, T.; Finstad, T. G. Versatile Apparatus for Thermoelectric Characterization of Oxides at high Temperatures. *Review of Scientific Instruments* **2014**, *85*, 103906.

(13) Kresse, G.; Hafner, J. *Ab initio* Molecular Dynamics for Liquid Metals. *Physical Review B* **1993**, *47*, 558–561.

(14) Kresse, G.; Furthmüller, J. Efficiency of *ab initio* Total Energy Calculations for Metals and Semiconductors Using a Plane-Wave Basis Set. *Computational Materials Science* **1996**, *6*, 15–50.

(15) Kresse, G.; Furthmüller, J. Efficient Iterative Schemes for *ab initio* Total-Energy Calculations Using a Plane-Wave Basis Set. *Physical Review B* **1996**, *54*, 11169–11186.

(16) Kresse, G.; Joubert, D. From Ultrasoft Pseudopotentials to the Projector Augmented-Wave Method. *Physical Review B* **1999**, *59*, 1758–1775.

(17) Perdew, J. P.; Burke, K.; Ernzerhof, M. Generalized Gradient Approximation Made Simple. *Physical Review Letters* **1996**, *77*, 3865–3868.

(18) Dudarev, S. L.; Botton, G. A.; Savrasov, S. Y.; Humphreys, C. J.; Sutton, A. P. Electron-Energy-Loss Spectra and the Structural Stability of Nickel Oxide: An LSDA+U Study. *Physical Review B* **1998**, *57*, 1505–1509.

(19) Monkhorst, H. J.; Pack, J. D. Special Points for Brillouin-Zone Integrations. *Physical Review B* **1976**, *13*, 5188–5192.

(20) Blöchl, P. E.; Jepsen, O.; Andersen, O. K. Improved Tetrahedron Method for Brillouin-Zone Integrations. *Physical Review B* **1994**, *49*, 16223–16233.

(21) King-Smith, R. D.; Payne, M. C.; Lin, J. S. Real-Space Implementation of Nonlocal Pseudopotentials for First-Principles Total-Energy Calculations. *Physical Review B* **1991**, *44*, 13063–13066.

(22) Heyd, J.; Scuseria, G. E.; Ernzerhof, M. Hybrid Functionals Based on a Screened Coulomb Potential. *Journal of Chemical Physics* **2003**, *118*, 8207–8215.

(23) Krukau, A. V.; Vydrov, O. A.; Izmaylov, A. F.; Scuseria, G. E. Influence of the Exchange Screening Parameter on the Performance of Screened Hybrid Functionals. *Journal of Chemical Physics* **2006**, *125*, 224106.

(24) Sieber, K.; Kourtakis, K.; Kershaw, R.; Dwight, K.; Wold, A. Preparation and Photoelectronic Properties of $FeWO_4$. *Materials Research Bulletin* **1982**, *17*, 721 – 725.

(25) Schmidbauer, E.; Schanz, U.; Yu, F. J. Electrical Transport Properties of Mono- and Polycrystalline $FeWO_4$. *Journal of Physics: Condensed Matter* **1991**, *3*, 5341–5352.

(26) Ejima, T.; Banse, T.; Takatsuka, H.; Kondo, Y.; Ishino, M.; Kimura, N.; Watanabe, M.; Matsubara, I. Microscopic Optical and Pphotoelectron Measurements of MWO_4 (M=Mn, Fe, and Ni). *Journal of Luminescence* **2006**, *119-120*, 59 – 63, Dynamical Processes in Excited States of Solids.

(27) Bharati, R.; Yadava, Y. P.; Singh, R. A. Electrical Transport Properties of Iron (II) Tungstate. *Journal of Materials Science Letters* **1983**, *2*, 808–810.

(28) Austin, I.; Mott, N. Polarons in Crystalline and Non-Crystalline Materials. *Advances in Physics* **1969**, *18*, 41–102.

(29) Chaikin, P. M.; Beni, G. Thermopower in the Correlated Hopping Regime. *Physical Review B* **1976**, *13*, 647–651.

(30) Hoang, K. Polaron Formation, Native Defects, and Electronic Conduction in Metal Tungstates. *Physical Review Materials* **2017**, *1*, 024603.

(31) Gao, Q.; Liu, Z. $FeWO_4$ Nanorods with Excellent UV–Visible Light Photocatalysis. *Progress in Natural Science: Materials International* **2017**, *27*, 556 – 560.

(32) Lany, S. Semiconducting Transition Metal Oxides. *Journal of Physics: Condensed Matter* **2015**, *27*, 283203.

(33) Balberg, I.; Pinch, H. The Optical Absorption of Iron Oxides. *Journal of Magnetism and Magnetic Materials* **1978**, *7*, 12 – 15.

(34) Sherman, D. M. In *Composition, Structure and Properties of Mineral Matter*; Marfunin, A. S., Ed.; Springer-Verlag, Chapter Electronic Structures of Iron Oxides and Silicates, pp 327–340.

(35) Leiva, H.; Dwight, K.; Wold, A. Preparation and Characterization of Conducting Iron Tungstates. *Journal of Solid State Chemistry* **1982**, *42*, 41 – 46.

(36) Schuler, R.; Norby, T.; Fjellvåg, H. Defects and Polaronic Transport in Fe_2WO_6. *Physical Chemistry Chemical Physics* **2020**, *27*, 15541–15548.

(37) Abdi, F. F.; Chemseddine, A.; Berglund, S. P.; van de Krol, R. Assessing the Suitability of Iron Tungstate (Fe_2WO_6) as a Photoelectrode Material for Water Oxidation. *The Journal of Physical Chemistry C* **2017**, *121*, 153–160.

(38) Schmahl, N. G.; Dillenburg, H. Phase Equilibrium and Thermodynamics of the Ternary Systems Fe-Mo-O and Fe-W-O. *Zeitschrift für Physikalische Chemie* **1972**, *77*, 113–26.

(39) Hochleitner, R.; Schröcke, H. Heterogene Gleichgewichte in der Wolframitgruppe. *Tschermaks mineralische und petrographische Mitteilungen* **1985**, *34*, 35–47.

(40) Hsu, C., L The Stability Relations of the Wolframite Series. *American Mineralogist* **1976**, *61*, 944–955.

(41) García-matres, E.; Stüßer, N.; Hofmann, M.; Reehuis, M. Magnetic Phases in $Mn_{1-x}Fe_xWO_4$ Studied by Neutron Powder Diffraction. *The European Physical Journal B* **2003**, *32*, 35–42.

(42) Santos, H. A. *Proceedings of 8th Mediterranean Electrotechnical Conference on Industrial Applications in Power Systems, Computer Science and Telecommunications (MELECON 96)*; 1996; Vol. 1; pp 399–402.

(43) Pan, L.-Y.; Ding, Y.-F.; Yu, Z.-L.; Wan, Q.; Liu, B.; Cai, M.-Q. Layer-dependent optoelectronic property for all-inorganic two-dimensional mixed halide perovskite $Cs_2PbI_2Cl_2$ with a Ruddlesden-Popper structure. *Journal of Power Sources* **2020**, *451*, 227732.

(44) Ding, Y.-F.; Yu, Z.-L.; He, P.-B.; Wan, Q.; Liu, B.; Yang, J.-L.; Cai, M.-Q. High-performance Photodetector Based on InSe/$Cs_2XI_2Cl_2$ (X = Pb, Sn, and Ge) Heterostructures. *Physical Review Applied* **2020**, *13*, 064053.

(45) Huang, B.; Hart, J. N. DFT Study of Various Tungstates for Photocatalytic Water Splitting. *Physical Chemistry Chemical Physics* **2019**, *22*, 1727–1737.

(46) Christian, L.; Andreas, K.; Wolfram, J. Limitation of Fermi level Shifts by Polaron Defect States in Hematite photoelectrodes. *Nature Communications* **2018**, *9*.

(47) Kanas, N.; Bittner, M.; Desissa, T. D.; Singh, S. P.; Norby, T.; Feldhoff, A.; Grande, T.; Wiik, K.; Einarsrud, M.-A. All-Oxide Thermoelectric Module with in Situ Formed Non-Rectifying Complex p-p-n Junction and Transverse Thermoelectric Effect. *ACS Omega* **2018**, *3*, 9899–9906.

(48) Takeuchi, T.; Kondo, T.; Takami, T.; Takahashi, H.; Ikuta, H.; Mizutani, U.; Soda, K.; Funahashi, R.; Shikano, M.; Mikami, M.; Tsuda, S.; Yokoya, T.; Shin, S.; Muro, T. Contribution of Electronic Structure to the Large Thermoelectric Power in Layered Cobalt Oxides. 2004.

(49) Sultan, M.; Mumtaz, S.; Ali, A.; Khan, M. Y.; Iqbal, T. Band Alignment and Optical Response of Facile Grown NiO/ZnO Nano-Heterojunctions. *Superlattices and Microstructures* **2017**, *112*, 210 – 217.

A Supplementary

A.1 Powder x-ray diffraction

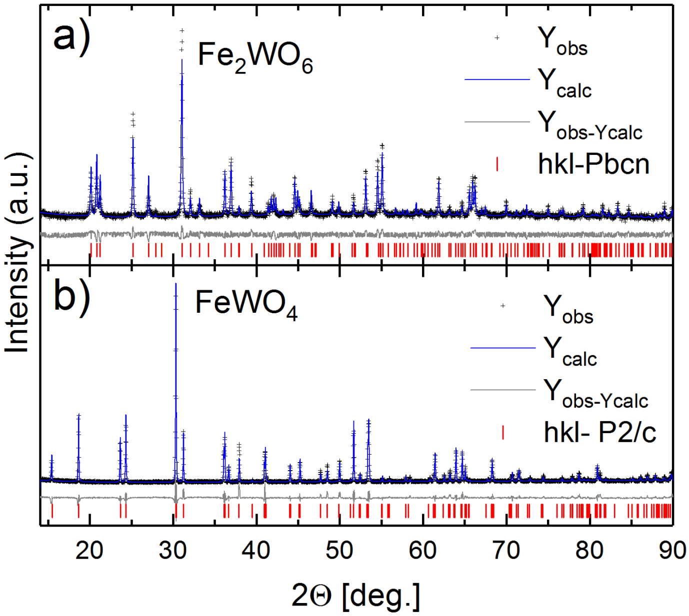

Figure A.1: Powder x-ray diffraction pattern of a) Fe_2WO_6 and b) $FeWO_4$ showing experimental data, Rietveld refinement, difference-plot and hkl ticks for the respective phases.

Table A.1: Lattice parameters for Fe_2WO_6 and $FeWO_4$ before and after being in contact with each other at elevated temperatures (900°C) determined by Rietveld refinement.

	a [Å]	b [Å]	c [Å]	β [°]
Fe_2WO_6 pre mix	4.5749(2)	16.7578(8)	4.9658(2)	90
Fe_2WO_6 post mix	4.5777(1)	16.7568(6)	4.9642(2)	90
$FeWO_4$ pre mix	4.7295(1)	5.7066(1)	4.9623(1)	90.047(3)
$FeWO_4$ post mix	4.7274(6)	5.7090(6)	4.9567(6)	90.11(1)

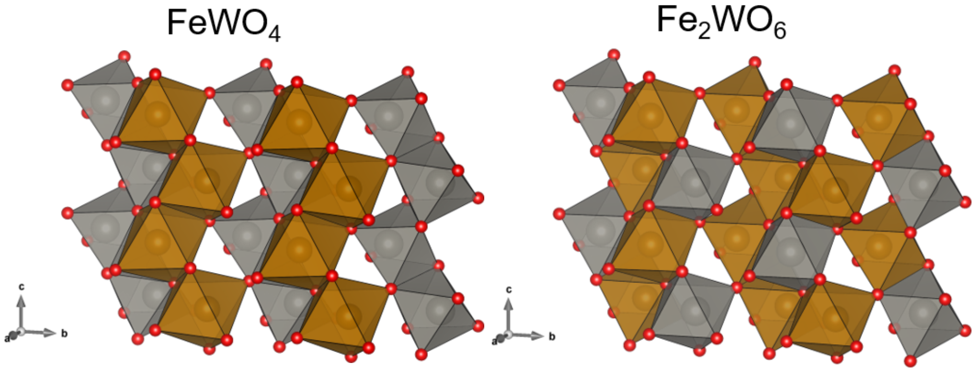

Figure A.2: Standard crystal orientation for $FeWO_4$ and Fe_2WO_6.

A.2 X-ray photoelectron spectroscopy

The onset of the work function peak in XPS spectra is usually extracted from the linear regression intersects between baseline and the quasi linear onset region. For $FeWO_4$ this would be 4.6 eV. It is visible from the spectrum though, that the real onset occurs somewhat earlier in the spectrum. This can be attributed to valence tail states above the valence band maximum, resulting in a smearing out of the Fermi level. This is visible in the slow but distinguishable increase of the intensity, even before the linear extrapolation determined onset of 4.6 eV. The true onset must thus lie between ca 3.8 and 4.6 eV. To determine the exact onset of the x-ray photo electron spectrum work function peak, the narrow scan between 0 to 4.6 eV was fitted linearly, to determine the first point to leave the baseline, thus representing the true onset point. As seen in Figure A.4, linear regression, omitting the two last points, contains all baseline points inside the 95% confidence interval. The first point to reside outside this confidence interval, can be seen as the real onset of the work function and was determined to be at 4.3 eV (marked green). Regressions containing all, or all but one point, failed to contain the majority of baseline points within the 95% confidence interval, and were thus ruled out to represent the baseline satisfactorily (marked red). In Fe_2WO_6, this method gives the same onset point of 4.51 eV as the linear fit intersect method.

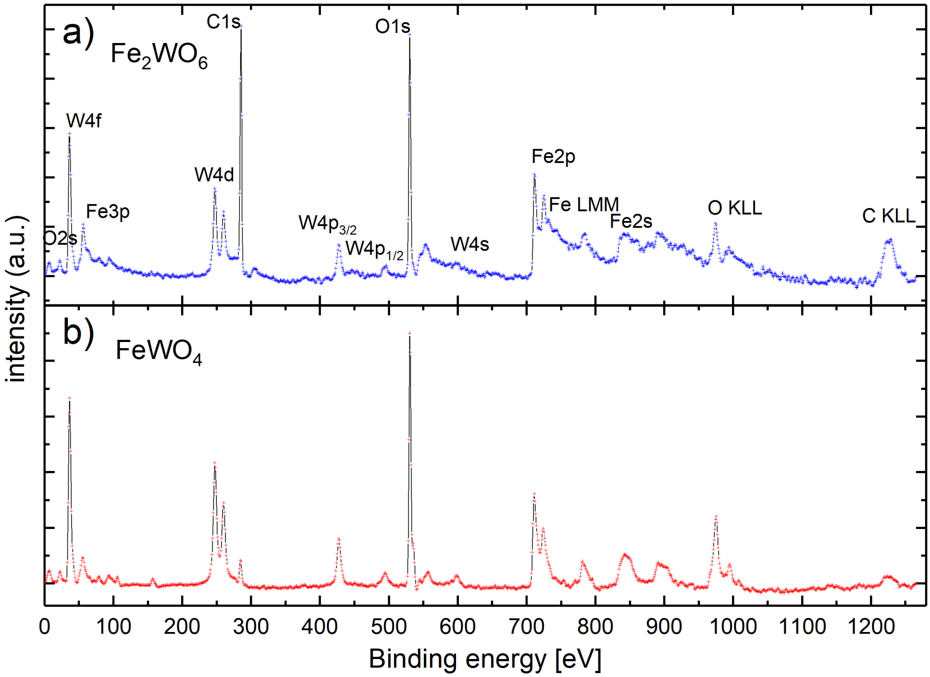

Figure A.3: X-ray photo emission survey-scan spectra of a) Fe_2WO_6 and b) $FeWO_4$. Characteristic emission features are indicated.

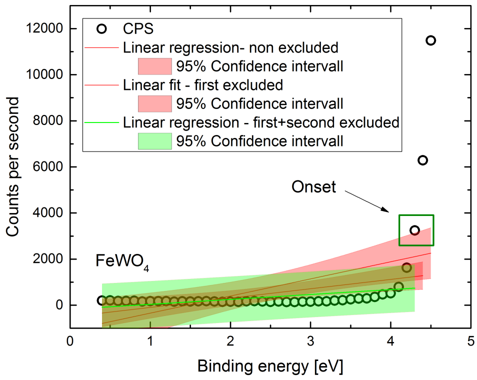

Figure A.4: XPS spectrum narrow scan of FeWO$_4$ between 0 and 4.6 eV. Linear regressions with 95%confidence bands, excluding, none-, the first-, and the second- point of the baseline interval. Exclusion of the two last points, led to a satisfying baseline regression, containing all baseline points within the 95% confidence interval. Thus exposing the first point to be outside of the confidence interval as the true onset of the work function (marked green).

A.3 Kubelka-Munk plots

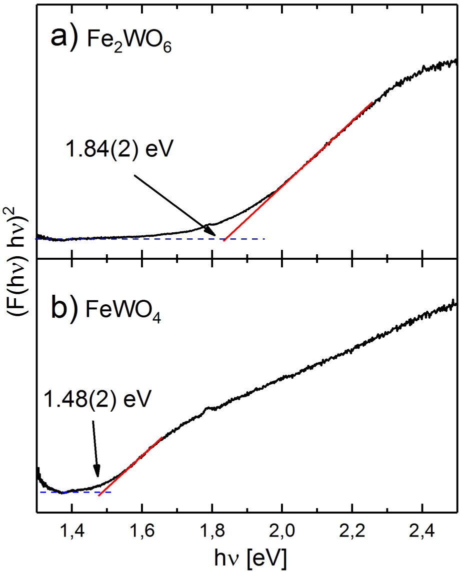

Figure A.5: Indirect transition Kubelka-Munk plot of Fe$_2$WO$_6$ and FeWO$_4$ respectively obtained from UV-VIS reflectance. F(hν) on the ordinate is obtained via the Kubelka-munk function $F(h\nu) = \frac{(1-R)^2}{2R}$, which is proportional to the absorption coefficient, allowing for an analysis equivalent to a Tauc-plot for indirect allowed transitions.

A.4 Extended *I*-*V* measurements

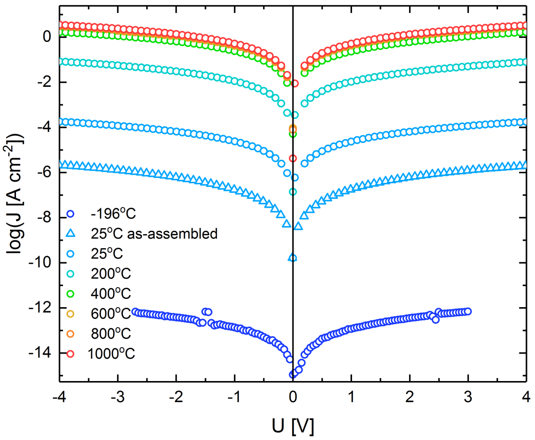

Figure A.6: Logarithmic *I*-*V* characteristics of the $FeWO_4/Fe_2WO_6$ pn-junction at various temperatures. Data plotted with a △-symbol is obtained from the as-assembled junction, whereas data plotted with a ◯-symbol is obtained after annealing the junction at 900°C.

A.5 Extended spin resolved DOS

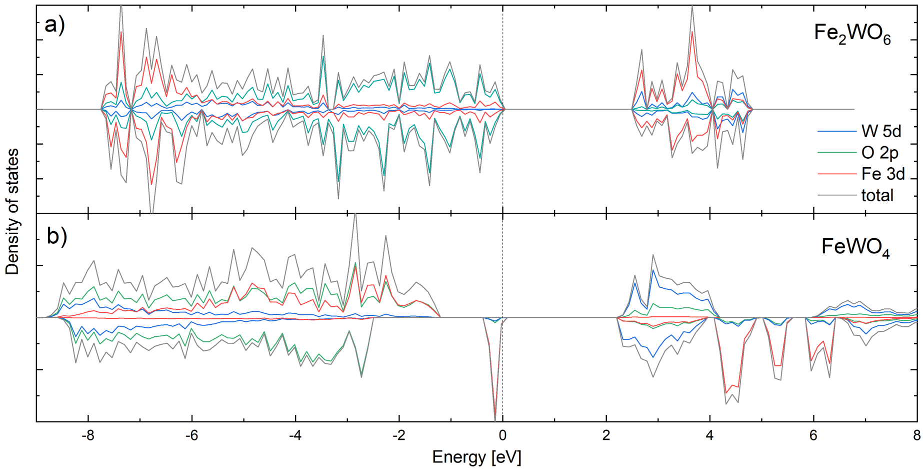

Figure A.7: Spin resolved projected density of states (HSE03) for a) Fe_2WO_6 and b) $FeWO_4$. (upper: ↑, lower: ↓)

List of symbols, acronyms, and constants

A	Area [cm^2]
$A(\Theta)$	Absorption factor
C	Proportinality constant
C_p	Specific heat capacity [J/(Kg K)]
$D(E)$	Density of states [1/cm^3]
D_n	Electron diffusion coefficient [cm^2/s]
D_p	Hole diffusion coefficient [cm^2/s]
E_B	Binding energy [eV]
E_F	Fermi energy [eV]
E_g	Band gap energy [eV]
E_u	Mobility activation energy [eV]
$F(hkl)$	Structure factor
I	Intensity [W/cm^2],[%]
I	Current [A]
J	Overlap integral [eV]
K	Equilibrium constant
LP	Lorenz polarization factor
L_n	Electron diffusion length [cm]
L_p	Hole diffusion length [cm]
N_A	Acceptor dopant concentration [1/cm^3]
N_D	Donor dopant concentration [1/cm^3]
P	Power [W]

Q	Heat [J]
R	Electrical resistance [Ω]
R_L	Load resistance [Ω]
R_{TEG}	Thermoelectric generator internal resistance [Ω]
R_∞	Remission
R_{wp}	Weighted profile residual
S	Spin degeneracy
T	Temperatuer [K],[°C]
T_C	Cold side temperature [°C]
T_H	Hot side temperature[°C]
V	Thermoelectric voltage [V]
ZT	Figure of merit (Thermoelectric modules)
$\Delta G^{\ominus}$	Standard Gibbs free energy [kJ/mol]
$\Delta H^{\ominus}$	Standard enthalpy of formation [kJ/mol]
$\Delta S^{\ominus}$	Standard entropy of formation [J/(mol K)]
Γ	Orbital degeneracy
Π	Peltier coefficient [V]
Ψ	Potential function
Θ	Incident x-ray angle [°]
χ	Electron affinity [eV]
ϵ	Permittivity [F/m]
ϵ_r	Relative permittivity ($\epsilon_r = \epsilon/\epsilon_0$)
η	Conversion efficiency [%]
λ	Wavelength [cm]
ν	Photon frequency [1/s]
ν_o	Optical phonon frequency [1/s]
ν_{id}	Ideality factor
ϕ	Electrostatic potential [V]
ϕ	Work function [eV]

ϕ_{bi}	Built-in potential [V]
ρ	Density [g/cm^3]
d	Distance [cm]
d_{hkl}	Lattice plane distance [Å]
$f(E)$	Electron distribution funciton
$f_0(E)$	Equilibrium electron distribution function
f_j	Atomic form factor
g_i	Degeneracy factor
hkl	Miller indices
j	Current density [A/cm^2]
k	Wave vector
l	Length [cm]
m	Mass [kg]
$m*$	Effective mass [m_e]
n	Electron concentration [1/cm^3]
n	Exponent for optic transition
n_i	Intrinsic charge carrier concentration [1/cm^3]
p	Hole concentration [1/cm^3]
q_e	Electronic heat flux density [W/cm^2]
r	Scattering exponent
s	Spatial coordinate
t	Time [s]
u	Mobility [cm^2/(V s)]
u	Temperature factor
v	Velocity [m/s]
x	Site fraction
z	Charge of carrier (Integer)
zT	Figure of merit (Thermoelectric materials)
α	Absorption coefficient

α	Seebeck coefficient [μV/K]
α	Thermal diffusivity [cm^2/s]
ΔT	Temperature gradient[K],[°C]
κ_e	Electronic thermal conductivity [W/(K cm)]
κ	Thermal conductivity [W/(K cm)]
μ_T	Thomson coefficient [V/K]
∇	Nabla operator $\nabla = \left(\frac{\partial}{\partial x}, \frac{\partial}{\partial y}, \frac{\partial}{\partial z}\right)$
$\dot{Q}$	Heat flux [W]
$\dot{q}$	Heat flux density [W/cm^2]
σ	Electrical conductivity [S/cm]
τ	Relaxation time [s]

Acronyms

BGJ	Broken-gap junction
CB	Conduction band
CBM	Conduction band minimum
CCO-349	$Ca_3Co_4O_9$
CF	Crystal field
DFT	Density functional theory
DOS	Density of states
GL	Gaussian-Lorentzian
HOMO	Highest occupied molecular orbital
LA	Assymetric Lorentzian
LUMO	Lowest unoccupied molecular orbital
NCO	$Na_{0.5}CoO_2$
OCV	Open circuit voltage
TC	Thermocouple
TE	Thermoelectric
TEC	Thermal expansion coefficient
TEG	Thermoelectric generator
TJ	Tunnel junction
UV-VIS	Ultraviolet-visible light spectroscopy
VB	Valence band
VBM	Valence band maximum
VdP	Van der Pauw
XPS	X-ray photoelectron spectroscopy

Physical constants

N_A	Avogadro constant 6.022 $^{x}10^{23}$ [1/mol]
R	Universal gas constant 8.314 [J/(mol K)]
ϵ_0	Vacuum permittivity 8.854 $^{x}10^{-12}$ [F/m]
e	Elementary charge 1.602 $^{x}10^{-19}$ [C]
h	Planck constant 6.626 $^{x}10^{-34}$ [Js]
m_e	Electron mass 9.109 $^{x}10^{-31}$ [Kg]
$\hbar$	Reduced Planck constant $\hbar = h/(2\pi)$
$\mathrm{k_B}$	Boltzmann's constant 1.381 $^{x}10^{-23}$ [$\mathrm{m^2kg/(s^2K)}$]